15TH INTERNATIONAL CONFERENCE on Communications, Electromagnetics and Medical Applications (CEMA'21)

Athens, Greece
21st October, 2021

Organized by:
Faculty of Telecommunications of TU-Sofia, Bulgaria

NATIONAL TECHNICAL UNIVERSITY OF ATHENS, GREECE

SCHOOL OF ELECTRICAL AND COMPUTER ENGINEERING

PROCEEDINGS

OF 15TH INTERNATIONAL CONFERENCE ON COMMUNICATIONS, ELECTROMAGNETICS AND MEDICAL APPLICATIONS (CEMA'21)

Organized by:

FACULTY OF TELECOMMUNICATIONS
TECHNICAL UNIVERSITY OF SOFIA, BULGARIA

NATIONAL TECHNICAL UNIVERSITY OF ATHENS, GREECE,
SCHOOL OF ELECTRICAL AND COMPUTER ENGINEERING

NATIONAL TECHNICAL UNIVERSITY OF ATHENS, GREECE

SCHOOL OF ELECTRICAL AND COMPUTER ENGINEERING

Athens, Greece
21st October, 2021

KING 2001, Sofia

Edited by Prof. Dr. Eng. **Dimiter Tz. Dimitrov**

ISSN: 1314-2100

SCOPUS Indexing
http://suggestor.step.scopus.com/progressTracker, ID: 6B4F77263D276412.

Printed in Bulgaria
KING 2001, Sofia

D. Dimitrov

P. Frangos

K. Dimitrov

Dear Colleagues,

It is our privilege to thank all of you for your contributions submitted at 15th regular International Conference on 'Communication, Electromagnetic and Medical Applications' CEMA'21. This is a conference which should help future collaboration in the area of engineering, especially in the area of communication technologies and medical applications. This is an important scientific event not only in Balkan region, but in Europe, also. The International Conference on Communication, Electromagnetism and Medical Applications CEMA'21 is dedicated to all essential aspects of the development of global information and communication technologies, and their impact in medicine, as well. The objective of Conference is to bring together lecturers, researchers and practitioners from different countries, working on the field of communication, electromagnetism, medical applications and computer simulation of electromagnetic field, in order to exchange information and bring new contribution to this important field of engineering design and application in medicine. The Conference will bring you the latest ideas and development of the tools for the above mentioned scientific areas directly from their inventors. The objective of the Conference is also to bring together the academic community, researchers and practitioners working in the field of Communication, Electromagnetic and Medical Applications, not only from all over Europe, but also from America and Asia, in order to exchange information and present new scientific and technical contributions.

Many well known scientists took part in conference preparation as members of International Scientific Committee or/and as reviewers of submitted papers. We would like to thank all of them for their efforts, for their suggestions and advices.

On behalf of the International Scientific Committee, we would like to wish you successful presentations of your papers, successful discussions and new collaborations for your future scientific investigations.

Engineering and medicine should provide high level of living for all people.

P. Frangos
Conference Chairman

D. Dimitrov
Conference Vice Chairman

K. Dimitrov
Conference Vice Chairman

INTERNATIONAL SCIENTIFIC COMMITTEE

Chairman:

P. FRANGOS, National Technical University of Athens, Greece

Vice Chairmen:

D. TZ. DIMITROV, Technical University of Sofia, Bulgaria
K. L. DIMITROV, Technical University of Sofia, Bulgaria

Members

N. AMPILOVA,	University of Petersburg, Russia
T. AVOYAGI,	Tokyo Institute of Technology, Japan
A. BEKJARSKY,	Technical University of Sofia, Bulgaria
E. BOEMO,	University Authonoma, Barcelona, Spain
R. BRUZGIENE,	Kaunas University of Technology, Lithuania
N. DIB,	Jordan University of Science and Technology, Aman, Jordan
V. DUMBRAVA,	Kaunas University of Technology, Litvania
N. ESCUDEIRO,	ISEP, Porto, Portugal
E. GAGO-RIBAS,	University of Oviedo, Spain
V. GEORGIEVA,	Technical University of Sofia, Bulgaria
G. GOUSSETIS,	Heriot - Watt University, United Kingdom
S. V.HOEYE,	University of Oviedo, Spain
I. ILIEV,	Technical University of Sofia, Bulgaria
F. KLETT,	Franhofer Institute, Ilmenau, Germany
G. KLIROS,	Hellenic Air-Force Academy, Athens, Greece
V. KUKENSKA,	Technical University of Gabrovo, Bulgaria
L. LUBIH,	Technical University of Sofia, Bulgaria
G. MALLET,	University "Sophia Antipolis", Nice, France
G. MATSOPOULOS,	National Technical University of Athens, Greece
M. MARTINS,	Academia Militar da Amadora, DCEE, Portugal
M.– J. MORALES-GONZALES,	University of Valladolid, Spain
L. NARBUTAITE,	Kaunas University of Technology, Lithuania
K. NIKITA,	National Technical University of Athens, Greece
M. NIKOLOVA,	High Naval School, Varna, Bulgaria
A. PANAGOPOULOS,	National Technical University of Athens, Greece
J. PETROVSKA,	Medical University of Sofia, Bulgaria
H. ROTH,	University of Siegen, Germany
S. SAUTBEKOV,	Euroasian University, Astana, Kazakhstan
A. SAVOV,	Medical University of Sofia, Bulgaria
S. SAVOV,	Technical University of Varna, Bulgaria
H.-P. SCHADE,	Technical University of Ilmenau, Germany
I. SOLOVIEV,	University of St. Petersburg, Russia
L. SONG,	Technical University of Harbin, China
G. STAMATAKOS,	National Technical University of Athens, Greece
A. USHEVA,	University of Boston, USA
R. VERDONE,	University of Bologna, Italy

REVIEWERS

BALZANO, Q.	University of Maryland, USA
BEHARI, J.	Jawaharlal Nehru University ,New Delhi, India
BOEMO, E.	Technical University of Madrid, Spain
DIMITROV, D.	Technical University of Sofia, Bulgaria
DONTSCHEWA, M.	University of Applied Sciences, Dorbirn, Austria
GOUSSETIS, G.	Heriot - Watt University, United Kingdom
MALLET, G.	University “Sophia Antipolis”, Nice, France
PETROVSKA, J.	Medical University of Sofia, Bulgaria
PRATO, F.	University of Western Ontario, Canada
ROTH, H.	University of Siegen, Germany
SAVOV, A.	Medical University of Sofia, Bulgaria
SCHADE, H-P.	Technical University of Ilmenau, Germany
SONG, L.	Technical University of Harbin, China
USHEVA, A.	University of Boston, USA

REGISTRATION

October, 21st, 09h 30min – 16h

The conference registration desk will be on-line at
National Technical University of Athens

CONFERENCE PROGRAM

21st October

OPENING CEREMONY

11h – 11h 30min
The Opening Ceremony will be on-line

SCIENTIFIC PROGRAM

21st October

FIRST SESSION

11h 30min – 13h 30min

On-line presentation and discussions

Chairman: Prof. Ivo Draganov, Faculty of Telecommunication, Technical University of Sofia, Bulgaria

---

1. **SEA STATE CHARACTERIZATION USING NORMALIZED EXPERIMENTAL ONE – DIMENSIONAL RADAR SIGNATURES AND FRACTAL TECHNIQUES**
   G. Pouraimis, A. Kotopoulis and P. Frangos, School of Electrical and Computing Engineering, National Technical University of Athens, Greece

2. **REVISITING ENHANCED AIS DETECTION RANGE UNDER DUCTING**
   Irina Sirkova, Laser Radars Lab, Institute of Electronics, Bulgarian Academy of Sciences, Bulgaria

3. **AN ANALYSIS OF UNCERTAINTY AND STATISTICS OF HIGH DYNAMIC RANGE ACOUSTIC SIGNALS**
   Ivan Simeonov,Vasil Levski National Military University, Veliko Tarnovo, Bulgaria

4. **NONSTANDART APPLICATIONS OF THE INFRASONIC AND HYDROACOUSTIC COMPONENTS OF THE INTERNATIONAL MONITORING SYSTEM OF NUCLEAR EXPLOSIONS**
   Tihomir Trifonov, Vasil Levski National Military University, Veliko Tarnovo, Bulgaria

5. **THEORETICAL AND EXPERIMENTAL DETERMINATION OF SOME PARAMETERS OF THE SIGNALS**
   Oleg Panagiev, Faculty of Telecommunications, Technical University of Sofia, Bulgaria

6. **EXPERIMENTAL SETUP FOR CONTROL, REGULATION AND SET UP OF OSCILLATOR FREQUENCIES IN LNB CONVERTER**
   Oleg Panagiev, Faculty of Telecommunications, Technical University of Sofia, Bulgaria

Break

13h 30min – 15h

SECOND SESSION

15h – 16h 30min

On-line presentation and discussions

Chairman: Prof. P. Frangos, School of Electrical and Computing Engineering, National Technical University of Athens, Greece

---

1. **MODELS OF DIFFUSION PROCESSES ON TRIANGULATED SURFACES**
   N. Ampilova, G. Doronin, St. Petersburg State University, St. Petersburg, Rusia

2. **A HUMAN SUPPORT SYSTEM IN A SMART HOME ENVIRONMENT**
   I. Nebogatikov, I. Soloviev, St. Petersburg State University, St. Petersburg, Rusia

3. **GUI FOR IMAGE FUSION IN MEDICAL IMAGES OF BRAIN**
   Diana S. Tsvetkova, Faculty of German Engineering Education and Industrial Management, Technical University of Sofia, Bulgaria,
   Veska Georgieva, Faculty of Telecommunications, Technical University of Sofia, Bulgaria

4. **A HYBRID APPROACH FOR BRAIN TUMOR DETECTION IN MRI IMAGES**
   Veska Georgieva, Faculty of Telecommunications, Technical University of Sofia, Bulgaria
   Veronika Katsarova, Faculty of German Engineering Education and Industrial Management, Technical University of Sofia, Bulgaria
   Lyubomir Laskov, Faculty of Telecommunications, Technical University of Sofia, Bulgaria

5. **CYBERSECURITY OF INFORMATION IN SPACE TELEMEDICINE**
   Evgeni Andreev, Veselka Radeva, Mariya Nikolova, N. Y. Vaptsarov NAVAL ACADEMY, Varna, Bulgaria

6. **OBJECTS TRACKING FROM VIDEO IN URBAN ENVIRONMENT BY LOW RANK RECOVERY**
   Ivo Draganov, Rumen Mironov, Faculty of Telecommunications, Technical University of Sofia, Bulgaria

CLOSING CONFERENCE

16h 30min – 17h

CONTACT US:

http://rcvt.tu-sofia.bg/CEMA/eth.html

Prof. Dr. Dimiter Dimitrov

Faculty of Telecommunication
Technical University of Sofia
8, Kliment Ohridsky str.
1756 Sofia, Bulgaria
Phone:++359 2 9652278
Fax: ++359 2 9652278
E-mail: dcd@tu-sofia.bg

Prof. P. Frangos

National Technical University of Athens
School of Electrical and Computer Engineering
9, Iroon Polytechniou Str. ,
157 73 Zografou, Athens, Greece
Phone : 00 30 210 772 3694
Fax : 00 30 210 772 2281
E-mail : pfrangos@central.ntua.gr

TABLE OF CONTENTS

1. **SEA STATE CHARACTERIZATION USING NORMALIZED EXPERIMENTAL ONE – DIMENSIONAL RADAR SIGNATURES AND FRACTAL TECHNIQUES** 1
   G. Pouraimis, A. Kotopoulis, P. Frangos

2. **REVISITING ENHANCED AIS DETECTION RANGE UNDER DUCTING** 6
   Irina Sirkova

3. **AN ANALYSIS OF UNCERTAINTY AND STATISTICS OF HIGH DYNAMIC RANGE ACOUSTIC SIGNALS** 10
   Ivan Simeonov

4. **NONSTANDART APPLICATIONS OF THE INFRASONIC AND HYDROACOUSTIC COMPONENTS OF THE INTERNATIONAL MONITORING SYSTEM OF NUCLEAR EXPLOSIONS** 15
   Tihomir Trifonov

5. **THEORETICAL AND EXPERIMENTAL DETERMINATION OF SOME PARAMETERS OF THE SIGNALS** 20
   Oleg Panagiev

6. **EXPERIMENTAL SETUP FOR CONTROL, REGULATION AND SET UP OF OSCILLATOR FREQUENCIES IN LNB CONVERTER** 27
   Oleg Panagiev

7. **MODELS OF DIFFUSION PROCESSES ON TRIANGULATED SURFACES** ... 33
   N. Ampilova, G. Doronin

8. **A HUMAN SUPPORT SYSTEM IN A SMART HOME ENVIRONMENT** 38
   I. Nebogatikov, I. Soloviev

9. **GUI FOR IMAGE FUSION IN MEDICAL IMAGES OF BRAIN** 43
   Diana S. Tsvetkova, Veska Georgieva

10. **A HYBRID APPROACH FOR BRAIN TUMOR DETECTION IN MRI IMAGES** 48
    Veska Georgieva, Veronika Katsarova, Lyubomir Laskov

11. **CYBERSECURITY OF INFORMATION IN SPACE TELEMEDICINE** 54
    Evgeni Andreev, Veselka Radeva, Mariya Nikolova

12. **OBJECTS TRACKING FROM VIDEO IN URBAN ENVIRONMENT BY LOW RANK RECOVERY** 58
    Ivo Draganov, Rumen Mironov

SEA STATE CHARACTERIZATION USING NORMALIZED EXPERIMENTAL ONE – DIMENSIONAL RADAR SIGNATURES AND FRACTAL TECHNIQUES

G. Pouraimis, A. Kotopoulis, P. Frangos

School of Electrical and Computing Engineering, National Technical University of Athens,
9, Iroon Polytechniou Str., 157 73 Zografou, Athens, Greece
Tel.: +30 210 772 3694; FAX: +30 210 772 2281; e-mail: pfrangos@central.ntua.gr

Abstract

This paper presents a novel method of sea state characterization by using several criteria, which are applied to normalized experimental Synthetic Aperture Radar (SAR) one–dimensional signatures (range profiles), provided to our research group by SET 215 Working Group on "SAR radar techniques". In previous Conference we had provided the "Fractal Dimension" and "Variance σ^2" criteria, while here we present the "Fractal Length" and "Power Spectrum Density - Least Squares" criteria. Note that concerning the first criterion ("Fractal Length"), this uses the so – called "Modified Fractal Signature" (MFS) or "blanket" method for calculating the "fractal length" of the radar range profiles. The main idea concerning this proposed technique is the fact that normalized SAR radar range profiles, corresponding to different sea states, produce different values of "Fractal Dimension" and "Fractal Length" for all angles of incidence examined here. As a result, a sea state characterization technique for two different sea states (turbulent and calm sea) is presented in this paper.

1. INTRODUCTION

Fractals can describe an unlimited number of complex patterns that resemble in different scales and are used as a mathematical tool for a variety of applications, such as image analysis and sorting, applied electromagnetism, etc. [1] – [7]. The indistinguishable structure on different scales is a basic feature of fractals. Accordingly, fractals can illustrate a certain very strong form of geometric complexity across multiple data sets, as well as SAR images. Synthetic Aperture Radar (SAR) images can be considered as fractals for a certain range of magnification. In addition, fractal objects have unique properties and features that may be related to their geometric structure.

Previous research in the area of sea clutter investigations by using radar techniques and fractal mathematics methods can be found in [8] – [20]. As opposed to those references, in the present paper, the main objective is to examine the sea state characterization problem by using real SAR backscattered data and fractal techniques (for the latter see, e.g., [21] – [29]). Then, in this paper of ours, we use four different criteria: the 'Fractal Dimension', the "Fractal Length", the "Variance σ^2", and the "Power Spectral Density - Least Squares". The first two criteria are considered here the main ones, following the method by Peleg et al. [21], which has also been applied in the past to real Synthetic Aperture Radar (SAR) images, using the "blanket" technique, to provide useful information about SAR image classification, as reported by Malamou et al. [22].

This paper uses the recorded sea clutter radar data, which were collected during the "NEMO 2014" trials in Taranto, Italy, using FFI (i.e., "Norwegian Institute of Defense", Oslo, Norway) PicoSAR X-band radar as input to a specific SET Working Group. The experiment took place in the Taranto bay in southern Italy on 23 and 24 September 2014. The first day the weather was quite windy, thus creating a rather turbulent sea, in comparison with the second day, during which the sea surface was almost calm.

2. PROBLEM GEOMETRY AND STATEMENT

The geometry of the sea state characterization problem is shown in Fig. 1. Here, a helicopter (with PicoSAR radar inside) rises vertically, whereas maintaining its steady position (latitude and longitude), and transmits electromagnetic (EM) radar pulses towards the sea. In addition, it records the azimuth angle with high sampling density in the grazing angle.

During the experiment performed by FFI in September 2014 (NEMO trials), the helicopter kept low vertical velocity and negligible horizontal velocity (helicopter movement from down to up). The first day (23/9/2014), the wind speed was reported in the range from 10 m/s to 12 m/s (rather high wind speed)

and the helicopter pilot kept the direction of the antenna beam up-wind (i.e., the direction of radar pulses - EM wave propagation in the opposite direction of the wind speed) within a 20° window in the horizontal (azimuthal) direction, as grazing angles θ_g (see Fig. 1) scanned from 3° to 37°. The time of the full grazing angle span was approximately 4 minutes.

During the second day (24/9/2014), the wind speed was very low (1 m/s–2 m/s, which sometimes died out locally) and the range of grazing angles was from 4° to 38° with a slight drift in the azimuth pointing angle of the bore sight of no more than 20°.

However, several practical questions arise about the characterization of a signal that embeds noise. To deal with the presence of noise in the signal, a method is presented here, which initially calculates the average of the range profiles (i.e., "range profile averaging"). For avoiding possible noise spikes in the signal, the number of N samples of the range profiles was set to be equal to 65, ensuring that this was sufficient to give the most accurate results.

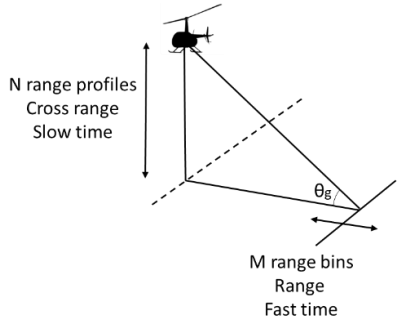

Figure 1. Geometry of the problem

Then the average of the distance profiles was normalized on a scale from 0 to 1 (i.e., "normalized range profiles") and the generated backscattered signal was transformed into the frequency domain (see Fig. 2 and 3 below).

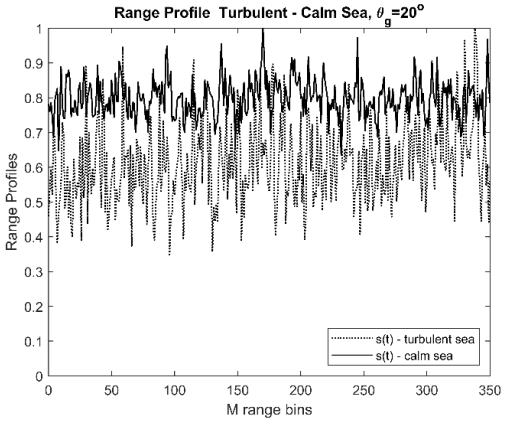

Figure 2. Representative PicoSAR radar range profiles at grazing angle θg = 20° for Day 1 (turbulent sea) and Day 2 (calm sea): time domain

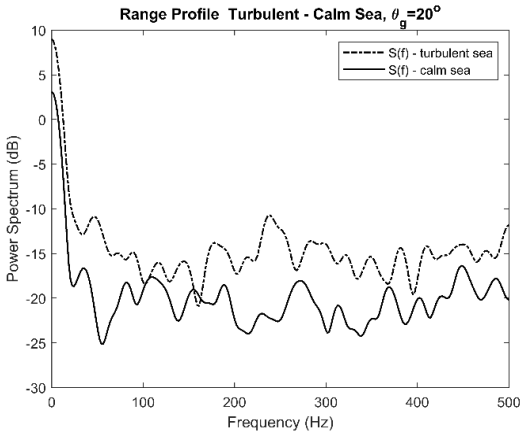

Figure 3. Representative PicoSAR radar range profiles at grazing angle θ_g = 20° for Day 1 (turbulent sea) and Day 2 (calm sea): frequency domain

Observing Fig. 2 and 3, the first day (turbulent sea), the range profiles take values from about 0.3 to 1, whereas during the second day (calm sea), the range profiles take values from 0.6 to 1 (in this case), i.e. smaller variance during the second day. Furthermore, in Fig. 4, the backscattered waves in the frequency domain (i.e., "spectral power") are shown.

3. SEA STATE CHARACTERIZATION RESULTS USING THE "FRACTAL LENGTH" AND "POWER SPECTRUM DENSITY - LEAST SQUARES" CRITERIA : NUMERICAL RESULTS

The sea state characterization criteria that are described in this paper are the "Fractal Length" and the "Power Spectral Density - Least Squares" criteria. Detailed information about all these criteria can be found at Ref. [30].

These criteria use the fractal theory and both fractal criteria use the blanket method, which was introduced by Peleg et. al. [21] and was used to characterize the texture of surfaces.

As mentioned above, the blanket method [3] is used here for the calculation of the fractal length and the fractal dimension of the range profiles in the frequency domain. Initially, in the paper by Peleg et. al. [21], the surfaces are classified based on the change of their properties in terms of the change of image resolution. Subsequently, Malamou et al. [22] and Tang et. al. [23] used the blanket method to characterize SAR images and document images, respectively.

The blanket method was proposed [21] to measure the area of irregular surfaces, which had been studied earlier by Mandelbrot [3] – [5]. The blanket method in one dimension, as applied in this paper,

considers that all points, which have a distance δ on both sides of a range profile, create an area of width 2δ, which is called "strip", defined by an upper and a lower blanket. The functions of the "upper" and "lower" curves of the range profile are provided by the following equations [21], [23]. Details on all that can be found at Ref. [30].

3.1. 'Fractal Length' Criterion results

This criterion for sea state characterization is performed by examining the logarithmic fractal length. The "Fractal Length" criterion calculates the logarithm of the fractal length of the normalized average signal for range profiles (averaging with N = 65 range profiles) in the frequency domain, using the blanket method, as briefly described above [30].

The "Fractal Length" criterion examines the difference between the fractal length for the scale δ = 1 and the fractal length logarithm for the scale of δ (the signal for scale δ = 1 is essentially identical to the backscattered signal), see Figures 4 and 5. Then the results for the grazing angles 10° and 25° are shown in Fig. 4 and 5.

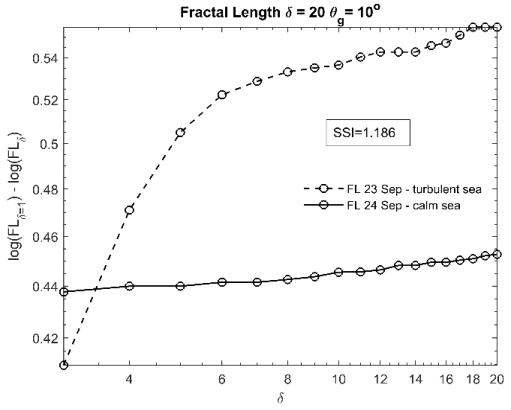

Figure 4. Logarithmic Fractal Length as a function of iteration δ for grazing angle 10°

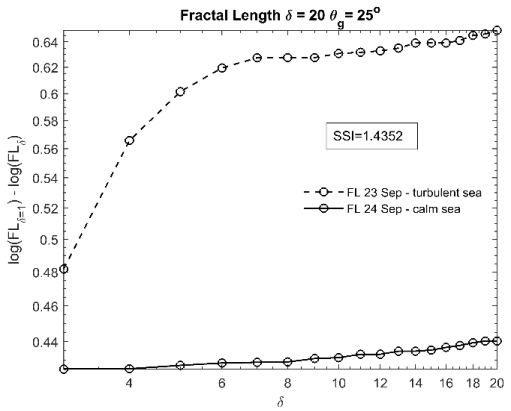

Figure 5. Logarithmic Fractal Length as a function of iteration δ for grazing angle 25°

Furthermore, the Sea State Index (SSI) is calculated for the 'fractal length' criterion. The Sea State Index of this criterion is the ratio of the mean logarithmic fractal length in the case of turbulent sea to the mean logarithmic fractal length for calm sea, in the frequency domain. As shown in Table I, the values of SSI here are higher than 1 for all values of grazing angle (i.e., from 5° to 35°), thus the fractal length criterion examined here is of high confidence.

TABLE I. Sea State Index (SSI) for 'fractal length' criterion for different grazing angles

SSI / Angle	Fractal Length
5°	1.272
10°	1.186
15°	1.437
20°	1.383
25°	1.435
30°	1.382
35°	1.563

3.2. Power Spectrum Density – Least Squares Approximation Criterion Results

The "Power Spectrum Density - Least Squares" criterion is used here to validate the results of the two main fractal criteria. The least squares approximations of the power spectrum density results, as lines of the form $\alpha x + \beta$, are shown in Figures 6 and 7 for the grazing angles of 10° and 25°, respectively. These Figures represent the power spectral density (PSD) versus the frequency on a log-log scale for turbulent and calm sea (see also [8], [9]).

Then, in Figures 6 and 7 it can be observed that the slopes of the lines of the least squares approximation (LSA) exhibit an absolute slope for the turbulent sea greater than the absolute slope value for the calm sea, something that is actually used as a criterion for characterizing the sea state. Then the corresponding numerical results are provided in Table II.

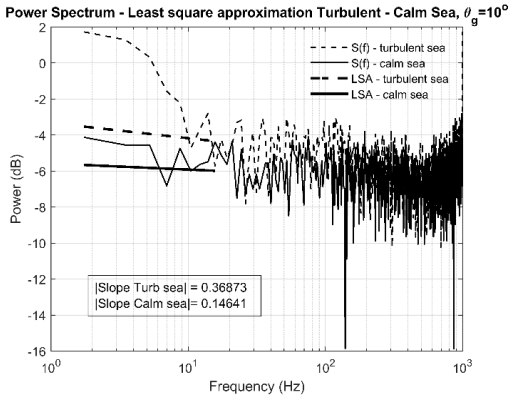

Figure 6. Power Spectrum Density and Least Squares slope for grazing angle 10°

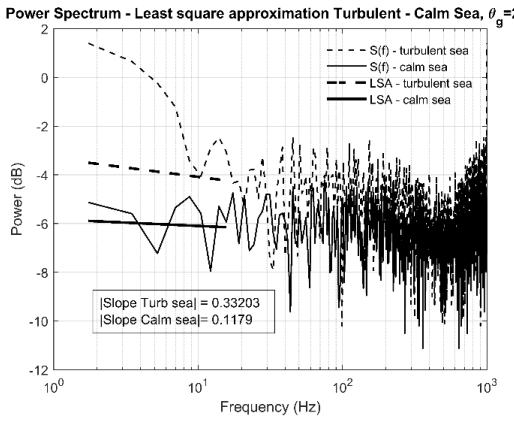

Figure 7. Power Spectrum Density and Least Squares slope for grazing angle 25o.

TABLE II. Absolute slope of least squares approximation results of power spectrum density for turbulent and calm sea

Sea State / Angle	Turbulent	Calm
5°	0.290	0.119
10°	0.368	0.146
15°	0.316	0.166
20°	0.300	0.148
25°	0.332	0.117
30°	0.346	0.115

Concluding, in a manner similar to that described in [8], [9], the "Power Spectrum Density – Least Squares" criterion can be used to characterize the sea state in a satisfactory way.

4. CONCLUSIONS

To summarize, this paper focused on the sea state characterization with the use of the two (2) criteria mentioned above (for further information on these methods, as well as the 'fractal dimension' and 'variance' criteria, the interested reader is referred to Ref. [30]).

These two (2) criteria were applied to the experimental one-dimensional signatures of a synthetic aperture radar (SAR) in the frequency domain (real radar data from sea surface) in two different sea states (turbulent and calm sea). The corresponding recorded sea clutter radar data were collected during the "NEMO 2014" trials in Taranto, Italy, 23–24/9/2014. An X-band PicoSAR airborne radar was used for that purpose by FFI (i.e., "Norwegian Institute of Defense", Oslo, Norway).

The above two (2) criteria were applied to the backscattered radar signals from the sea surface. Namely, to suppress the inherent radar receiver electronic noise, averaging of the radar range profiles was used (here with N = 65 range profiles) and subsequently the data were normalized on a scale from 0 to 1 (i.e., "normalized range profiles"). Finally, the range profiles generated as described above, were transformed to the frequency domain. Finally, the 'Sea State Index' (SSI) was calculated for the above criteria, which were found to be suitable for accurate sea state characterization.

5. FUTURE RESEARCH

In our future related research, we intend to validate the above mentioned criteria [all four (4) of them, see abstract above, as well as Ref. [30]] for sea state characterization for *simulated* backscattered radar data (range profiles) to be produced by a rigorous electromagnetic (EM) code, already developed by our research group. Furthermore, we intend to use fractal methods on the "full set of range profiles" [i.e., *three-dimensional (3D) fractal analysis* on the backscattered radar range profiles], rather than the essentially two-dimensional (2D) analysis of the range profiles, presented in this paper. Finally, the '*uniformity of the spectra'* of the range profiles, for 'calm' and 'turbulent' sea conditions respectively, can be more carefully examined by our research group in the near future.

6. ACKNOWLEDGMENT

The authors would like to thank SET-215 Working Group, and FFI Institute (i.e. 'Norwegian Institute of Defense', Oslo, Norway), in particular, for providing to us the real recorded sea clutter radar data which were collected during the 'NEMO 2014' trials in Taranto, Italy, and are shown in Figs. 2 above.

Furthermore, the authors acknowledge very useful discussions with Profs. N. Ampilova and I. Soloviev, St. Petersburg State University, Dept. of Mathematics and Informatics, in the area of 'fractal techniques', through the support by the 'International Mobility Program', National Technical University of Athens (NTUA), Greece.

References

[1] D. H. Werner and R. Mittra, "Fractal electrodynamics: Surfaces and superlattices", in Frontiers in Electromagnetics. Wiley-IEEE Press, 2000, pp. 1–47. DOI: 10.1109/9780470544686, ch1.

[2] K. Falconer, Fractal Geometry: Mathematical Foundations and Applications. J. Wiley and Sons, 1990.

[3] B. B. Mandelbrot, The Fractal Geometry of Nature. New York: W. H. Freeman and Company, 1977.

[4] B. B. Mandelbrot, Fractals: Form, Chance and Dimension. W. H. Freeman and Company, 1977.

[5] B. Mandelbrot, "How long is the coast of Britain? Statistical self-similarity and fractional dimension", Science, vol. 156, no. 3775, pp. 636–638, 1967. DOI: 10.1126/science.156.3775.636.

[6] R. Esteller, G. Vachtsevanos, J. Echauz, and B. Lilt, "Comparison of fractal dimension algorithms using synthetic and experimental data", in Proc. of ISCAS'99, IEEE International Symposium on Circuits and Systems, 1999. DOI: 10.1109/ISCAS.1999.778819.

[7] B. Li, Y. Xu, J. Zhang, and L. Cui, "Study on calculation models of curve fractal dimension", in Proc. of 6th International Conference on Natural Computation (ICNC 2010), 2010, pp. 3072–3079. DOI: 10.1109/ICNC.2010.5584690.

[8] T. Lo, H. Leung, J. Litva, and S. Haykin, "Fractal characterization of sea-scattered signals and detection of sea-surface targets", IEE Proceedings F (Radar and Signal Processing), vol. 140, no. 4, pp. 243–250, 1993. DOI: 10.1049/ip-f-2.1993.0034.

[9] [9] J. Hu, W.-W. Tung, and J. Gao, "Detection of low observable targets within sea clutter by structure function based multifractal analysis", IEEE Transactions on Antennas and Propagation, vol. 54, no. 1, pp. 136–143, 2006. DOI: 10.1109/TAP.2005.861541.

[10] [10] J. Chen, T. K. Y. Lo, H. Leung, and J. Litva, "The use of fractals for modeling EM waves scattering from rough sea surface", IEEE Transactions on Geoscience and Remote Sensing, vol. 34, no. 4, pp. 966–972, 1996. DOI: 10.1109/36.508413.

[11] F. Berizzi, E. Dalle Mese, and G. Pinelli, "One-dimensional fractal model of the sea surface", IEE Proceedings - Radar, Sonar and Navigation, vol. 146, no. 1, pp. 55–64, 1999. DOI: 10.1049/ip-rsn:19990259.

[12] F. Berizzi and E. Dalle-Mese, "Fractal analysis of the signal scattered from the sea surface", IEEE Transactions on Antennas and Propagation, vol. 47, no. 2, pp. 324–338, 1999. DOI: 10.1109/8.761073.

[13] G. Lixin and Z. Wu, "Fractal model and electromagnetic scattering from time-varying sea surface", Electronics Letters, vol. 36, no. 21, pp. 1810–1812, 2000. DOI: 10.1049/el:20001199.

[14] Z. Li and Y.-Q. Jin, "Bistatic scattering from a fractal dynamic rough sea surface with a ship presence at low grazing-angle incidence using the GFBM/SAA", Microwave and Optical Technology Letters, vol. 31, no. 2, pp. 146–151, 2001. DOI: 10.1002/mop.1383.

[15] F. Berizzi and E. Dalle-Mese, "Scattering from a 2-D sea fractal surface: Fractal analysis of the scattered signal", IEEE Transactions on Antennas and Propagation, vol. 50, no. 7, pp. 912–925, 2002. DOI: 10.1109/TAP.2002.800695.

[16] C. Yang and H. Zhou, "The study of electromagnetic scattering by a target with fractal rough surface", in Proc. of 6th International Symposium on Antennas, Propagation and EM Theory, 2003, pp. 488–491. DOI: 10.1109/ISAPE.2003.1276734.

[17] Y. Li, X. Lv, K. Liu, and S. Zhao, "Fractal-based target detection within sea clutter", Acta Oceanol. Sin., vol. 33, no. 9, pp. 68–72, 2014. DOI: 10.1007/s13131-014-0519-1.

[18] A. Jayaprakash, G. Ramachandra Reddy, and N. S. S. R. K. Prasad, "Small target detection within sea clutter based on fractal analysis", Procedia Technology, vol. 24, pp. 988–995, 2016. DOI: 10.1016/j.protcy.2016.05.217.

[19] L. Gong et al., "Characterization and prediction of complex natural fractures in the tight conglomerate reservoirs: A fractal method", Energies, vol. 11, no. 9, p. 2311, 2018. DOI: 10.3390/en11092311.

[20] H. Pan et al., "Roughness change analysis of sea surface from visible images by fractals", IEEE Access, vol. 8, pp. 78519–78529, 2020. DOI: 10.1109/ACCESS.2020.2990161.

[21] S. Peleg, J. Naor, R. Hartley, and D. Avnir, "Multiple resolution texture analysis and classification", IEEE Transactions on Pattern Analysis and Machine Intelligence, vol. PAMI-6, no. 4, pp. 518–523, Jul. 1984. DOI: 10.1109/TPAMI.1984.4767557.

[22] A. Malamou, C. Pandis, P. Frangos, P. Stefaneas, A. Karakasiliotis, and D. Kodokostas, "Application of the modified fractal signature method for terrain classification from synthetic aperture radar images", Elektronika ir Elektrotechnika, vol. 20, no. 6, pp. 118–121, 2014. DOI: 10.5755/j01.eee.20.6.7281.

[23] Y. Y. Tang, H. Ma, D. Xi, X. Mao, and C. Y. Suen, "Modified fractal signature (MFS): A new approach to document analysis for automatic knowledge acquisition", IEEE Transactions on Knowledge and Data Engineering, vol. 9, no. 5, pp. 747–762, 1997. DOI: 10.1109/69.634753.

[24] S. Savaidis, P. Frangos, D. L. Jaggard, and K. Hizanidis, "Scattering from fractally corrugated surfaces using the extended boundary condition method", Journal of the Optical Society of America A, vol. 14, no. 2, pp. 475–485, 1997. DOI: 10.1364/JOSAA.14.000475.

[25] N. Lin, H. P. Lee, S. P. Lim, and K. S. Lee, "Wave scattering from fractal surfaces", Journal of Modern Optics, vol. 42, no. 1, pp. 225–241, 1995. DOI: 10.1080/09500349514550181.

[26] D. Jaggard and X. Sun, "Scattering from fractally corrugated surfaces", Journal of the Optical Society of America A, vol. 7, no. 6, pp. 1131–1139, 1990. DOI: 10.1364/JOSAA.7.001131.

[27] A. K. Sultan-Salem and G. L. Tyler, "Validity of the Kirchhoff approximation for electromagnetic wave scattering from fractal surfaces", IEEE Transactions on Geoscience and Remote Sensing, vol. 42, no. 9, pp. 1860–1870, 2004. DOI: 10.1109/TGRS.2004.832655.

[28] R. Xin-Cheng and G. Li-Xin, "Fractal characteristics investigation on electromagnetic scattering from 2-D Weierstrass fractal dielectric rough surface", Chinese Physics B, vol. 17, no. 8, p. 2956, 2008. DOI: 10.1088/1674-1056/17/8/032.

[29] A. Iodice, A. Natale, and D. Riccio, "Kirchhoff scattering from fractal and classical rough surfaces: Physical interpretation", IEEE Transactions on Antennas and Propagation, vol. 61, no. 4, pp. 2156–2163, 2013. DOI: 10.1109/TAP.2012.2236531.

[30] G. Pouraimis, A. Kotopoulis, B. Massinas and P. Frangos, 'Sea State Characterization using Experimental One – Dimensional Radar Signatures and Fractal Techniques', 'Elektronika ir Elektrotechnika' Journal, Vol. 27, No. 3, May/June of 2021. DOI: 10.5755/j02.eie.28906

REVISITING ENHANCED AIS DETECTION RANGE UNDER DUCTING

Irina Sirkova

Laser Radars Lab, Institute of electronics, Bulgarian Academy of Sciences,
Tzarigradsko chaussee 72, 1784 Sofia, Bulgaria
irina@ie.bas.bg

Abstract

This report studies the propagation of Automatic Identification System frequencies under various tropospheric ducting and sea surface conditions with the parabolic wave equation method. The aim is to examine the influence of sea surface roughness on the possibility to enlarge the AIS detection range under ducting.

1. INTRODUCTION

Initially designed as a ship reporting system for collision avoidance, the AIS (Automatic Identification System) nowadays has enlarged applications beyond the situational awareness and security. The AIS has become part of the VHF Data Exchange System concept [1] which increases the requirements to the AIS performance and reliability. At the same time, the growing importance of the AIS traffic poses the need to monitor shipping at distances greater than can be achieved via the conventional propagation mechanisms like line-of-sight (LoS) and diffraction. Thus the long range detection capability becomes a key AIS characteristic. Among the factors that can influence the long range detection of AIS messages the ducting anomalous propagation mechanism, often present over the sea, is identified as a major candidate [2]. This clear-air propaga-tion mechanism is due to deviation in tropospheric refractivity N (N=(n-1)10^6) from the standard conditions caused by temperature and water vapour changes. The spatial change of n is larger with height than with range and generally the horizontal variations of n can be neglected [3]. The appearance of negative vertical gradient of the modified refractivity M (M=N+(z/a_e)10^6, with z the height above the sea surface and a_e - the Earth's radius, indicates the presence of tropospheric duct [3]. For practical purposes the average behaviour of the modified refractivity M(z) is often approximated with piecewise-linear profile. On Fig. 1 are schematically presented the M(z) profiles for the four duct types with essential parameters indicated.

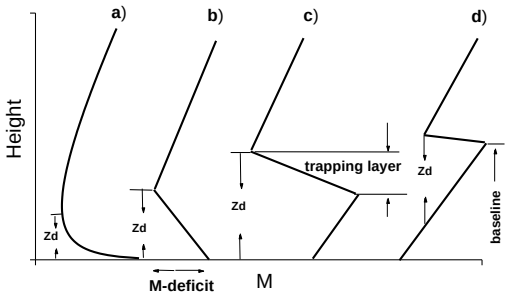

Figure 1. a) evaporation, b) surface, c) surface-based, d) elevated duct, zd – duct thickness

The complicated maritime conditions require sophisticated propagation methods. The paraxial approximation to the wave equation, known as the parabolic equation (PE), allows correct accounting simultaneously for the strong refraction under ducting, dif-fraction around the Earth's curvature, reflection and scattering from the rough sea surface, and antenna pattern [4, 5]. This report studies the propagation of AIS frequencies under various tropospheric ducting and sea surface conditions with the PE method. The aim is to examine the influence of sea surface roughness on the possibility to enlarge the AIS detection range under ducting.

2. METHOD DESCRIPTION

In this study 2D narrow-angle forward-scatter scalar PE is used as implemented in "Advanced propagation model (APM) Computer software configuration item (CSCI) documents", Space and Naval Warfare Systems Center Tech. Doc. 3145, which allows finding a full-wave solution to the AIS signal propagation problem in terms of path loss, PL (PL in dB):

$$PL = 20\log\left(\frac{4\pi r}{\lambda}\right) - PF\ , \qquad (1)$$

here λ is the free-space wavelength, r is the distance between the corresponding points and PF is the propagation factor (in dB) defined as the square of the ratio of the electric field amplitude E received at a given point under specific conditions to the amplitude of the electric field E_0 received at the same point under free-space conditions where E participates with its polarization component which coincides with the polarization of E_0 [3]. In this study, the initial field is provided by an omni directional antenna. Equation (2) gives the expression of the PF in terms of the reduced PE field, $U(x,z)$, which comes from the APM routines:

$$PF = 20\log|U(x,z)| + 10\log(r) + 10\log(\lambda)\ . \qquad (2)$$

Two international channels in the VHF maritime mobile band centered at 161.975 MHz and 162.025 MHz are allocated to the AIS. Later in the calculations the F=161.975 MHz is used. The examples of duct parameters have been taken from among the typical ones for the Bulgarian Black sea shore [6]. In order to preliminary assess the trapping of the AIS frequencies, well known formula for maximum wave length, λ_{max}, trapped in a duct is used [7]:

$$\lambda_{\max} = \frac{2}{3} C z_d (\Delta M)^{3/2}\ , \qquad (3)$$

where z_d is the duct thickness, ΔM is the M-deficit, see Fig. 1, and C=3.77x10^{-3} for surface and surface-based ducts. In this report these two types of ducts have been studied: the evaporation duct, even though the most widespread over the sea, is not able to trap the AIS frequencies with its maximal height of 40 m, whereas the elevated ducts have been considered to have weak influence due to there relatively great height above the sea surface. Also, surface and surface-based ducts are less sensitive to frequency than evaporation ducts and can extend over the ocean for several hundreds of kilometers and last for multiple days.

A trans-horizon path supposes reflections from the sea surface, therefore the sea surface roughness should be accounted for. Here this is done in the framework of the "effective" reflection coefficient, R_{eff}, concept in which the Fresnel reflection coefficient, R_F, is multiplied by a roughness reduction factor R_{rf} [4]:

$$R_{eff} = R_{rf} R_F\ , \qquad (4)$$

$$R_{rf} = R_{M-B} = \exp\left[-2k^2\sigma_h^2 \sin^2(\alpha)\right] \mathrm{x}\ \mathrm{I}_0\left[2k^2\sigma_h^2 \sin^2(\alpha)\right]. \qquad (5)$$

In (5) the Miller-Brown roughness reduction coefficient, $R_{M\text{-}B}$, is used [8] where σ_h is the standard deviation of the sea surface height h, I_0 is the modified Bessel function of the first kind of order zero, k is the free-space wave number and α is the local grazing angle measured with respect to the mean plane of the sea surface. The $R_{M\text{-}B}$ assumes the sea wave amplitude is Gaussian distributed with zero mean, i.e. in (5) σ_h=h_{rms} where h_{rms} is the root mean square deviation of the surface height. Note that the $R_{M\text{-}B}$ refers to the forward coherent reflected field (i.e. the diffuse scattered field is neglected as well as the small perturbations of the sea surface) and does not account for the shadowing and multiple scattering. The only parameter related to sea surface roughness in $R_{M\text{-}B}$ is the h_{rms} which can be expressed entirely in terms of the wind speed. In (5) the quantity 2kh_{rms}-sin(α) is the Rayleigh roughness parameter for the surface, [4], that is often used as a criterion for the degree of roughness. It is to note that when the grazing angles are very small (both ducting propagation and ship-to-ship propagation suppose small grazing angles) $R_{M\text{-}B}$ tends to 1 and thus the influence of the roughness is reduced. Nevertheless, the wavelength of AIS frequencies is about 1.85 m, i.e. it is of the same order as sea height variations in high sea states; hence, a roughness reduction factor is to be introduced to account for the reduction of the Fresnel reflection coefficient from flat surface.

There is a variety of formulae relating h_{rms} to the wind speed and sea state [9, 10] depending on the sea wave spectrum used for their obtaining. In this report the relation corresponding to sea wave spectra of Pierson-Moskowitz type is applied [10]:

$$h_{rms} = 0.0051 U_{10}^2\ , \qquad (6)$$

where U_{10} is the wind speed in m/s at h=10 m. The dielectric characteristics of the sea surface are calculated as functions of frequency following "Propagation in Non-Ionized Media", CCIR 1986, vol.5.

3. RESULTS AND DISCUSSION

The first example of ducted propagation refers to a surface duct with bilinear profile (see Fig. 1 (b)) and parameters z_d=100 m, ΔM=45 M-units, antenna height h_a=10 m, F=161.975 MHz, horizontal polarization (HOR) and smooth sea surface. It is to note that, following relation (3), this duct requires

λ_{max}<1.68 m; this means that AIS frequencies (λ around 1.85 m) will not be (completely) trapped. However, the transition from ducting to non-ducting conditions (and vice versa) for frequencies with λ around λ_{max} is gradual and those frequencies will have significantly extended propaga-tion/ detection range in comparison to the standard troposphere case, see Fig. 2 and Fig. 3. On Fig. 2 is shown path loss versus range and height. Figure 3 provides the *PL* for two vertical cuts at fixed range *FixR*=20 km and *FixR*=25 km (red and black line); for comparison are given the respective cuts for standard troposphere (StanTrop) - green and blue line. Even for these relatively short distances, 20 km and 25 km, the *PL* decrease under ducting is clearly seen, especially for the most important first 50 meters above the sea surface. With some certainty it can be expected that under similar conditions the AIS detection range will be increased.

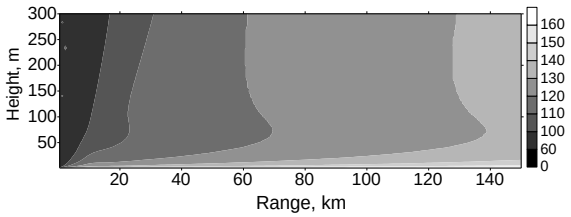

Figure 2. *PL* for surface duct

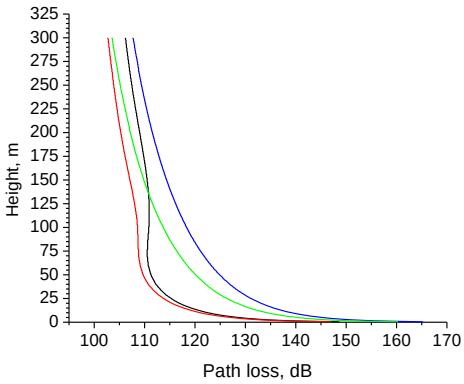

Figure 3. PL for FixR=20 km (red – surface duct, green - StanTrop) and FixR=25 km (black – surface duct, blue - StanTrop)

The next four figures, Fig.4 - Fig.7, refer to a surface-based duct modelled with tri-linear profile (see Fig. 1 (c)) with parameters as follows: trapping layer base height 113 m, z_d=268 m, ΔM=23 M-units, the slopes of the profile below and above the trapping layer correspond to the standard troposphere. The AIS frequencies are trapped by this duct. The *PL* for h_a=20 m and HOR is shown on Fig. 4 for standard troposphere, smooth and rough sea (U_{10}=9 m/s). On Fig. 5 are shown *PL* curves for fixed height FixH=h_a=20 m for the tri-linear duct and smooth sea: black curve refers to HOR, red for VER (vertical polarization); for comparison the respective curves for StanTrop are also given (in blue and green). Clearly seen is the difference between the two polarizations. Note that close to the two *PL* peaks the *PL* under ducting exceeds that of standard troposphere. After the second peak ducting decreases significantly the *PL* but it exists a "skip zone" between 20th and 60th km, see Fig. 4 (b).

On Fig. 6 are shown *PL* curves for fixed range *FixR*=35 km (close to the first *PL* peak, see Fig. 5) for the same tri-linear duct as on Figs. 4 and 5, and HOR: the red curve refers to smooth sea, the StanTrop *PL* is given in blue, the black curve shows the influence of sea surface roughness introduced through formulas (4)-(6) for U_{10}=9 m/s. Figure 7 presents the *PL* for the same conditions as on Fig. 6 but only the area of interest below the first 50 meters above the sea is given: red - smooth sea; black - rough sea, U_{10}=9 m/s; blue - rough sea, U_{10}=15 m/s. As expected, the influence of ducting prevails over that of sea roughness which is negligible except in the area close to the *PL* peak. A possible reason is change of the grazing angles to the sea in the "skip zone" so that the influence of the R_{rf}=$R_{M\text{-}B}$ is increased. The increased roughness, U_{10}=15 m/s, "blurs" the *PL* pattern, see also Fig. 4 (c). The presence of "skip zones" indicates that ducting may not always be advantageous for the detection range and this may by aggravated by the sea roughness.

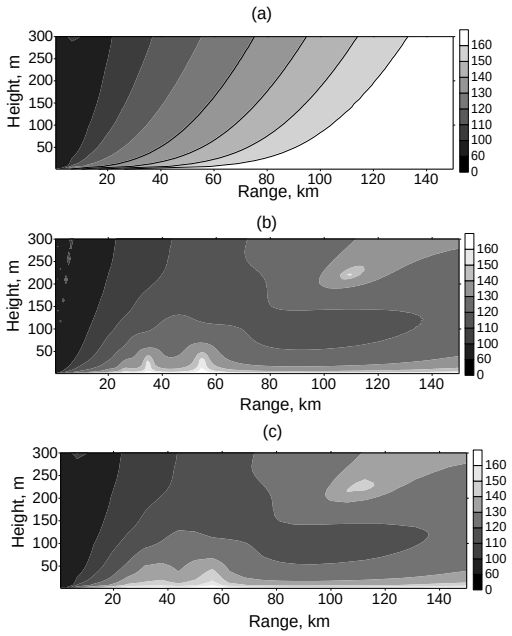

Figure 4. *PL* for h_a=20 m: (a) StanTrop, (b) tri-linear duct, smooth sea, (c) tri-linear duct, rough sea

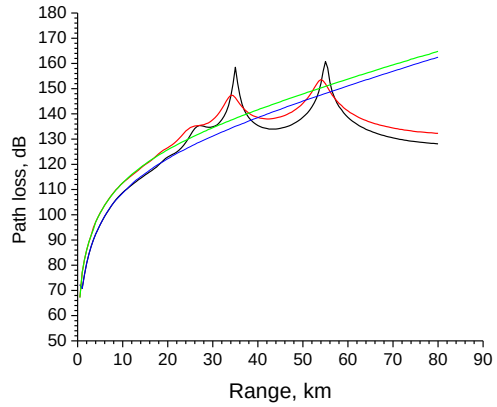

Figure 5. *PL* for FixH=h_a=20 m, tri-linear duct, smooth sea: black – HOR, red – VER, blue & green – HOR & VER for StanTrop

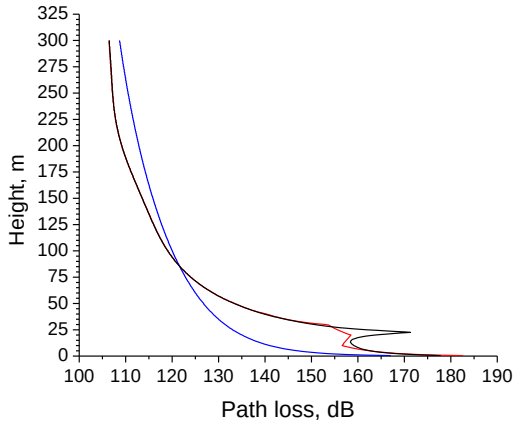

Figure 6. PL for FixR = 35 km, HOR, tri-linear duct: red - smooth sea, black – rough sea, blue – StanTrop

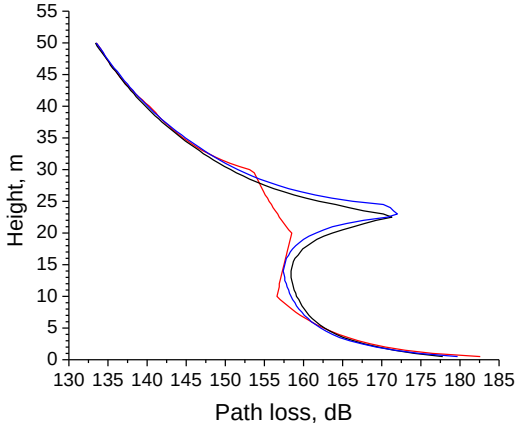

Figure 7. PL for FixR=35 km, HOR, tri-linear duct: red - smooth sea, black – rough sea, U10=9 m/s, blue - rough sea U10=15 m/s

4. CONCLUSION

The results indicate that to be reliable and of practical use the extension of the detection range through ducting requires:

- a good preliminary assessment of the duct types and parameters;
- accounting for sea roughness for sea state 4 and higher (according to the scale relating wind speed to sea state [10]); even though the roughness has rather weak influence, it may increase the *PL* in the "skip zones";
- additional investigations that account for the rocking of the ship, influence of breaking waves, etc.

5. ACKNOWLEDGMENTS

This work was supported by the Ministry of Education and Science of Bulgaria (support for ACTRIS BG, part of the Bulgarian National Roadmap for Research Infrastructure).

References

[1] F. Lázaro, R. Raulefs, W. Wang et al. "VHF Data Exchange System (VDES): an enabling technology for maritime communications", CEAS Space J, Vol. 11, 2019, 55–63.

[2] ITU-R M.2123 "Long range detection of automatic identification system (AIS) messages under various tropospheric propagation conditions", 2007.

[3] D.E. Kerr, (Ed.) Propagation of Short Radio Waves, Peter Peregrinus, London, UK, 1987.

[4] M. Levy, Parabolic Equation Methods for Electromagnetic Wave Propagation, IEE electromagnetic waves series 45, UK, 2000.

[5] I. Sirkova, "Brief Review on PE Method Application to Propagation Channel Modeling in Sea Environment", CEJE, Vol. 2, No. 1, 2012, 19-38.

[6] I. Sirkova, "Duct occurrence and characteristics for Bulgarian Black sea shore derived from ECMWF data", J Atmos Sol-Terr PHy, Vol. 135, 2015, 107-117.

[7] J. D. Turton, D. A. Bennetts, and S.F.G. Farmer, "An introduction to radio ducting," Meterorolog. Mag., Vol. 117, 1988, 245-254.

[8] A. R. Miller, R. M. Brown, and E. Vegh, "New Derivation for the Rough Surface Reflection Coefficient and for the Distribution of Sea-Wave Elevations", IEE Proc.-H, Vol. 131, 1984, 114–116.

[9] T. P. Leonard, I. Antipov, and K.D. Ward, "A comparison of radar sea clutter models", Conf. Radar 2002, 15-17 Oct 2002, Edinburgh, UK, 429-433.

[10] L. B. Wetzel, "Sea clutter", Naval Res. Lab. Report 9244, Washington, USA, 1990, 41 p.

AN ANALYSIS OF UNCERTAINTY AND STATISTICS OF HIGH DYNAMIC RANGE ACOUSTIC SIGNALS

I. Simeonov

Vasil Levski National Military University, Veliko Tarnovo, Bulgaria
76, Bulgaria Blvd., 5000, Veliko Tarnovo, Bulgaria
Tel. +359 62 618724, Fax. +359 62 618899, E-mail: ivanov_ivan@nvu.bg

Abstract

In this paper, a number of large dynamic range acoustic signals statistics has been presented based on continuous wavelet transform. Some typical examples from battlefield acoustics and from musical acoustics are considered. Therefore, a specialized platform and a measuring microphone with the required features are used in field experiments. The characteristic acoustic environment signature and background noise features for some concrete setup are described. Possible directions for using these technics for signal statistics analysis for retrieving useful information, based on Shannon entropy, are outlined. The datasets consisting of the raw data and metadata from bell ringing and gunfire, and noise recordings are estimated. The wavelet transform was of particular importance here, as it provides both constant-bandwidth analysis that correlates with sound perception and optimal resolution. The discussed problems by means of continuous wavelet transform (CWT) and decomposition (or Shannon) entropy are approached. The results can be used in various areas of acoustics and electrodynamics.

1. INTRODUCTION

In the recent years, some application of modern acoustic methods in interdisciplinary fields and discovery of the difficulties when signal processing and storing of high dynamic range acoustic data, such as music, noise of natural phenomena, battlefield acoustic, and others was regarded [1, 2, 3].

Many acoustic data from field experiments have been collected since 2008 at different sites.

Wavelet analysis offers a way to process this acoustic data collection and it provides possibility to made interesting considerations about their characteristics.

The analysis based on Shannon entropy have been powerful and useful in determining the noise influence.

The aim is presenting one direction for using technics for signal statistics analysis for retrieving useful information, based on Shannon entropy and wavelet processing.

2. SHANNON ENTROPY PROPERTIES IN ACOUSTIC DATA PROCESSING

In Donoho et all work, [4] is discussed some of the lessons of harmonic analysis in the XX century and the authors made this interesting possible connection between the compression, and not only compression, of real data, concerns random, and the deterministic objects analysis following Tikhomirov's words:

"our vast mathematical world" is itself divided into two parts, as into two kingdoms. Deterministic phenomena are investigated in one part, and random phenomena in the other.

To Kolmogorov fell the lot of being a trailblazer in both kingdoms, a discoverer in their many unexplored regions he put forth a grandiose programme for a simultaneous and parallel study of the complexity of deterministic phenomena and the uncertainty of random phenomena, and the experience of practically all his creative biography was concentrated in this programme.

From the beginning of this programme, the illusory nature of setting limits between the world of order and the world of chance revealed itself" [4,5].

The ideas of entropy of the signal or signal uncertainty and its measure (bits per signal units) was defined in communication theory.

In Stratonovich work, [6] Shannon entropy for a continuous random variable with p.d.f. $p(\xi)$ is defined as an expectation:

$$H_\xi = \mathrm{E}[p(\xi)] == -\int_{\mathbf{X}} p(\xi)\ln p(\xi)\,d\xi$$

or $H_\xi = -\int_{\mathbf{X-\Lambda-\Lambda_0}} \ln\left(\frac{dP}{dv}\right) P(d\xi)$, in case $\nu_0(\xi) = dv/d\xi = 1$.

In other side Shannon entropy can be defined with Kullback–Leibler divergence as:

$$\mathrm{H}(\boldsymbol{X}) = \mathrm{E}[\mathrm{I}_{\boldsymbol{X}}(x)] = \log(N) - D_{KL}\big(p_{\boldsymbol{X}}(x) \parallel P_U(\boldsymbol{X})\big).$$

So, H(***X***) is the number of bits which would have to be transmitted to identify ***X*** from *N* equally likely possibilities, less the relative entropy of the uniform distribution on the random variates of ***X***, $P_U(\boldsymbol{X})$ from the true distribution P(***X***).

The *relative entropy* or *Kullback–Leibler distance* between two probability mass functions *p(x)* and *q(x)* is defined, [7] as

$$D_{KL}(p \parallel q) = \sum_{x \in \mathcal{X}} p \log \frac{p}{q} = E_P \log \frac{p(X)}{q(X)}$$

Some useful properties of Kullback–Leibler divergence was demonstrated also in R. Angelova-Slavova's works [8, 9].

The known analogy with quantum systems, is in Sanchis-Alepuz paper [10] where the Shannon's information entropy defined by:

$$Su = -\int \mathcal{P}(\mathrm{r}) \ln \mathcal{P}(\mathrm{r}) d\mathrm{r}$$

Probability distribution function $\mathcal{P}(\mathrm{r})$ similarly to electronic density distribution here is normalizing the square of the displacement field of a given acoustic level

$$\mathcal{P}(\mathrm{r}) = |u(\mathrm{r})|^2 / \int |u(\mathrm{r})|^2 d\mathrm{r},$$

and this quantity gives the uncertainty of the localization of sound in acoustics problems.

3. WAVELET ANALYSIS AND SHANNON ENTROPY

The wavelet transform is used to decompose a mixture of signals and noise, into components at different resolutions and make some conclusions about noise features.

It is known that the finer scales in the continuous wavelet transform (CWT) gives a higher-fidelity signal analysis. It can be better describe oscillations or localize signal transients, with the CWT than with the discrete wavelet transforms.

One regard to wavelets, which can be viewed as an information processing technique can be found in Oliveira's work, [11] where the concept of wavelet mutual information between a signal and an analyzing wavelet is introduced.

The Shannon entropy of some orthogonal wavelets, like Daubechies, Symmlets, Coiflets, that cannot be described by analytical expressions can be found by using the so-called two-scale relationship of a multiresolution analysis.

In [11] a few simple discrete signals were analyzed in order to gain insight into the information theory approach for multiresolution analysis. One possible method for measurement of entropy of discrete signal wavelet packets, [12,13] is expressed as:

$$\mathrm{WPE}_{\mathrm{N}} = -\sum p_{j,n} \log p_{j,n}$$

where $\mathrm{p_{j,n}} = \mathrm{E_{j,n}}/\mathrm{E_{tot}}$ - relative energy for scale j,

$$\mathrm{E_{j,n}} = \sum_{\mathrm{k}} \left|\mathrm{d_{j,n}}(k)\right|^2, \ \mathrm{E_{tot}} = \sum_{\mathrm{n}} \mathrm{E_{j,n}}$$

$$\mathrm{p_{j,n}} = \frac{\sum_k \left| 2^{\frac{\mathrm{j}}{2}} \int_{-\infty}^{\infty} \mathrm{s(t)}\, \psi_{\mathrm{n}}\left(2^{-\mathrm{j}}\mathrm{t} - \mathrm{k}\right) \mathrm{dt} \right|^2}{\sum_{\mathrm{n}} \mathrm{E_{j,n}}}$$

$\mathrm{s(t)}$ is original signal,

j, n, k represents the scale, band, and surge parameter, respectively.

Equation for $\mathrm{WPE_N}$ uses the Shannon method to calculate WPE. The N notation in $\mathrm{WPE_N}$ is used to denote the level of decomposition used in Wavelet packet decomposition.

The idea is that the accuracy of the selected wavelet basis is higher when the entropy is small.

4. WAVELET ANALYSIS AND SHANNON ENTROPY OF EXPERIMENTAL ACOUSTIC DATA

The interaction of the acoustic wave with objects, such as the ground, obstacles, the effects of reverberations, first reflections, absorption, interference and diffraction, turbulence etc. will change the registered sound pictures in real setups, [14,17].

The sound picture and noise level is varying in accordance of type of concrete space: close or free space, in dependence of source and receiver points placement. They change depending on the local parameters as temperature, wind speed and direction, air pressure and humidity etc.

In the next it was made the analysis of a set of experimental data and it was found the wavelet entropies of the different sound records.

First it was regarded the unique bell sounds in close space. The signals, see project Bell [1,3] denoted as Melnik2-1220 AD, was registered inside the hall in National Historical Museum in Sofia. In the figures 1a) and b) was shown some bell strike waveforms (ringing) in time.

Zoomed fragment of last bell strike in the time scale are shown in Fig.1b).

Second signal, illustrated on a Fig.2 consist a parts from time signal from the first blast from 122 mm 2S1 howitzer ("Gvozdika ") see [15], where in a) is shown the signal captured from two blasts from the two howitzers ("Salvo"), in b) the first from two blasts, 1024 samples.

And in third, record of noise of hailstone strikes, plus noise of auto alarms was regarded, see fig.3a), and zoomed part in Fig.3 b). The conditions for hail dropping strikes in concrete urban environments was: 20 May 2013, see [16].

This raw data was exported in MatLab and here were determined Shannon entropy coefficients for the wavelet tree for Daubechies3 wavelet level 3. Fig. 4 shows wavelet packets for three parts of bel ringing waveform (Fig. 1).

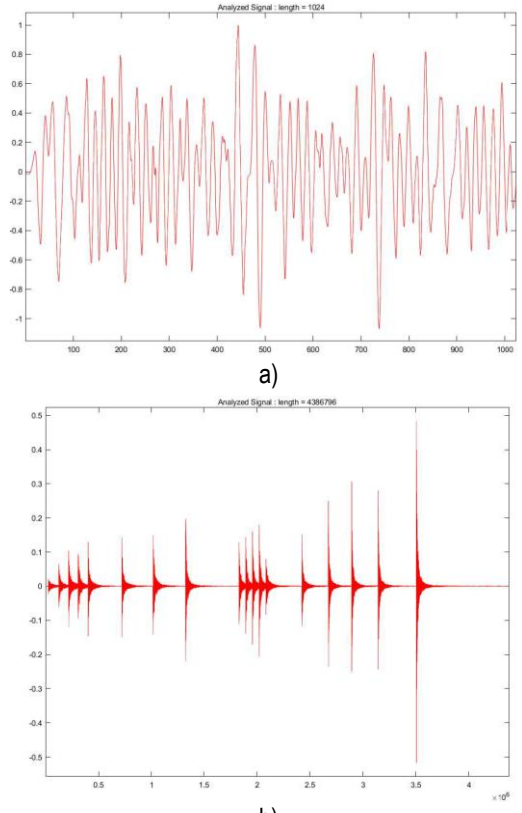

a)

b)

Figure 1. Waveforms of unique bell stroke (XIII cent.), a) ringing, on the b) it was separated only last bell ring

The wavelet packet entropies for concrete bel ringing signals in hall, totally 3 examples (noise, noise and part of ring, ring) were calculated and some results are shown in table 1. In table is shown entropies for the simulated noise with normal and uniform distribution.

Analogically wavelet packet entropies for the signals from blast fig. 2 and hail strikes fig. 3 were calculated. Part of results is shown in table 3.

From wavelet packet entropies presented in table 1,2 can be seen that for noise and for signal with noise the coefficients of Shannon entropy ShE(1,1) has higher values, than other situations.

Then the proportion of ShE(1,0) and ShE(1,1), and ShE(j,0) and ShE(j,1) i.e. entropy of approximation coefficients to detail coefficients may be parameter for noise discrimination.

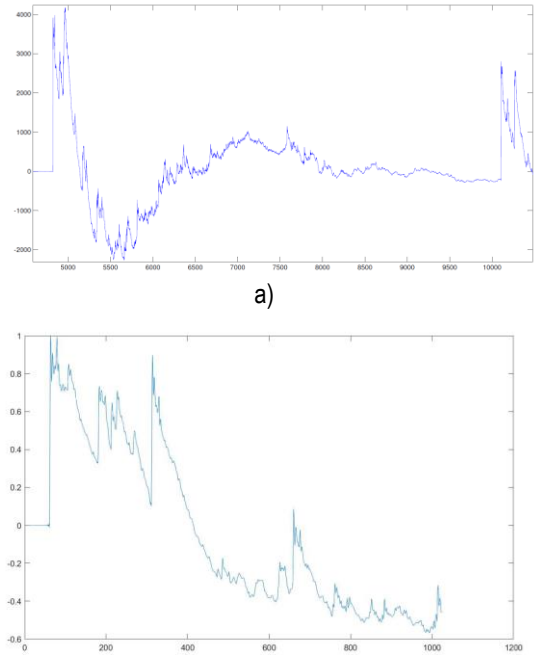

a)

b)

Figure 2. Parts from time signal from the first blast from 122 mm 2S1 howitzer, a) "Salvo", b), the first from two blasts

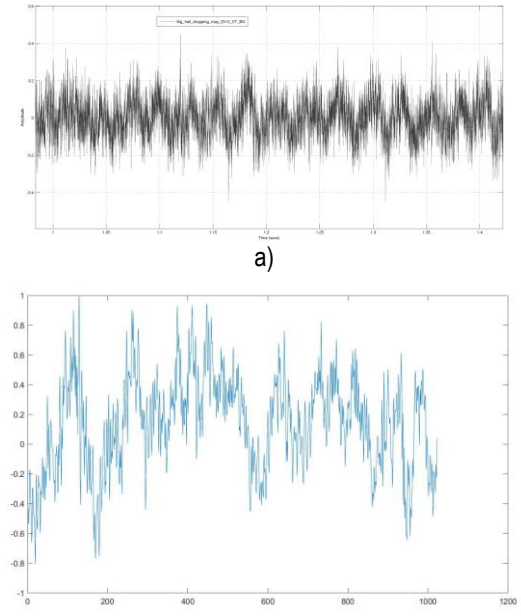

a)

b)

Figure 3. a)-Part of waveform of hail strikes, 0.4sec, in V. Tarnovo, BG, urban environments, 20 May 2013, b) 1024 samples of hail strikes - zoom part of a), Fs=65536 Hz

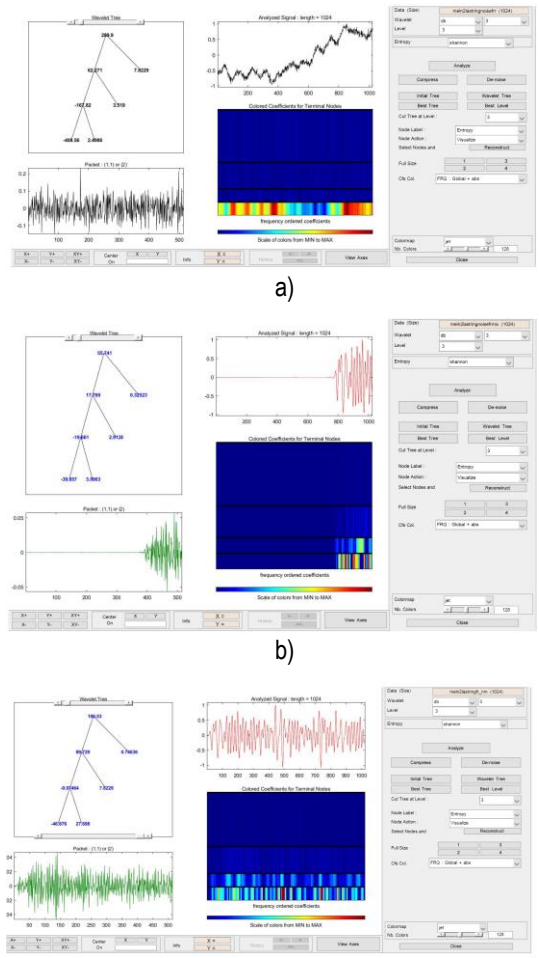

Figure 4. Calculated wavelet packets and Shannon entropies for three cases: a-noise, b-noise and c-ring, see. fig 1 the last ring, (Daubechies db3, level 3).

Table 1

s name (1024 samples)	ShE(0,0)	ShE(1,0)	ShE(1,1)
Noise	289.9	62.271	7.823
Ring_Noise	55.741	17.769	0.32523
Ring	180.53	89.729	0.74636
Uniform distr simulation	220.2	79.51	79.273
Norm distr simulation	141.85	71.464	68.755

Table 2

s name (1024 samples)	ShE(0,0)	ShE(1,0)	ShE(1,1)
Front of blast artil	248.93	119.26	0.77904
Hail2013	186.35	105.22	19.441
Uniform distr simulation	220.2	79.51	79.273
Norm distr simulation	141.85	71.464	68.755

In audio fingerprinting the background noise is one of degradation factors like as pitching, equalization, analog to digital conversion, audio coders etc. When the purpose is automatically recognizing the type of sound recording Papaodysseus [18] and Rousopoulos [19], proposed recognition system of musical recordings in the presence of noise. The main idea in this works is the assumption of existing of invariant characteristics in time – frequency domain, which are independent of distortion and the system employs a set of mathematical characteristics, extracted from a musical recording, whose determination was based on human perception.

In the other side if the purpose is automatically recognizing the type of location from which the signal is received it can be applied data mining methods like it was presented in [20].

5. CONCLUSION AND FUTURE RESEARCH

As it shown proportion of entropy of approximation coefficients to detail coefficients in entropy of discrete signal wavelet packets may be one parameter for noise discrimination.

The obtained results show acceptable accuracy in many real acoustic situations. It was demonstrated that wavelet processing and Shannon entropy was appropriate to analysis the characteristics of acoustic signals.

The future work will be related to their application in aerial acoustics, in interdisciplinary fields such as, study of noise from natural phenomena, ecology, battlefield acoustics and others.

ACKNOWLEDGEMENTS

I would also like to thank prof. Tihomir Trifonov from Vasil Levski National Military University for his advice and for creating an exceptional atmosphere of inspiring interest in acoustic signal processing.

I would also like to extend my thanks to doctor Georgi Dimkov from the Institute of mathematics, Bulgarian academy of sciences for their collaboration in projects and for providing the hardware PULSE.

References

[1] The Bell Project - Research and Identification of Valuable Bells of the Historic and Culture Heritage of Bulgaria and., http://www.math.bas.bg/bells/belleng.html

[2] Fol, V., György, G., Trifonov, T., Alexiev, A., Ivanov I.S., Acoustic Characteristics of Sacral Thracian Sites. AIS

2016 - 11th International Symposium on Applied Informatics and Related Areas, November 17, 2016, Székesfehérvár, Hungary, 84-87.

[3] Trifonov T., I. Simeonov, N. K. Yordanov Advanced Signal Processing Methods For Analysis Of High Dynamic Range Acoustic Phenomena, Proc. 13th Conference on 'Communications, Electromagnetics and Medical Applications' (CEMA'18), Sofia, Bulgaria, 18-20 Oct. 2018, pp. 52-56, ISSN: 1109-1606

[4] Donoho, D. L., Vetterli, M., DeVore, R. A., & Daubechies, I. (1998). Data compression and harmonic analysis. IEEE Transactions on Information Theory, 44(6), 2435-2476

[5] V. M. Tikhomirov, "Widths and entropy," Usp. Mat. Nauk, vol. 38, pp. 91–99, 1983 (in Russian).

[6] Stratonovich R.L. Teoriya informacii [Information Theory]. M.: Sov. radio 1975. (in Russian)

[7] Thomas M. Cover and Joy A. Thomas, Elements of Information Theory. John Wiley & Sons, Second edition, 2006.

[8] Angelova-Slavova, R.L. Convergence and applications of the Metropolis - Hastings Algorithm. Plovdiv: Astarta, 2020. ISBN 978-954-350-284-4 (in Bulgarian)

[9] Angelova-Slavova, R.L. Some Properties of the Kullback – Leibler Divergence. sent to Annual of NVU "V. Levski", to be printed 2020. (in Bulgarian)

[10] Sanchis-Alepuz, H., & Sánchez-Dehesa, J. (2008). Shannon Entropy as a Characterization Tool in Acoustics. Journal of the Acoustical Society of America, 123, 3280.

[11] H. M. de Oliveira and D. F. de Souza, "Wavelet analysis as an information processing technique," 2006 International Telecommunications Symposium, 2006, pp. 7-12, doi: 10.1109/ITS.2006.4433232.

[12] Rizal, A., R. Hidayat, R.,H.A Nugroho, Comparison of multilevel wavelet packet entropy using various entropy measurement for lung sound classification, International Journal of Advanced Computer Science and Applications 10(2), pp. 77-82, 2019.

[13] Rosso, O. A., Blanco, S., Yordanova, J., Kolev, V., Figliola, A., Schürmann, M., & Başar, E. (2001). Wavelet entropy: a new tool for analysis of short duration brain electrical signals. Journal of neuroscience methods, 105(1), 65-75.

[14] Trifonov, Tihomir Fundamentals of sound engineering: [Textbook for VVOVU V. Levski - V. Tarnovo]- Sofia: Ministry of Defence St. George the Victorious, 1995. (in Bulgarian)

[15] Yordanov N., Trifonov T., Simeonov I., An experimental investigation of the 122mm artillery system firing acoustic field, International scientific journal Security&Future, Year I, Iss. 4, Sofia, Dec. 2017, Sofia, Bulgaria, Scientific technical union of mechanical engineering Industry-4.0, pp. 160-162, ISSN: 2535-082X

[16] Ivanov I.S., Hajnal É. Characteristics of Hail Dropping Noise in Urban Environment Journal "Mathematics, Computer Science and Education" Vol. 1, No. 1, 2018, pp. 37–43, "St. Cyril and St. Methodius" University of V. Tarnovo, Bulgaria, ISSN: 2603-4670 (Print)

[17] Trifonov T. Statistika, Faber V. Tarnovo, 2012, ISBN 978-954-9498-18-9 (in Bulgarian)

[18] C. Papaodysseus, G. Roussopoulos, D. Fragoulis, T. Panagopoulos, and C. Alexiou, "A new approach to the automatic recognition of musical recordings," J. Audio Eng. Soc., vol. 49, no. 1/2, pp. 23–35, 2001.

[19] G. Roussopoulos, D. Fragoulis, C. Papaodysseus, Ath. Panagopoulos, M. Exarhos, Mathematical Characteristics for the Automated Recognition of Musical Recordings, WSEAS Transactions on Mathematics, Issue 3, Vol.3, pp. 698-704, July 2004, ISSN: 1109-2769

[20] I. Simeonov, T.Trifonov, T. Georgieva-Trifonova, Signal Processing and Storing of High Dynamic Range Acoustic Data for Knowledge Discovery, Proc. of 14th International Conference on Communications, Electromagnetics and Medical Applications CEMA'19, Sofia, Bulgaria, October 17th-19th, 2019, pp. 58-62, ISSN: 1314-2100.

NONSTANDARD APPLICATIONS OF THE INFRASONIC AND HYDROACOUSTIC COMPONENTS OF THE INTERNATIONAL MONITORING SYSTEM OF NUCLEAR EXPLOSIONS

Tihomir Trifonov

Vasil Levski National Military University, Veliko Tarnovo, Bulgaria
76, Bulgaria Blvd., 5000, Veliko Tarnovo, Bulgaria
Tel. +35962 618724, Fax. +359 62 618899 E-mail: tihomirtrifonov@ieee.org

Abstract

The Comprehensive Nuclear-Test-Ban Treaty, which was ratified by the Republic of Bulgaria in 1999, prohibits nuclear tests in the atmosphere and outer space, underground and underwater. At present, the International Monitoring System collects data from inspections at the International Data Centre located in Vienna, using four modern technologies: seismic, underwater acoustic, infrasonic and radionuclide. This paper discusses the features, methods, equipment and capabilities of the infrasonic and hydroacoustic components of the monitoring system. It has been shown that such systems can be used to detect other phenomena of natural origin or caused by human intervention: volcanic eruptions, hurricanes and typhoons, quarry or mine explosions, firing from large-caliber gun systems, missing submarines and more. Some results of the ***in situ*** *study of the acoustic (sound and infrasound) characteristics of the truck-mounted 122 mm multiple rocket launcher BM-21 "Grad" are investigated.*

1. INTRODUCTION

A nuclear explosion releases a huge amount of energy into the atmosphere. A strong shock wave is formed, behind whose front in the initial period the temperature and pressure are extremely high. As it moves away from the epicentre of the explosion, this shock wave becomes acoustic. This is accompanied by a dissipation of its energy, as the short wave components of its spectrum attenuate faster than the long-wave. Only infrasonic waves remain over long distances, namely those in the ultra-low frequency range (far infrasound), i.e., with frequencies less than 1Hz [1,2,3]. The principle of further propagation of low-frequency components remains in underground and underwater nuclear explosions, where and other types of waves occur. If the nuclear explosions are under water, in the atmosphere above the surface of the world's oceans or underground near the shore, then the sound waves caused by the nuclear explosion can be detected through sonar monitoring stations. Due to the peculiarities of the propagation of sound waves in an aquatic environment (so-called SOFAR), the detection can take place over great distances. It has been proven that this can be done through only 11 stations [1]. They are of two main types: underwater hydrophone stations and so-called T-phase stations [2,7].

However, it should be emphasized that hydroacoustic stations are one of the most expensive and most difficult to maintain. This is because they are located in places with huge hydrostatic pressure, aggressive environment and temperature changes.

In the presented work the peculiarities, methods, equipment and possibilities of the infrasonic and hydroacoustic components of the system for monitoring of air and underground nuclear explosions are considered. It has been shown that these systems, or similar local ones, can be used to detect other phenomena of natural origin or caused by human intervention: volcanic eruptions, hurricanes and typhoons, quarry or mine explosions, firing from large-caliber gun systems and others.

For the first time in 1945, the American scientist Maurice Ewing proposed the use of an ionospheric waveguide channel for acoustic control of possible atomic experiments in the USSR. In the former Soviet Union on the idea of Academician I. K. Kikoin in 1953 created an infrasonic measuring station to detect atmospheric nuclear explosions. In the 1990s, this type of system received a new impetus for development in connection with the Comprehensive Nuclear-Test-Ban Treaty (CTBT).

American scientists Maurice Ewing and J. Worzel discovered the existence of underwater sound channels SOFAR (SOund Fixing And Ranging) transmission in 1944. In the former Soviet Union in 1946, the same discovery was made by L. M. Brekhovskikh and L.D. Rosenberg [6,7].

2. INFRASOUND AND ITS PROPAGATION IN THE ATMOSPHERE

Detection and registration of infrasound waves is a complex task, as the wavelength reaches several kilometers (for example, infrasound with a frequency of 1Hz has a wavelength of 340 meters, and if the frequency is 0.1Hz, the length is already 3.4 kilometers) [4,5]. The sensors used should be protected from noise caused by other factors, such as wind, temperature anomalies, turbulence, etc. Resonant vibrators such as loudspeakers, pipes, strings, etc. could be used as sensors. Their main disadvantage is their large size (hundreds of meters and more) and narrow frequency range. On the other hand, they have high sensitivity and efficiency. At present, compact sensors are most commonly used, which convert acoustic oscillations into electrical signals. They are of two main types: low-frequency condenser microphones [5] (for near infrasound) and microbarometers (for far). This is necessary because the electromotive voltage of the microphones is proportional to the acceleration of the membrane, and in one oscillation for a few seconds or minutes practically no e.v. In the case of microbarometers, on the other hand, they perceive low-frequency infrasound well, while at higher frequencies they are very inert [3].

The ability to detect useful infrasonic signals from the pressure sensors described above is usually determined not by their sensitivity but by the fluctuations in the atmosphere at their location caused by other causes. As an example, the pressure of a typical useful infrasonic signal from a remote source at the point of detection is of the order of 0,1 Pascals, which is equivalent to a barometric pressure caused by a change in height of 1 cm and is not a problem. in the absence of noise to be registered. That is, modern sensor designs provide sufficient sensitivity, but noise filtering is required. At low frequencies, they are caused mainly by changes in weather on a synoptic scale, tides, the effect of sunshine during the day, the breeze circulation in the atmosphere. At higher frequencies they are caused mostly by convection and turbulence.

The energy dissipation of acoustic waves is proportional to the square of their frequency. This means that sound with a frequency of 1000 Hz loses 90% of its energy at a distance of 7 kilometers at sea level, if the frequency is 1 Hz this distance is 3,000 kilometers, and at a frequency of 0,01 Hz it is comparable to the circumference of the globe. (This includes losses from the expansion of the wavefront).

Since the Earth's atmosphere is layered and randomly inhomogeneous, as a result of refraction and other physical phenomena in it, the so-called sound channels in which infrasound propagates over great distances - Fig.1 [2].

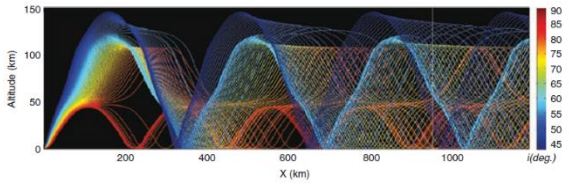

Fig. 1. The propagation of the infrasonic wave (stratosphere and thermosphere)

As emphasized above, in order to detect the useful signal, filtering, spatial and frequency, is required. In spatial filtering, it is important that the correlation radii of the useful signal and the noise are different. The radius of spatial correlation of useful infrasound is much larger. This makes it possible to build spatial filters that average and greatly minimize the energy of noise. Fig.2 shows a picture of a real infrasonic station, in which a similar spider filter is realized [1].

Fig. 2. Acoustic group from infrasound station IS18 in Greenland [1]

The analysis of the function of the cross-correlation or of the mutual spectra between the signals from different noise-protected sensors from one acoustic group or from several groups makes it possible to determine the speed and direction (azimuth) of the source by the signal delays. This analysis can be used in the whole frequency range, and the analysis of the mutual spectra allows to identify signals with different frequencies, but having the same speed and coming from one direction.

A minimum of three infrasonic acoustic groups are required to determine the direction of the source. Typically, an infrasound station contains between 4 and 8 such groups. At present, the International

Monitoring System (IMS) consists of 60 infrasound monitoring stations located around the globe in suitable places (low noise, etc.), [1,2].

Data are collected in quasi-real time in Vienna. An interesting fact is that an electronic signature is used for security of the transmitted information in the stations. Communication links are required to operate with 99.5% availability and its terrestrial communication links with 99.95% availability [1].

2. UNDERWATER SOUND CHANNEL SOFAR. HYDROACOUSTIC DETECTION SUBSYSTEM

The underwater sound channel is formed at a certain profile of the gradient of the speed of sound under water [6,7]. Usually, the axis of the channel is at a depth of about 1 kilometer. On it the sound can travel huge distances almost without attenuation. This is shown in Fig.3.

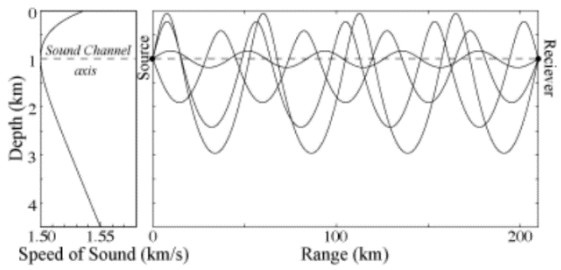

Fig. 3. Example of underwater sound channels SOFAR [6,7]

The hydroacoustic subsystem consists of two types of stations, all 11 in number. They have been shown to cover all important areas of the world's oceans. Six of the 11 stations use low frequency sensitive hydrophones [8] are deployed on the ocean floor, their signals sent by cable to a nearby island for transmission to the International Data Center. For security, two triples of low-frequency hydrophones are located on opposite sides of well-chosen islands.

In addition, five so-called T-phase (from *terrestrial*) seismic stations are deployed on oceanic islands. Hydroacoustic wave travels horizontally from an ocean source, converting to a seismic wave when it meets land. The hydroacoustic and seismic networks are complementary in verification terms: hydroacoustic stations are more sensitive than seismic ones in regard to monitoring the southern oceans, while the reverse is true for the northern oceans [10]. The schematics is shown on Fig.4 and Fig.5 respectively.

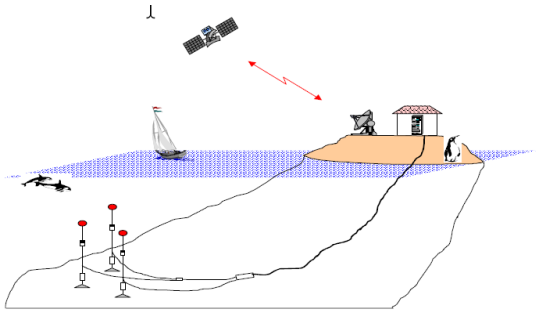

Fig. 4. Hydroacoustic station

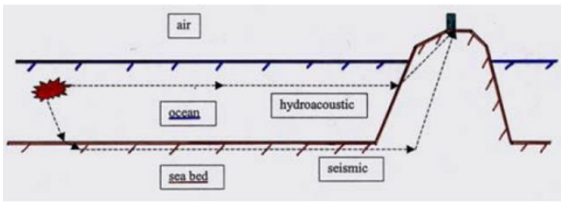

Fig. 5. T-phase station

It should be noted that hydrophone triples are used to applicate triangulation methods in the localization of underwater events [9].

3. SOME EXAMPLES OF APPLICATION OF THE INFRASONIC AND HYDROACOUSTIC METHODS

In addition to their direct purpose (detection of above-ground and underground nuclear explosions), infrasound stations can be used for other useful activities. For the first time, without the necessary equipment, humanity discovered events generating infrasonic waves of enormous power in 1883, the eruption of Krakatoa volcano and in 1909, the fall of the Tunguska meteorite in eastern Siberia. In both cases, infrasonic waves orbit the globe several times and are detected as anomalies in the recordings of ordinary barometers. At present, it is considered that modern infrasonic equipment can be used for the following events of natural and anthropogenic origin (the list is not complete):

- volcanic eruptions;
- occurrence of hurricanes and typhoons;
- quarry or mine explosions;
- rocket launches;
- shock waves when crossing the sound barrier from aircraft;
- falling meteorites;
- infrasound emitted by animals such as elephants;
- shooting from large-caliber gun systems, etc.

Figure 6 shows the spectrum of the noise from the launch of a Scud missile [3]. The distance to the source is 27 km. It can be seen that the event is about 150 seconds from the recording, and the infrasound is from 1Hz to about 25Hz.

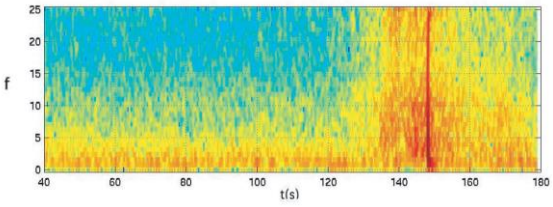

Fig. 6. Launch of an operational tactical missile SS-1 Scud B (8K14 Elbrus). Source: S. Tenney, ARL.

Fig. 7 shows the scalogram of a recording of firing with a rocket-propelled grenade launcher system "BM-21" - flight of 7 122 mm projectiles from a package of volley fire of AP Markovo, Bulgaria, 05 Oct. 2017. It allows for a detailed analysis of the event and to obtain the so-called sound signature of the system.

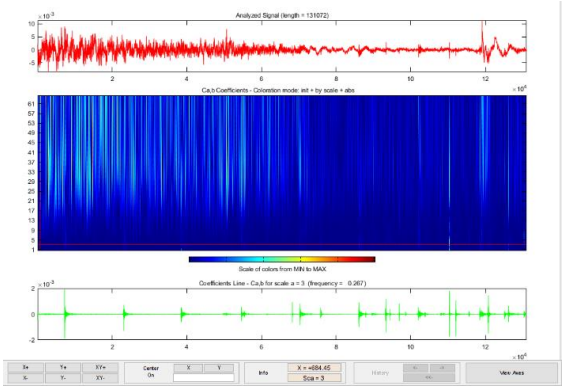

Fig. 7. The scalogram of the recording of firing with a rocket-propelled grenade launcher "BM-21"

The recording was made by the authors with the participation of doctoral students and cadets from Vasil Levski National University, with the integrated PULSE 12 platform of Brüel&Kjær and a low-frequency measuring microphone of the same company [5].

The study of acoustic effects caused by infrasound is a relatively new field, which is an expensive and time-consuming study, which, however, gives very useful results [4].

In Fig. 8 is shown the localization of the crash of the Argentine submarine San Juan. The analysis is performed by specialists from the Center in Vienna [1]. The signal processing is from the north triplet hydroacoustic station H10 in temporary interval from 14:58 to 15:16 on November 15, 2017. The method of progressive multichannel correlation is used. The graph shows the main arrival of the signal at 14:59:07 and subsequent introductions. It can be seen that although the system is designed for other purposes, it must be accurate enough even in non-standard use.

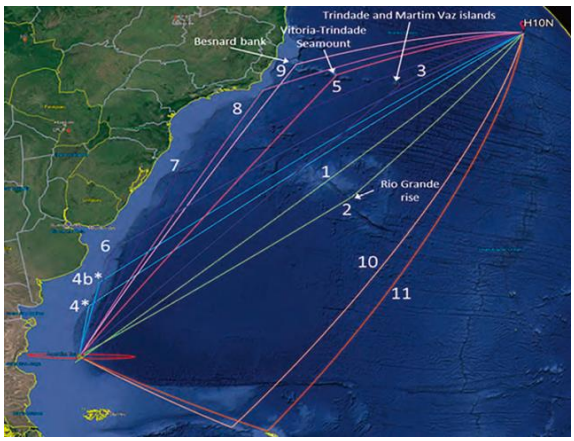

Fig. 8. Localization of the crash of the Argentine submarine San Juan

CONCLUSION

Infrasonic and hydroacoustic monitoring stations, in addition to detecting and locating nuclear experiments in the atmosphere, underground, and underwater, can be used to detect and study other anthropogenic or natural phenomena: volcanic eruptions, the formation of hurricanes and typhoons, quarry or mine explosions, firing from large-caliber gun systems, missile launches, detection of damaged submarines, etc.

The main advantage of this method is that near and far infrasounds propagate over extremely long distances in the air and underwater. Of course, in its implementation there are important features and difficulties, which, however, in the current state of the art are completely surmountable.

In the present work, it is shown by real *in situ* measurements that the method can also be used to collect data on the acoustics of the battlefield, i.e., to monitor tactical infrasound. The created database can be used for civil and military purposes.

References

[1] https://www.ctbto.org/

[2] A. Le Pichon et al. (eds.), Infrasound Monitoring for Atmospheric Studies, DOI 10.1007/978-1-4020-9508-5_3, © Springer Science + Business Media B.V. 2010

[3] Tactical Infrasound, Study Leader: Christopher Stubbs, JASON, The MITRE Corporation, 2005

[4] Ivanov I.S., Hajnal É. Characteristics of Hail Dropping Noise in Urban Environment Journal "Mathematics, Computer Science and Education" Vol. 1, No. 1, 2018, pp. 37–43, "St. Cyril and St. Methodius" University of V. Tarnovo, Bulgaria, ISSN: 2603-4670 (Print)

[5] Brüel&Kjærp,Knowledge-center, https://www.bksv.com/en/Knowledge-center

[6] Clay C S, Medwin H, Acoustical Oceanography,Wiley Interscience, New York, 1977.

[7] Urick R J, Principles of Underwater Sound, 3rd ed. McGraw-Hill, New York, 1983.

[8] Trifonov T., Specific Features of Using Piezoceramic Transducers for Underwater Noise Measurements, Facta Universitatis, Vol.1, No4, 1999, Nis, Yugoslavia, pp.51-55.

[9] Trifonov T., A. Irinchev, Methods for localization of sources of acoustic signals, Scientific notices of NTS in mechanical engineering, Sozopol, 1999, pp.144-149. in bulgarian

[10] Marta Galindo Arranz, A Global Network of Hydroacoustic Stations for Monitoring the Comprehensive Nuclear-Test Treaty, Tehniacustica, Bilbao, 2003

THEORETICAL AND EXPERIMENTAL DETERMINATION OF SOME PARAMETERS OF THE SIGNALS IN DVB-T RECEPTION

Oleg Panagiev

Technical University of Sofia, Bulgaria
Sofia 1000, 8 Kl. Ohridski Blvd.
T. +359 (2) 965 2284; E. ctv@tu-sofia.bg

Abstract

The article discusses some problems with the terrestrial reception of radio and television digital signals (DVB-T) in the single-frequency (SFN) network. The reception is carried out with a Yagi antenna for four channels (23, 27, 40, 49). Mathematical express-ions for basic parameters (BER, MER, and SNR) are proposed and derived, characterizing the quality and reliability of reception of radio and television signals from first-generation digital multiplexes. The constellation diagrams for TV channels are presented at the receiving location from nearby and remote transmitters. The theoretical and experimental results were obtained in the Rice and Relay model of the transmission channel. Presented are graphical, tabular and photo data for four channels of considered digital multiplexes operating in the UHF band with different modulations of subcarriers.

1. INTRODUCTION

Nowadays bigger and bigger part of the radiocommunication systems transmit digital signals: television, radio, data. The project for video broadcasting (DVB) was created in the distant 1993 by representatives of radio and television providers, manufacturers, network operators and regulatory agencies [1]. In the next years several regulatory documents were created by international and European organizations (ITU, ETSI, CENELEC), that were accepted also by national agencies and institutions, where in Bulgaria this is BIS (Bulgarian Institute for Standardization). For the normal functioning of every radiocommunication system, it is necessary for its parameters for broadcasting as well as for receiving signals to correspond to the standardized values. Depending on the environment (air, cable) and place (space, ground) of the distribution of signals, the DVB systems and the corresponding DVB standards are divided in tree types: : DVB-S/S2, DVB-T/T2 and DVB-C/C2 [1, 2, 3, 4].

Over the years, the DVB technology turned into inseparable part of the global broadcast of satellite, cable, ground and IP based services. When a new specification is completed from DVB, it is published as BlueBook, after which the document is usually published as official standard by ETSI [5].

Every DVB system allows for digital signals to be broadcasted or received with MPEG or HEVC compression, where the resolution is SD or HD. The requirements for providing higher and higher quality and reliability of the information lead to constant refinement of DVB systems, improvement of their parameters and application of different methods for processing their signals, protection from failures and control. Since there is a lot common between the three types of DVB systems, it is possible to perform transmodulation from DVB-S/S2 and DVB-T/T2 to DVB-C/C2, which is widely used in the systems for cable television (CATV/HFC).

They are the same for processing the signals in “encoding/decoding the source”, but for “encoding/decoding the channel” they have differences in the type of used modulation and the way of forming of the digital stream before the modulation. In Base Band (BB) the signals are digital, where they are compressed MPEG-2, MPEG-4 or HEVC. After the modulation (QPSK/8-PSK/M-QAM/COFDM) the signal is converted frequency-wise for certain channel, where it is already in analog form [4]. In this sense, the control of the parameters of DVB systems for assurance of their normal functionality is done by measurement of BER, MER, C/N, U_s, V_{bit} and etc., for one or more carrying frequencies in certain frequency range.

The current investigation is done for the determination of these parameters by transmission of digital signals according to the standard DVB-T in single frequency network (SFN). Some problems with aerial reception of digital signals from near and distant multiplexes by Ricean and Rayleigh model of the transfer channel are reviewed.

2. DIGITAL VIDEO BROADCASTING-TERRESTRIAL (DVB-T)

In terrestrial aerial digital television broadcasting (DVB-T) for one channel for the corresponding standard (B/G, D/K), 4-6 digital television channels can be broadcasted. This is achieved through compression of the information for each channel according to the method MPEG-2 or MPEG-4 and forming a transport stream (TS), following multiplexing and modulation. There is only one carrying frequency here, called central f_c. The standard DVB-T provides several work modes, provisionally labeled as 2k and 8k, where the theoretical count of subcarrying signals is 2^{11}=2048 (2k) and 2^{13}=8192 (8k). In practice, however, lower amount of subcarrying signals are used. After addition of the pilot signals, the bits for internal and external protection from failures and synchronization to the useful digital stream (of the video signal, sound signals and the transmitted additional data), the count of subcarrying frequencies reaches up to 1705 (2k) and 6817 (8k). The 2k mode is meant for use in single transmitters and in small single frequency networks (SFN) with small distance between the transmitters. The 8k mode can be used for single transmitters as well as for large single frequency networks with larger distance between the transmitters. Every subcarrying signal is modulated separately with one symbol, where for each cycle of the modulation all subcarrying signals transmit one OFDM symbol. Three ways for modulation of every subcarrying signal are used: QPSK, 16-QAM or 64-QAM. The spectrum of the OFDM signal represents a sum of the spectra of the separate modulated subcarrying signals, which mutually overlap each other. The maximum of certain subcarrying signal matches with the minimums of the spectra of the neighboring modulated subcarrying signals. In fact, the OFDM signal is similar to Gaussian noise. The whole energy of the spectrum is focused in the frame of the television channel with frequency band 8MHz (UHF band), 2k and 8k modes and guard interval Δ′, whose place in OFDM symbol is showed in Fig. 1. In Table1 the values for the main parameters of the OFDM signals are presented and the mathematical dependencies between them are:

$$T_{OFDM} = \Delta + T_u, \text{ [μs]} \quad (1)$$

$$(T_u/T_{OFDM}) = T_u/(\Delta + T_u) = T_u/[T_u/(1+\Delta/T_u)]$$

$$= (1+\Delta/T_u)^{-1} = (1+\Delta)^{-1} \quad (2)$$

$$\Delta' = \Delta/T_u = 1/2^n, \quad (3)$$

where $n = 2, 3, 4, 5$.

$$T_{OFDM}^{(1/4)} > T_{OFDM}^{(1/8)} > T_{OFDM}^{(1/16)} > T_{OFDM}^{(1/32)} \quad (4)$$

$$T_u^{(1/4)} = T_u^{(1/8)} = T_u^{(1/16)} = T_u^{(1/32)} \quad (5)$$

$$\Delta^{(1/4)} > \Delta^{(1/8)} > \Delta^{(1/16)} > \Delta^{(1/32)} \quad (6)$$

$$\Delta^{(1/4)} = 2\Delta^{(1/8)} = 4\Delta^{(1/16)} = 8\Delta^{(1/32)} \quad (7)$$

Table 1. OFDM parameters

Mode		8k			
Δ'		1/4	1/8	1/16	1/32
Δ	μs	224	112	56	28
T_u	μs	896			
T_{OFDM}	μs	1120	1008	952	924
$D=(T_u/T_{OFDM})$		4/5	8/9	16/17	32/33

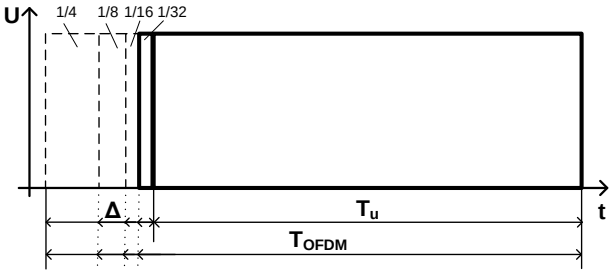

Fig. 1. Guard interval in OFDM symbol

QAM is the most popular modulation for subcarrying signals, where for DVB-T 16-QAM and 64-QAM are used. The output digital signal is formed through with orthogonal frequency division multiplexing (OFDM), respectively with coded orthogonal frequency division multiplexing (COFDM). COFDM is a special form of modulation with many carrying signals, for which one stream of data is transmitted through large number of subcarrying signals with lower data speed. It can deal with the high levels of the multipath distribution and the delays between the received signals. This leads to the concept for single frequency networks (SFN), in which many transmitters send the same signals with the same frequency, generating "artificial multipath". COFDM does similarly well also with co-channel narrowband interference, caused by the existing analog channels [4, 6, 7]. Furthermore, in reality COFDM represents a combination of modulation and multiplexing.

The formed COFDM signal with introduced energy dispersal, outer and inner coding/interleaving, mapping and pilots is converted with D/A converter in a signal with intermediate frequency. After that with UpC, the resulting analog signal is converted for some of the TV channels of the UHF range with width of the frequency band 8MHz. For achievement of certain distance (coverage), the radiofrequency signal (RF) is increased from power amplifier and is passed through a suitable feeder to the antenna (Fig.2a).

The reception of the DVB-T signals is performed with external and internal antenna and is processed in a DVB-T receiver, whose block diagram is shown on Fig.2b. The amplification of the received signals and the choice of precisely defined channel is performed in the tuner, which represents separate screened module integrated in the DVB-T receiver (set-top-box). Here, unfavorable influence is produced by the analog noise and nonlinear distortions. After that, the received signal for a chosen channel is processed by A/D converter and is transformed in digital form. Timing and frequency synchronization are performed in the next block and the guard interval in front of every symbol is removed and the symbol is processed by FFT for demodulation of OFDM [8].

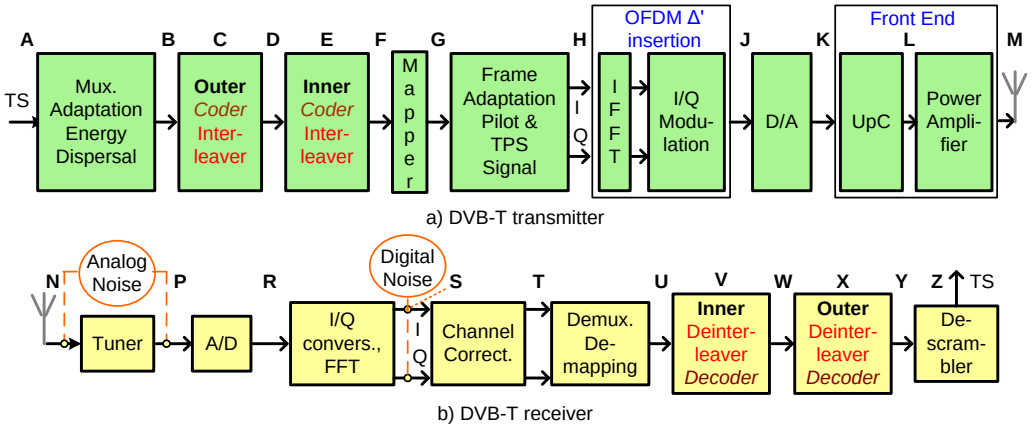

Fig. 2. Block diagrams of a DVB-T transmitter and receiver

The obtained I and Q components of the signal are subject to subsequent processing: channel correction, demulti-plexing and demapping, inner and outer deinterleaving/decoding, and descrambling (option). After that the decoded/ descrambled data is sent to the MPEG decoder. Here unfavorable influence is produced by the digital noise and Inter Symbol Interference (ISI). The protection from failures is done by Viterbi decoder and by RS decoder.

In real SFN network, the reception of DVB-T signals is of several transmitters working on one frequency (Fig.3). Through optimization of the density of the transmitters, the height and the location of the tower, the power of transmission, SFN can provide better coverage and economy of the spectrum. In addition, a satisfactory level of interference to and from adjacent networks can be maintained. However, the existence of at least two transmitters, even synchronized with GPS, makes the reception harder due to "natural" echoes conditioned by the lay, the buildings, the presence of trees, chimneys and etc. between the transmitter and the receiver.

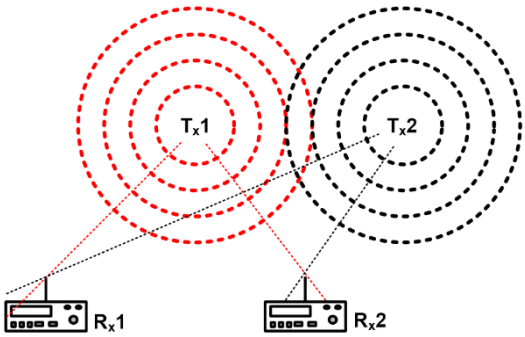

Fig. 3. SFN configuration

For a good reception, it is important that the echo arrives at the reception point within the protection interval, which is favorable, and at the places located at the edge of the coverage zone, a lower power will be needed. The signals coming from the transmitter will contribute to improvement of the common ration between the carrying signal and noise. The zones in radio shadow can be serviced also by secondary amplification, where "gap- filler" is used, representing a co-channel retransmitter.

During the installation and set up of every DVB-T transmitter, it is necessary to set up also the delay of

the signal, so that, at all places for reception in the coverage zone, the relative delays of all significant received signals (the main ones and their echoes) can be in the range of the guard interval. R_x1 receives the main signal from a transmitter T_x1 and the delayed and attenuated signal from T_x2. R_x2 receives the signals from T_x1 and T_x2 without differential delay [9].

The establishment of the level of influence of unfavorable factors on the DVB-T signal parameters and respectively decrease in the quality and reliability of the connection transmitted in the channel and subsequently received information, is done according to numerous regulatory documents. In these documents, the methods and means for experimental definition of the necessary values for BER, MER, S/N, END, EVM, C/N and etc. are presented. In [4] are presented "DVB-T measurement parameters and their applicability" for transmitter, network and receiver. The following parameters, which give an in-depth analysis of the various impacts (all deteriorating the signal), can be calculated [4, 6]:

a) Modulation Error Ratio (MER) - S, T and H test points:

$$MER = 10.lg\left\{\frac{\sum_{j=1}^{N}(I_j^2 + Q_j^2)}{\sum_{j=1}^{N}(\delta I_j^2 + \delta Q_j^2)}\right\}, \text{[dB]} \quad (8)$$

where I_j and Q_j are the ideal coordinates of the j^{th} symbol, δI_j and δQ_j are the errors in the received j^{th} symbol point and N is the number of symbols in the measurement sample.

b) Signal-to-Noise Ratio (SNR or S/N) – S, T test points:

$$SNR = 10.lg\left\{\frac{\frac{1}{N}\sum_{j=1}^{N}(I_j^2 + Q_j^2)}{\frac{1}{N}\sum_{j=1}^{N}(\sigma I_j^2 + \sigma Q_j^2)}\right\}, \text{[dB]} \quad (9)$$

where the σI_j and σQ_j are the error vector co-ordinates which represent the offset from the co-ordinates of the centre (mean value) of the actual received data for a specific constellation point, to the actual received data point j.

c) Bit Error Rate (BER) – from F to U or from E to V; W or X; Z. BER is the numerical value of Error probability P_B. From [4] and [6] the mathematical dependence is derived for Error probability:

$$P_B = A.erfc\left[\sqrt{C.(E_b/N_0)}\right].\left\{1 - B.erfc\left[\sqrt{C.(E_b/N_0)}\right]\right\}, \quad (10)$$

where for 16-QAM A=0,75; B=0,38; C=0,4 and for 64-QAM A=0,88; B=0,44; C=0,14.

3. THEORETICAL AND EXPERIMENTAL RESULTS

The reception of DVB-T signals is carried out with antenna from "wave channel" (Yagi) type, oriented in the horizontal and the vertical plane (in external and internal installation). The measurements were made with a specialized measuring instrument that allows to monitor and record the parameters and characteristics of the received first generation digital multiplex TV signals. The location of reception is the city of Sofia, where channel 23, 27 and 40 are from closely and channel 49 from far away placed transmitters. The theoretical and experimental results were obtained by two models of the transmission channel:

- Ricean = directional receiving antenna + reflected signals;
- Rayleigh = omnidirectional antenna reception + reflected signals.

In Table 2, the main parameters of the signals transmitted in every of the above-mentioned channels are mentioned as well as the calculated speeds of the digital streams in Mbps. For the goal according to [10], equation (2) and Table 1 the mathematical dependencies for net data rate V_{bit} are derived:

$$V_{bit} = SR\,.\,b\,.\,R_c\,.\,K_{RS}.\,(1+\Delta')^{-1}$$

$$= SR\,.\,b\,.\,R_c\,.\,K_{RS}/(1+\Delta'), \text{[Mbps]}, \quad (11)$$

where $b=log_2M$, K_{RS} =188/204 and

$$(T_u/T_{OFDM}) = D = (1+\Delta')^{-1}. \quad (12)$$

Then

$$V_{bit} = SR\,.\,b\,.\,R_c\,.\,K_{RS}.D \text{ , [Mbps]}. \quad (13)$$

On Fig. 4 is shown the graphical relation-ship of V_{bit} = func (channel, Δ'). The carrying frequencies of every channel are calculated according to the following formula:

$$f_{c,i+21} = 474 + i.B \text{ , [MHz]} \quad (14)$$

where $i = 0, 1, 2, 3, \ldots, 48$ and B is channel bandwidth.

Table 2. Parameters of the channels

Parameters \ channel	23	27	40	49
f_c MHz	490	522	626	698
Modulation	64-QAM	16-QAM	64-QAM	64-QAM
B MHz	8	8	8	8
Mode	8k	8k	8k	8k
R_c	2/3	2/3	2/3	2/3
b	6	4	6	6
Δ'	1/4	1/16	1/4	1/4
V_{bit} Mbps	20,27	15,90	20,27	20,27

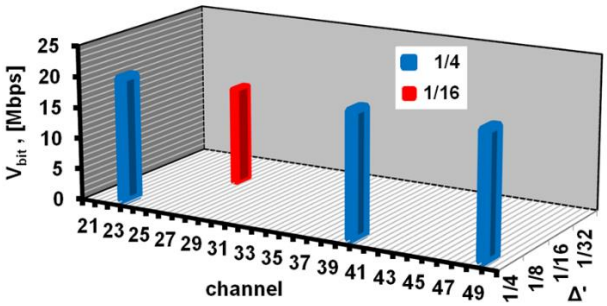

Fig. 4. V_{bit}=func (channel, Δ')

The numerical values of the main parameters of the DVB-T signals for the four television signals are presented in Table 3 and the graphical relations between them on Fig.5 *BER=func(C/N)*, Fig.6 *C/N and MER=func(f_c)* and Fig.7 U_s=*func*(f_c). For MER, C/N and U_s of the presented graphics, a comparison was made between the obtained values for Rayleigh and Ricean channels and those required by the standard [10] C/N_{min} and $U_{s\,min}$ - the lowest (Low) and highest (High) values of 5 referenced.

Table 3. Experimental results

Parameters \ channel	23		27		40		49	
Model channel	Ricean	Rayleigh	Ricean	Rayleigh	Ricean	Rayleigh	Ricean	Rayleigh
C/N dB	31,8	12,5	25,6	4	32,2	10,7	8,4	0,1
MER dB	25,7	15,8	21,7	11,9	24,5	16	17	-
CBER	4,8E-3	7,1E-2	5,1E-3	6,8E-2	4,5E-3	6,3E-2	5,8E-2	-
VBER	<1E-7	6,5E-5	<1E-7	4,5E-3	<1E-7	7,9E-5	2,8E-5	-
U_s dBμV	57,2	37,9	51	28,7	58,3	35,9	35	26,5

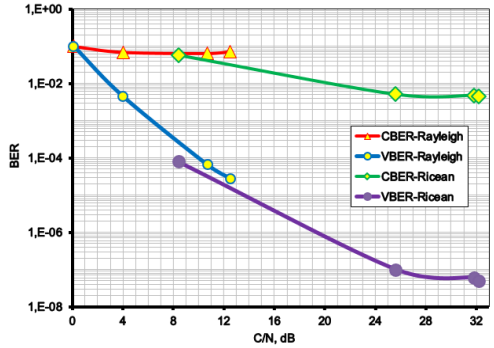

Fig. 5. BER=func (C/N)

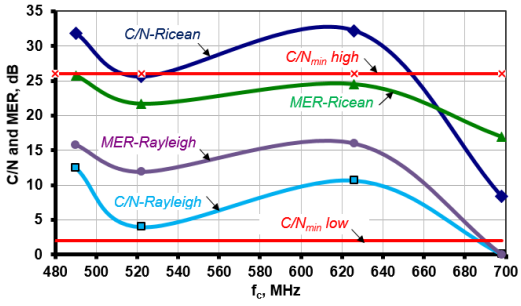

Fig. 6. C/N and MER=func (f_c)

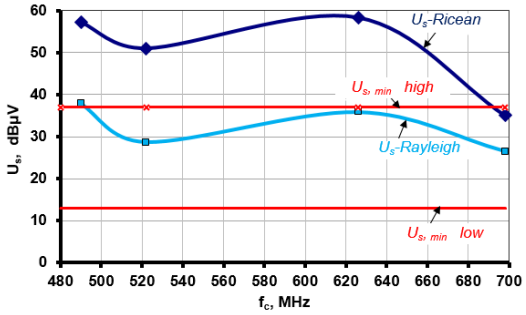

Fig. 7. U_s=func (f_c)

The deterioration of BER is more significant on the Rayleigh channel than on Ricean channel, because of the presence of disturbances by interference from echoes or from the signals from adjacent transmitters. For the distant transmitter (ch.49) even the level of the signal is <26,5 dBμV and an image of the constellations is missing (Fig.8), while for the closer one (ch.40) VBER=7,9E-5 and the level is 35,9 dBμV (Fig. 9).

Fig. 8. Constellation and spectral diagrams (ch.49-Rayleigh)

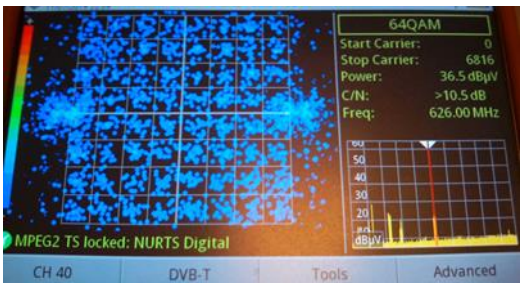

Fig. 9. Constellation and spectral diagrams (ch.40-Rayleigh)

For Ricean channel: for ch.49 the level of the signal is with around 10 dB higher compared to the Rayleigh channel, and VBER=2,8E-5 has an image of the constellations (Fig.10). For the near (ch.40) VBER<1E-7 and the level is 58,3 dBμV (Fig. 11).

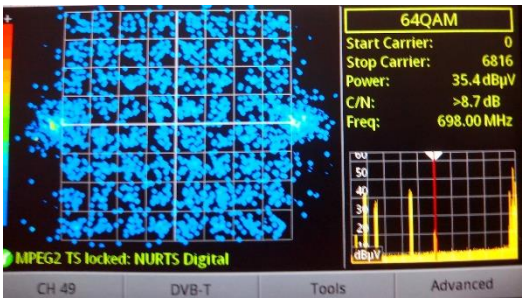

Fig. 10. Constellation and spectral diagrams (ch.49-Ricean)

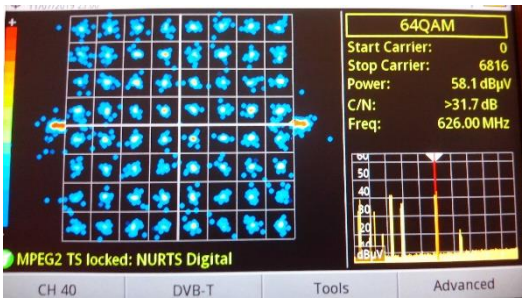

Fig. 11. Constellation and spectral diagrams (ch.40-Ricean)

4. CONCLUSION

The obtained theoretical and experimental results allow the formulation of measures to improve the DVB-T service at the receiving point. These measures can be divided into two: measures, that are undertaken by the operator-owner of the multiplexers and measures to be taken by the customer. In the first case, the measures are related to the broadcasting and retranslation of the signals, and in the second case, to their reception. Here are some of them:

a) Measures for transmission:

- changing the length of the protection interval, which, if Δ′ is extended without change in the absolute duration of T_u, would accordingly reduce the capacity of the channel and V_{bit} (a longer Δ′ could compensate longer echoes);
- extension of Δ′ and T_u, which wouldn't lead to decrease in the capacity of the channel, but would make the processing of the signal difficult;
- in irregularly spaced networks the self-interference can be minimized by specific distribution of given transmitters over time.
- when there is a lack of coverage in the zone of service (deep valleys, tunnels, underground places or inside houses), a "gap-filler" can be used.

b) Measures for reception:

- finding a better spot for the antenna;
- usage of one or more directional antennas with higher gain;
- usage of antenna amplifier with low noise in case of reception with stationary antenna.

In SFN usually 8k mode is used (Table1), because the symbols and therefore the respective protective intervals are longer. The big SFN use the maximum Δ′=1/4 to support greater distances. For smaller regional SFN and for filling a gap, smaller Δ′ can be used.

For the observation and control of some main parameters of the DVB-T signals on the customer side, some manufacturers allow for those parameters to be visualized on the screen of the TV through suitable software (Fig.12). This software is installed in the set-top-boxes (STB) [11] during their manufacturing or at later stage trough "Update".

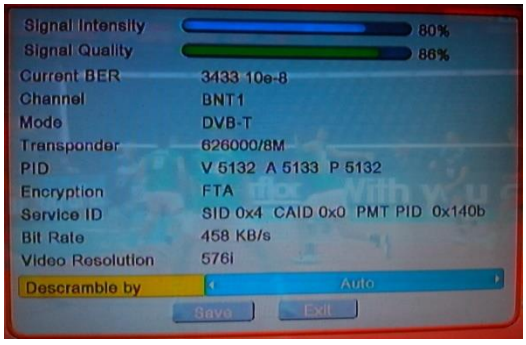

Fig. 12. DVB-T parameters from STB

References

[1] ETSI EN 300 744:"Digital Video Broadcasting (DVB); Framing structure, channel coding and modulation for digital terrestrial television", 2015

[2] EN 300 421:"Digital Video Broadcasting (DVB); DVB framing structure, channel coding and modulation for 11/12 GHz satellite services", 1997

[3] EN 300 429:"Digital Video Broadcasting (DVB); DVB framing structure, channel coding and modulation for cable systems", 1998ETSI

[4] TR 101 290:"Digital Video Broadcasting (DVB); Measurement guidelines for DVB systems", 2014

[5] DVB Standards, 2019, www.dvb.org

[6] Panagiev, O. B. Improving the reception of class DVB-T receivers. ICEST, Proc. of Papers, vol.1, V.Tarnovo, June 2012, pp.13-16

[7] J.H. Stott, The how and why of COFDM, EBU Technical Review, 1999

[8] Sadinov S. , P. Daneva and P. Kogias, Description and Simulation of OFDM Reception Process, Journal of engineering science and technology review, Kavala, Greece, Vol.7, Issue 3, 2014, pp. 18-22

[9] DVB-T/H Field Measurements, App. Note, 2010, www.anritsu.com

[10] TR101190:"Digital Video Broadcasting (DVB); Implementation guidelines for DVB ter-restrial services; Transmission aspects", 2011

[11] http://ferguson-digital.eu/en/download/

EXPERIMENTAL SETUP FOR CONTROL, REGULATION AND SET UP OF OSCILLATOR FREQUENCIES IN LNB CONVERTERS

Oleg Panagiev

Technical University of Sofia, Bulgaria
Sofia 1000, 8 Kl. Ohridski Blvd.
T. +359 (2) 965 2284; E. ctv@tu-sofia.bg

Abstract

The article discusses problems arising in the low noise block (LNB) satellite communications converters and their solution. An experimental setup for establishing the oscillator frequency according to the standard values specific to the different types of LNB converters: Singleband, Dualpol, Universal (Single, Twin, Quad, Quattro) is proposed. The experiments were applied for control, regulation and set up of the frequencies of the local oscillators for the low (9750MHz) and high (10600MHz) Ku band range but they can be equally applied to other types of LNBs operating in different frequency ranges. In the experimental setup, no additional generators, emitters, polarizers and feedhorns are used, but only a level meter with a built-in spectrum analyzer with a working frequency band up to 2150MHz. As a source of radio signals for a specific range and polarization, transponders from satellites located on geostationary orbit are used.

1. INTRODUCTION

The reception of satellite signals (TV, R, Internet) is performed with individual and collective (SMATV, CATV) systems. Two satellite ranges are mainly used:

- C (3,4-4,2)GHz;
- Ku (10,7-12,75)GHz.

In recent times the Ka band (17,2-22,2) GHz also finds wider application in VSAT systems. Due to the high values of the radiofrequencies (RF) f_{sig} and their high decay in the coaxial transferring media, it is necessary for frequency of the signals from the satellites to be converted to a lower frequency range and then to be transmitted through a coaxial cable to the receiving equipment (set-top-box, TV receiver, Head End, etc.). The devices, that are used for this purpose are mounted in the focus of the satellite antenna (Dish-parabolic, offset) and are called Low noise block converter (LNB) or Low noise converter (LNC). In some literature sources [1, 2, 3] the name Low noise block downconverter (LNB, LND) is also used. Its main purpose is to amplify the received signals and to convert their frequencies to a lower frequency range IF1=(950-2150) MHz. The frequency converter (DwC) is essential part of LNB and consists of local oscillator and mixer to whose output the filter is connected to.

During normal use of LNB due to different reasons, changes in their technical parameters or defects occur, which make its functioning impossible. Most characteristic are:

- causing defects in the semiconductor elements (transistors, diodes, integrated circuits), resistors and conductors due to penetration of moisture and water, as well as static electricity;
- change in the location of the dielectric resonators, caused by peeling off of the PCB;
- blockage of the waveguides with nests of invading insects (most often wasps) through a pierced plastic cap of the feedhorn (Fig.1).

Figure 1. Plastic cap of the feedhorn

A number of these defects can be removed, but this requires LNB to be disassembled and the defective elements to be replaced. In any such case the oscillator frequency f_{osc} is changed in narrower or wider borders like ±2MHz, ±7MHz, ±10MHz and even

more than ±30 MHz. After disassembly of LNB and removal of the defect, assembly follows, but to the extent that adjustment of f_{osc} is possible.

2. STRUCTURAL DIAGRAMS OF LNB

The every LNB contains single-step, double-step or triple-step Low Noise Amplifier (LNA), local oscillator, mixer, integral stabilizer (most often 78xx) and filters.

In the more complex/multifunctional LNBs (Twin, Quad, …) are also electrical switches/multiplexers integrated for provision of same signals in every output (Fig. 2).

The other type of LNB (Quattro), which is used in the collective systems [4] is with four outputs, where the manufacturer decides the arrangement of the signals by polarization and subband (Table 1).

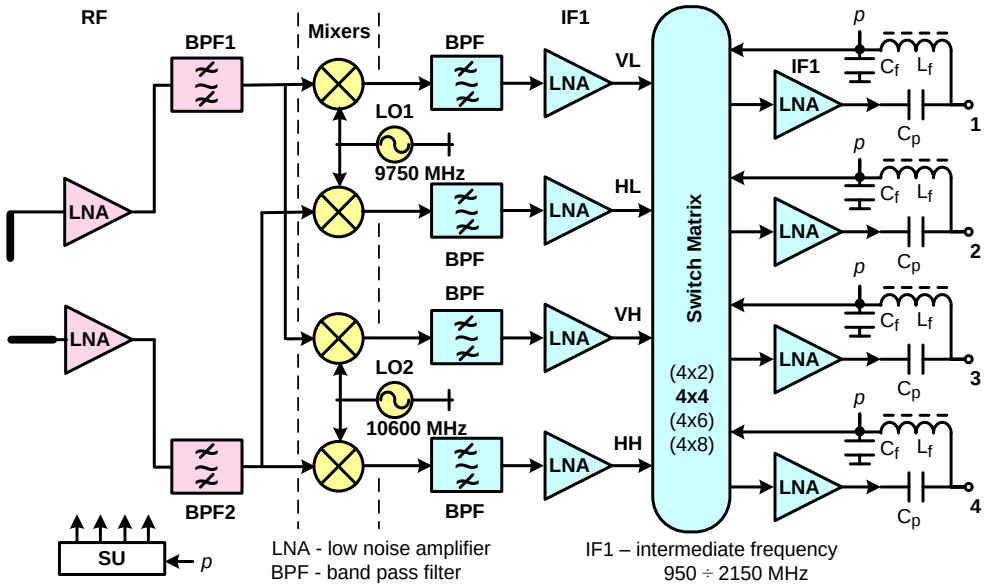

Figure 2. Block diagram Quad LNB

Table 1. Pins for Quattro LNB

Band	Sub band	Polarization	
		Horizontal	Vertical
Ku	Low	HL	VL
	High	HH	VH

The active and passive electronic elements (transistors, resistors, capacitors, inductances, etc.) for processing of the signals from every subband are mainly on separate printed circuit boards (PCB), but there are also such that exist on one PCB.

Regardless of the type of LNB, the oscillators are realized with bipolar or field transistors with parallel or series feedback, that are most often connected according to common emitter/sours scheme [5, 6], where their transit frequency must satisfy the condition:

$$f_T > 2f_{osc}, \text{[GHz]}. \quad (1)$$

The frequency of the output signal IF1 in the modern universal LNB is from 950MHz to 2150MHz and is derived from the following equation [7]:

$$IF1 = f_{sig} - f_{osc}, \text{[MHz]} \quad (2)$$

where for the low subband IF1 = (950-1950) MHz and for the high subband IF1 = (1100-2150) MHz.

For LNB, that work under 8GHz, i.e. in C range [7]:

$$IF1 = f_{osc} - f_{sig}, \text{[MHz]}. \quad (3)$$

The oscillator frequencies are standardized for:

a) Ku band:

- Singleband and Dualpol LNB, f_{osc} = 10 000 MHz;
- Universal LNB, $f_{osc,\ Low}$ = 9 750 MHz and $f_{osc,\ High}$ = 10 600 MHz;

b) C band:

- Singleband and Dualpol LNB, f_{osc}=5150 MHz.

Note 1: There are also other values of the oscillator frequencies, but they are used less often. In some satellite receivers there is a possibility for input of arbitrary values of f_{osc}, (Fig. 3).

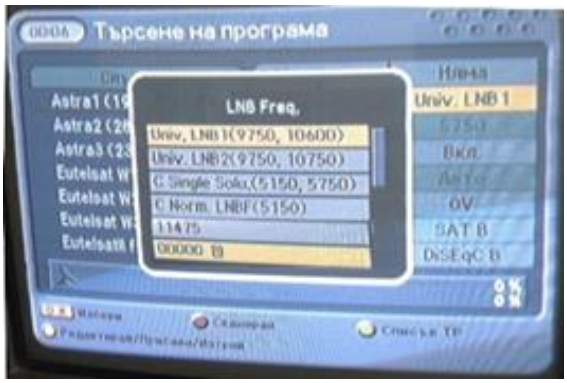

Figure 3. Menu of DVB-S set-top-box

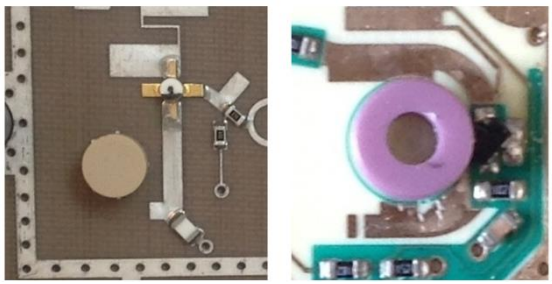

Figure 4. Dielectric resonator (DR)

The main frequency setting element in the classical oscillators is the dielectric resonator (DR), (Fig. 4). Its resonance frequency in the general case according to the equations of Maxwell in TE_{mnp} mode is defined according to the formula [1, 8, 9]:

$$f_r(TE_{mnp}) = \frac{c}{2\pi\sqrt{\mu_r\varepsilon_r}}\sqrt{(\frac{X'_{mn}}{r})^2 + (\frac{p\pi}{h})^2}, \quad (4)$$

where

c = 3.10^8 m/s;

m, n, p – the number of variations in the standing wave pattern in the x, y, z directions;

x'_{mn} – extrema of Bessel functions of first kind;

r – radius DR;

h – height DR;

ε_r – the DR's material dielectric constant;

μ_r – the DR's material magnetic constant, $\mu_r = 1$.

The oscillators in LNB work on TE_{011}. After the corresponding conversions and observing the border conditions for the oscillator frequency with precision of 2%, the following formula is derived:

$$f_{osc} = 374.\frac{r^2}{\sqrt{\varepsilon_r}}.(\frac{2,7}{\pi^2} + \frac{h}{r}).\frac{1}{V}, \quad (5)$$

where

$30 < \varepsilon_r < 50$ and $2 > (h/r) > 0,5$;

$V = \pi.r^2.h$ – volume of the resonator.

With lower acceptable precision (5-10%), equation (5) can be written as:

$$f_{osc} = 73.\frac{\pi}{\sqrt{\varepsilon_r}}.\frac{1}{\sqrt[3]{V}}. \quad (6)$$

Note 2: By *r* and *h* in [mm] f_{osc} is in [GHz] and by *r* and *h* in [m] f_{osc} is in [MHz].

In practice, the precise ascertainment of the oscillator frequency is done by changing the volume of DR (most often with change of its height) through a metallic screw mounted on the metal screen around the oscillator (Fig. 5).

Figure 5. LNB inside (high subband)

3. EXPERIMENTAL SETUP AND RESULTS

3.1. Description of the experimental setup

The experiments were performed according to the scheme of the experimental setup (Fig. 6) with Universal Quattro LNB, in which the processing of the signals for every subband is done on separate PCB (Fig. 5 High and Fig. 7 Low). The satellite signal from the antenna with LNB separates in two through a splitter, where a combined measuring device (level meter with integrated spectral analyzer) with maximal work frequency of 2150 MHz is connected to one of its outputs, while to the other – a satellite receiver (DVB-S/S2 set-top-box). On the screen of television receiver (TV) are illustrated the menu, submenus and the image of the received channels from the satellite using the satellite receiver.

Figure 7. LNB inside (Low subband)

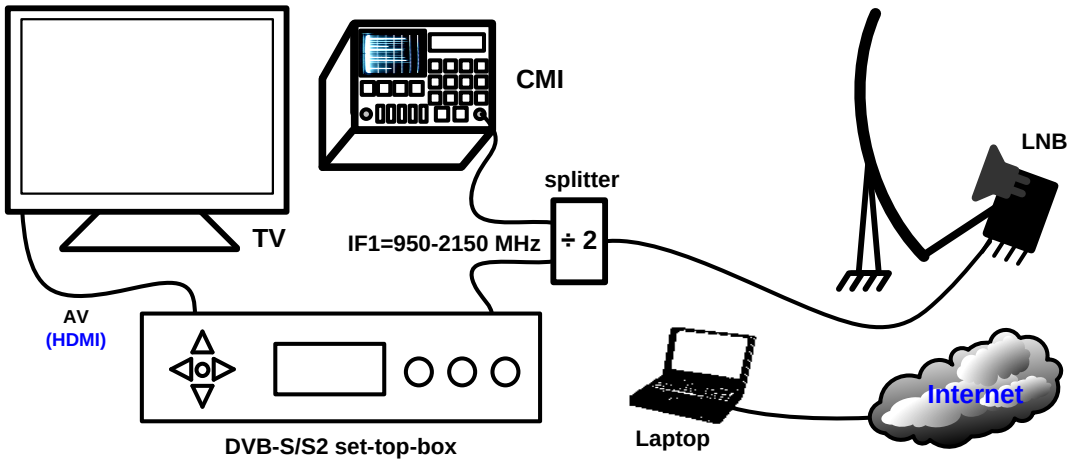

Figure 6. Experimental setup

The connection between TV and set-top-box is through AV cable or HDMI cable. Before starting of the essential part of the experiment, it is necessary for the parameters of the transponders from the satellite, to which the antenna is preconfigured, to be inputted in the set-top-box. For this goal information from www.lyngsat.com is used.

At the beginning (first stage) LNB is with the original settings of the oscillator frequencies and the measured values are presented in Table 2. After that (second stage) it is disassembled and then again assembled. New measurements are performed and the data is filled again in Table 2. In the third stage LNB is again disassembled, but with ungluing/gluing of the dielectric resonator and desoldering/ soldering of the oscillator transistor. The results are given in Table 2.

Table 2. f_{osc} for LNB

	f_{osc}, MHz	
standard	9750	10600
original	9752	10603
new	9750	10600

Note 3: The whole experiment is performed in one day under the same weather conditions for the same transponders in Low and High subbands for the two polarizations (H and V).

3.2. ALGORITHM FOR SET UP

According to the scheme of the experimental setup, when the experiment is carried out (the three stages) it is necessary to perform the following algorithm for the correct set up of the f_{osc} (Fig. 8):

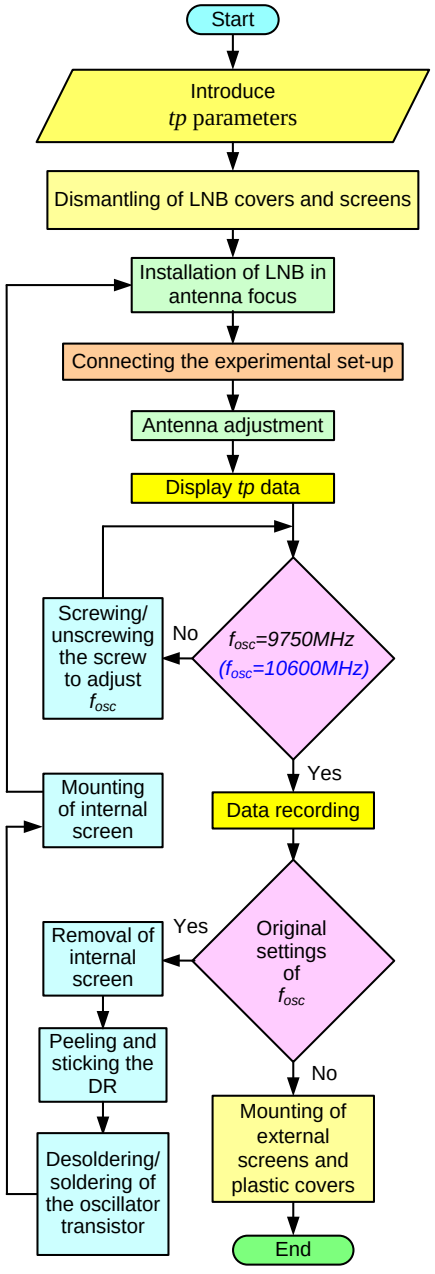

Figure 8. Algorithm

1) Disassembly of the plastic caps and metal screens, in order to reach the screws for adjusting the height and volume of the DR and respectively of f_{osc} for every subband.

2) Mounting of LNB in the focus of the antenna.

3) Connection of the experimental setup from Fig. 6.

4) Orienting the antenna to preselected satellite. For its precise setup (by azimuth and elevation), the measurements of the combined measurement device in spectral analyser mode and the TV, where the main parameters of the satellite signals are visualized, are watched (Fig. 9). After the appearance on the TV screen of the maximal values of the level and quality of the signal for a specific transponder, all screws and nuts are tightened.

Note 4: The transponders for the specific satellite are chosen in advance and the data for the frequency, polarization, speed of symbols (SR) and f_{osc} are entered. Supply voltage to the LNB is permitted.

5) The data is read and written in Table 2.

6) The screen for Low and High subbands are successively disassembled. In the third state, the DR is peeled/glued, and the oscillator transistor is desoldered/soldered. These operations require the disassembly and, again, assembly of the LNB from and to the holder of the focus of the antenna. After the procedures in the second and third stages, the screens with the screws for the regulations of the oscillator frequencies are mounted.

7) Power is provided to the LNB, according to the experimental setup, successively for every output (respectively polarization and subband).

Note 5: In the same way are the checks and adjustment of f_{osc} performed for the other subbands and polarizations.

8) LNB is demounted from the antenna, the external screens and plastic caps are mounted.

9) LNB is mounted in the focus of the antenna again and verification of the values of f_{osc} for each subband is performed.

Note 6: If necessary, the operations from 1 to 9 are repeated (the author in his practical activity has not had so far such problem).

3.3. Experimental results

From the measured data (Table 2), it can be seen, that for Low the oscillator frequency has changed with around 2 MHz and for High – with around 3 MHz. The placement of the screw for regulation of the height of the DR is presented on Fig. 7: 1- initial position at original setting and 2- new (after the set up).

On Fig. 9 and Fig. 10 shows the spectrograms and bargraphs respectively at $f_{osc} \neq 9750$ MHz and after tuning with the screw $f_{osc} = 9750$ MHz.

Figure 9. $f_{osc} \neq 9750$ MHz

Figure 10. $f_{osc} = 9750$ MHz

It is clear that at f_{osc} different from the standard values there may be an indication of the presence of a satellite signal, but the quality is low, which is due to the high BER values before and after the error correction due to the low values of C/N < 6,5 dB [10].

After application of the described method for precise set up of the oscillator frequency, the quality of the channel rises from 16% to 69%-73%, which allows proper reproduction of the satellite signal and the appearance of quality image (Fig.10) and sound.

4. CONCLUSION

The suggested method and the described algorithm can be applied to all types of LNB converters, whose oscillator frequencies are obtained with DR oscillator (DRO). In this paper, the case where both oscillator frequencies are higher than the standard was investigated. They can be applied with the same success also when one f_{osc} is lower (e.g. 10597MHz), and the

other is higher (e.g. 9764MHz) or both f_{osc} are lower (e.g. 9743MHz and 10540MHz). After disassembly and subsequent assembly of LNB, it is necessary to pressurize its housing for protection from penetration of water, moisture and dust.

References

[1] Pozar, D., Microwave engineering, 4th ed., 2012

[2] Ku-band LNB line-up, http://www.pabr.org, 2018

[3] Wade, P., D. Twombly, Modification of TVRO LNBs for 10GHz, QEX magazine, p.3-5, April 1995

[4] Sadinov. S., P. Kogias, K. Angelov, Determination of Distortion in Broadband Amplifiers for Different Standards of Signals in CATV Networks, ARPN Journal of Engineering and Applied Sciences, Vol.11, No.17, 2016

[5] Abdullah, M., M. Atif, G. Anton, J. Fang, Design guide for RF transistors and diode in low noise block (LNB), App. Note Infineon, 2018

[6] AN11698: BFU910F FE for Ku band Universal Single LNB applications, App. Note NXP Semiconductors, 2015

[7] Panagiev, O. Handbook for Laboratory Exercises in Radiocommunication Systems, Technical University of Sofia, 2019

[8] Kajfez, D., P. Guillon, eds. Dielectric Resonators, 2nd ed., Noble, 1998

[9] Huitema, L., T. Monediere, Dielectric Materials for Compact Dielectric Resonator Antenna Applications, Chapter 2, Intech, 2012

[10] www.lyngsat.com

MODELS OF DIFFUSION PROCESSES ON TRIANGULATED SURFACES

N. Ampilova, G. Doronin

St. Petersburg State University
n.ampilova@spbu.ru

Abstract

Diffusion processes occur in many scientific areas, they are especially important in chemistry, biology and medicine. The most part of mathematical models for a description of diffusion are nonlinear Partial Differential Equations which do not have analytical solutions, and numerical methods require large computing resources. As scientific interest to the structures (fractal clusters) generated in the result of diffusion processes grows, the search of new models is intensified. The important method complementary to mathematical models is imitation modeling in which space mobility of the particles of a substance is directly modeled.

There are two directions in such an approach: an imitation of random walks of particles and cellular automata modeling. In this work we implement based on random walk algorithms for the modeling of the growth of fractal clusters on triangulated surfaces. We use classical variants of Diffusion Limited Aggregation (DLA) and Reaction Limited Aggregation (RLA) models. It is shown that for Cluster Aggregation (CCA) model fractal cluster cannot be constructed correctly without additional assumptions about the cluster restructuring. The software is implemented on Python language and may be used by both researchers and students as a tool for modeling complex processes.

1. INTRODUCTION

Diffusion is one of main processes when two substance interact. Hence the mathematical and imitation modelling are common tool for research. Mathematical models are often do not have analytical solutions and we need to apply numerical methods. In additional to these methods one may use imitation modelling in which a mobility of particles is modelled directly. Such an approach allows obtaining visual representation of the objects which appear in the result of diffusion both on surfaces and in the space. Complex structures generated by various diffusion processes are called aggregates or fractal clusters due to their similarity with well-known objects. Really, aggregates may be not only fractals but multifractals as well.

The active studying of such structures began in 1970 and continues successfully up to now. Imitation modelling of the growth of fractal clusters in an environment having given physical properties may help in the forecasting the process under study. Fractal aggregates appear in the process of crystallization [8], and hemagglutination [14]. Imitation modelling was applied to the study of the spread of cancer cells in blood [16].

The models of the construction of fractal clusters may be divided into following groups [13]:

- by a method of cluster formation (cluster-particle or cluster-cluster)
- by a method of the motion of particles or clusters (chaotic or directional)
- by a method of sticking of particles or clusters depending on a coefficient.

In 1981 W. Witten and L. Sander proposed the first computer model (DLA) [15] constructing a fractal cluster on the plane as a results of random walks of particles which are thrown one by one. Then this model was widened and modified, that resulted in the description of RLA which allowed the modelling by addition of a physical parameter of a given environment, and CCA model which considered the motion of clusters not particles.

The second approach to the diffusion modeling is based on a widened notion of cellular automata. In this notion any alphabet, any transition functions and any regimes of the change of cell states are possible. Such a wide interpretation of cellular automata allows us to construct mathematical descriptions of space-time processes of various character including the processes with self-organisation ([1], [4])

In practical application it is important to use the modelling both on surfaces and in the space. An implementation of DLA algorithm on the bone surface and based on cellular automata approach was proposed in [4]. In [2] the optimized DLA algorithm on triangulated surface based on random walk was designed and implemented. CCA model was applied to study

processes in colloidal solutions and aerogels, the implementation was made in space configuration [10,11].

In this work we present based on random walk imitation modelling for DLA, RLA and CCA models. Optimized DLA and RLA are realized on triangulated surface, for CCA it is shown that in the framework of classical model a correct implementation on a surface is impossible without an assumption about the cluster restructuring.

The software implemented on Python includes the following algorithms

- Triangulation of a surface by the marching method
- Base and optimized DLA for triangulated surface
- RLA
- CCA on a square lattice
- Visualization of results in 3D

The paper is organized by the following way. In sections 2 and 3 DLA model and its optimization both on the plane and a triangulated surface are described. The CCA model is discussed in the next section. In 5 we describe RLA model. The results of numerical experiments are given.

2. DLA MODEL

2.1. Witten-Sander base model

In this variant particles are thrown on the plane randomly and walk by random way on a square lattice. The initial particle is considered as a cluster. Every next particle may move equiprobably in 4 directions – up, down, left, right – on the lattice lines or cells. A particle joins to the cluster if it is a neighbour for a particle in the cluster. The choice of a way of moving depends on the representation of a particle – it may be presented by a vertex of the lattice or by a cell. The representation naturally influences on the visualization results.

2.2. DLA on triangular lattice

In this case we should define the directions of the particle transitions. For a particle being in a triangular with sides a, b, c define the probabilities to move in neighbour triangulars through corresponding sides as follows

$$p(a) = \frac{1/a}{1/a + 1/b + 1/c} \qquad (1)$$

$$p(b) = \frac{1/b}{1/a + 1/b + 1/c}$$

$$p(c) = \frac{1/c}{1/a + 1/b + 1/c}$$

Divide the segment [0,1] on intervals proportionally these probabilities. Choose a random number and depending on the interval in which it lies take the neighbour cell.

For example in the triangular with sides 3, 4, 5 we have p(a)=20/47, p(b)=15/47, p(c)=12/47. The unit segment is divided as [0, 20/47, 35/47, 1]. If the random number is in the first interval we go to the neighbour triangular through side a, etc.

3. OPTIMIZATION OF DLA ALGORITHM

In applications the base DLA model has some disadvantages:

1. Every particle moves on a lattice chaotically and the number of steps is unbounded. Hence for large parts of surfaces the number of steps which are required to join to a cluster grows indefinitely. Thus for the large number of particles the run time may be unpredictably large.
2. In real experiments one usually model several clusters on the same surface. But this fact is not taken into account, that also results in the run time growth.

It follows that in real modelling we have to use some restrictions on the number of particles, size of the surface and the number of particles in the cluster. Besides that we consider a variant optimization based on a reducing the number of random walking.

3.1. Optimization on square lattice

The optimization proposed in [2], defines the position of joining of a particle to a cluster in advance, at the moment when the particle is thrown on the lattice. For a square lattice with M cells we compute a matrix of choice of coefficients G [M, M] which will be used to define the particle position.

When a particle is thrown on a lattice the choice coefficients are calculated for each boundary points of the cluster. It is known [2] that these coefficients depend on only the sum of coordinate distances (a on abscissa and b on ordinate) between a new particle

and boundary points of the cluster and may be calculated as

$$p(a,b) = \frac{1}{4(a+b)} \qquad (2)$$

We consider the obtained coefficients as values of a distribution function, choose a value randomly and the preimage of this value defines the position of joining.

3.2. Optimization on a surface

For a triangulated surface we present the structure of a lattice by a graph, such that triangles correspond graph vertices, and edges between vertices mean that these triangles are adjacent. Define on edges (paths by length 1) weights (choice coefficients) which are calculated by (1). Write these weights in a matrix G_1. Then construct a sequence of matrices $\{G_k\}$, such that G_k contains choice coefficients for k-length paths. The weight of a path equals the product of weights of edges.

In G_1 denote by $p(i,j)$ the weight of the edge (i,j). Let $p(i,j) = y$, and $p(j,j_1) = y_1$, $p(j,j_2) = y_2$, $p(j,j_3) = y_3$ for neighbors of *j*. Then in G_2 in elements with indices (i,j_1), (i, j_2), (i, j_3) the coefficients $p(i,j_1) = yy_1$, $p(i,j_2) = yy_2$, $p(i,j_3) = yy_3$ will be written. Thus (i,j_1) corresponds to the 2-length path from i to j_1 and its weight is the product of the edges of the path. The matrices of higher order are constructed by analogy.

The common matrix of the choice coefficients is calculated as the sum of G_k, where k is from 1 to a given N. The position of the place of the joining to the cluster is defined by the analogy with the case 3.1.

The optimized algorithm may require more or equal time than the base one. The optimization results in considerable time gain when we conduct a series of experiments, because the matrix G is calculated one time for a given surface.

Summing up one may say that:

1. when modeling one cluster the base and optimized algorithms show close results. The optimized variant may be slower if the number of triangular is large.
2. when modeling the large number of clusters the optimized algorithm reduces run-time considerably.

The optimized algorithm for a triangulated surface was implemented in [3].

In the next table the results of the both algorithms on the surface $x^3 + y^2 + z = 0$ are given. The number of triangles is 4000, the number of particles in cluster is 500.

Table 1. The comparison of base and optimized DLA algorithms

The number of clusters	Base DLA	Optimized DLA
1	5m 56s	6m 59s
5	53m 11s	11m 41s

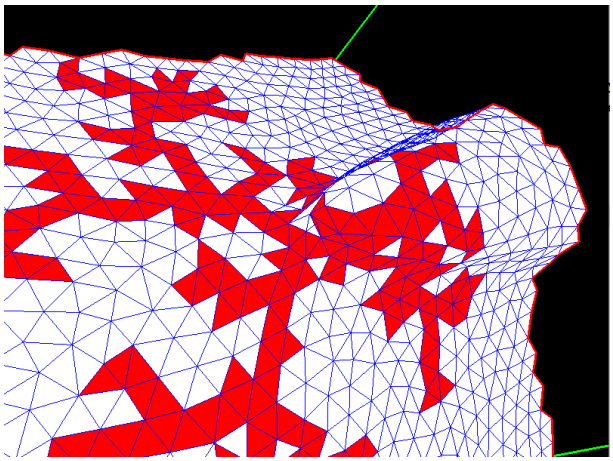

Figure 1. The result obtained by optimized DLA on the surface $\boldsymbol{x^3 + y^2 + z = 0}$

4. CCA MODEL

4.1. CCA on square lattice

This model was proposed in [9]. As opposed to particle-cluster model in this model the common number of particles is known and all of them are on the surface (or plane).

The particles randomly walk on the lattice. When 2 particles collide they join into a cluster, and this cluster continue to walk. It is assumed that the probability of collision of 3 or more clusters is very small. At the end of the modelling we have a final aggregate.

The movement of a cluster on square lattice is similar to the movement of a particle –-on every step the cluster may move one cell left or right or up or down equiprobably. Clusters are considered to be sticky if at least one particle of the first cluster is on the cell which is neighbor of a particle of the second one. In such a situation due to the square lattice, a cluster moves as a single whole and saves his structure.

4.2. Problems of CCA on triangular lattice

On a triangular lattice we not always can model the cluster movement to save its structure. To explain

the situation we give the following definitions. We call the movement of a cluster ***correct*** if

1) every particle of the cluster passes through the same number of the cells of the lattice.

2) the number of particles does not change, i.e the structure is preserved.

The movement of a cluster is ***semi-correct*** if only 1) or 2) holds. The movement is ***incorrect*** if it is not correct or semi-correct.

It is easy to note that the movement of a cluster on square grid is correct, because all the particles pass the same distance in a chosen direction and the structure is preserved.

On a regular triangular grid the movement of a cluster may be only semi-correct. In this case different particles may pass different distances and move in different directions. Hence to save the structure the cluster has to turn. In other words we cannot move the cluster as a single whole. Such a situation is explained by the structure of triangular lattice.

On Fig.2 the red cluster on the left part of the picture moves in the direction marked the black arrow on 1 cell. On the right side its initial position (blue color) and the result of the movement (red color) are shown. We see that some particles pass 1 cell, and one particle should pass 3. We see that the cluster makes 1 step, but to do it possible the particles should pass different number of cells. According to our definition the movement is semi-correct, because 1) does not hold. Note that this situation is possible only for regular triangular grid on the plane.

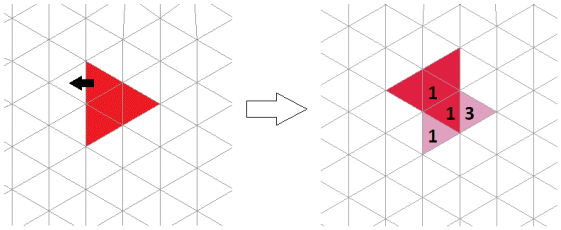

Figure 2. The example of the motion of a cluster on regular triangular grid: particles of the cluster make different number of steps

For non-regular triangular lattice the nodes of the lattice may have different number of neighbors and it does not allow preserving the structure of a cluster. This situation is illustrated on Fig.3. Blue cluster consists of 5 particles, every particle has 2 neighbors. We cannot move it into red area without changing the structure.

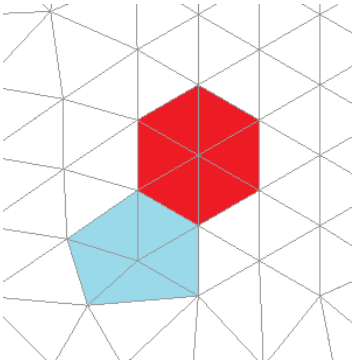

Figure 3. Restructuring on non-regular grid: blue cluster cannot be moved to the red area without changing its structure

Thus, it is impossible to implement CCA algorithm on a non-regular lattice without modifications allowing the cluster restructuring. For example in [17] the authors assumed that a cluster may spin, and when 2 clusters stick together they can spin in the point of contact. They also proposed that there is a tension between particles, hence particles may influence each other in the process of the cluster growth. It may lead to a change of the cluster structure.

In real tasks the modelling of CCA on a surface has a limited scope of application, and the modelling in the space is more important. In this case some problems appearing for non-regular lattice on a surface may be solved and a cluster may be admitted to turn or change a structure. Such a model may be used when studying colloid solution or aerogels. In [16] an interesting variant of CCA space model in a boundary area was implemented: when cluster collides with boundaries it moves in opposite direction. This model may be applied to the modelling of nanoscale medicinal products [10], catalytic reactions [11] and physical properties of materials.

5. RLA MODEL

To take into account physical properties of a real environment we should introduce some parameters. In this model the probability of joining a particle to a cluster is considered.

Proposed in [7] RLA (Reaction Limited Aggregation) model describes the growth of a fractal cluster when the probability of sticking together is small. In [12] the authors merged CCA and RLA models, introduced the binding energy between particles and assumed that the probability of sticking depends on the time of random walking and the time of breaking binds. Thus the probability of sticking is dynamical.

We implemented RLA on a triangulated surface and used a probability of sticking as a parameter. This is a modification of DLA and may be performed both for base and optimized variants.

If a particle is near a cluster and the probability of sticking p_s is small it continue to walk. Denote the number of walks by *N* and the number of walks which lead a particle to a cluster by N_w. One may assume that the less p_s the more N_w. For example if $p_s = 0.2$ we may take $N_w \leq 10$, and for $p_s = 0.5$ take $N_w \leq 6$. If after N walking $N_w = 0$ (the particle did not get closer to the cluster) we delete the particle and throw a new one.

The example of the construction of the aggregate on the surface $x^3 + y^2 + z = 0$ for $p_s = 0.1$ (left) and $p_s = 1$ (right) is shown on Fig. 4. The number of triangles is 1419, the number of particles is 200.

The run-time for $p_s = 0.1$ is 1m 3s, and 19s for $p_s = 1$.

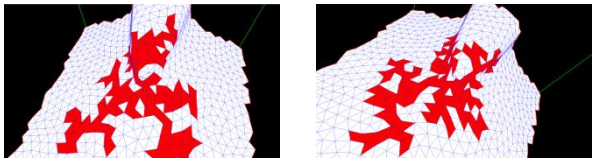

Figure 4. RLA model on the surface

$$\boldsymbol{x^3 + y^2 + z = 0}$$

$$\boldsymbol{p_s = 0.1}\ \text{(left)} \quad \boldsymbol{p_s = 1}\ \textbf{(right)}$$

The triangulation was performed by the marching method proposed by E. Hartmann [5]. It is quite simple to implement and may be applied to any type of a surface. The size of the lattice may be defined by a parameter.

6. CONCLUSION

Mathematical models of diffusion are rather complex and as a rule do not have analytical solutions. For a successful study of diffusion processes one should combine mathematical and numerical methods and imitation modelling. In this work we present a program system for the imitation modelling of the growth of fractal clusters on a triangulated surface by DLA and RLA models. It is shown that CCA model cannot be implemented on a triangular grid without a restructuring of a cluster. The program may be useful both for researchers and students.

References

[1] Bandman O. L. Cellular Automata composition techniques for spatial dynamics simulation. Bulletin of the Novosibirsk Computing Center. 2008. No.27. p. 1–40.

[2] Batyukov A. Design and implementation of classification algorithms of digital images of biomedical preparations. — Ph.D. thesis /A.M. Batyukov; St. Petersburg State University, 2015.(in Russian)

[3] Doronin G.A. Modeli agregacii ogranichennoi diffusiei na tranguliruemih poverhnostiah.Proc. Conf. LXXIV Herzen Readings, 5-10 April, 2021, St.Petersburg, p. 218-223. (in Russian)

[4] Evseev A. Kletochno-avtomatnoe modelirovanie diffusionnih processov processov na trianguliacionnih setkah. Prikladnaia discretnaia matematika 27. Tomsk, isd. Tomskogo universiteta, 2009. No 4(6). p. 72-83.

[5] Hartmann E.. Geometry and Algorithms for computer aided design. Department of Mathematics Darmstadt University of Technology, 2003. Geometry and Algorithms for COMPUTER AIDED ehartmann/ and Algorithms for COMPUTER AIDED DESIGN Erich Hartmann Department of Mathematics Darmstadt University of Technology October 2003 (pdfslide.net)

[6] Hasmy A., Primera J., Woignier T. Cluster–cluster aggregation with mobile impurities. — Journal of Sol-Gel Science and Technology., 2019. DOI: 10.1007/s10971-019-04918-3

[7] Julien R., Kolb M. — J. Phys. –1984, Ser. A. –V.17. – P.L639.

[8] Kassner K. Pattern Formation in Diffusion-Limited Crystal Growth.—Singapure: World Scientific, 1996.

[9] Kolb M., Botet R., Julien R. — Phys. Rev. Lett. –1983. – V.51. – P.1123.

[10] Lebedev I. V., Khudeev I. I., Kolnoochenko A. V., Tyrtyshnikov A. Y., Ivanov S. I., Menshutina N. V. Silica-resorcinol-formaldehyde aerogels nanostructure modelling. — Chemical Engineering Transactions, 70, 1765-1770., 2018.

[11] Menshutina N., Lebedev E.,Kolnoochenko A.,Tsygankov P.,Lebedev I. Complex Modeling and Design of Catalytic Reactors Using Multiscale Approach — Part 1: Diffusion in Porous Catalyst. — Computation, 8(1),11., 2020.Shih W. Y., Aksay I. A., Kikuchi R. — Phys. Rev. –1987, Ser. A. –V.36.– P.5015.

[12] Smirnov B.M. Physica fractalnih clasterov. — M.,Nauka, 1991. (in Russian)

[13] Wiegel F., Perelson F. — J. Stat. Phys. V.29 P.813, 1982.

[14] Witten T. A., Sander L. M. Diffusion-Limited Aggregation, a Kinetic Critical Phenomenon. — Physical Review Letters., 1981.

[15] Zhukova I., Kolpak E. Mathematical models of malignant tumor. Vestnik SPbGU—2014, ser. 10, n.3, c. 5-17. (in Russian)

[16] Zirianov R. Razvitie fractalnih modelei agregacii kolloidnih chastits. Molodoi uchenii. No. 24 (128), p. 72-76., 2016. (in Russian)

A HUMAN SUPPORT SYSTEM IN A SMART HOME ENVIRONMENT

I. Nebogatikov, I. Soloviev

St. Petersburg State University, Comp. Sci. Dept.
st049100@student.spbu.ru, i.soloviev@spbu.ru

Abstract

In this work we describe the principles of the life support system of the smart home inhabitant. The system involves monitoring the activity and classification of the activity types of inhabitants using artificial intelligence methods, controlling the duration of their actions, the response functions and the necessary social support. The system is implemented on the Google Smart Home platform.

1. INTRODUCTION

Automatic assistance for a human in everyday life and emergency situations, and social, specialized medical and other support are current topics in technical, and social research [2]. This is a part of the program for the creation of a comfortable and safe environment for humans with their pets, and, in particular, it involves the equipping a person's home with additional “smart” hardware and software tools [10].

The organization of such an environment may also include the implementation of various strategies to support the life of the inhabitant, for example, assistance in tracking the schedule of medication, strolling, exercises, etc. Such a home is often called "smart home" [11, 12].

In addition to the basic tasks solved with smart home systems that offer the optimization of household with static smart household devices, we can recognize a subclass of specific tasks for the inhabitant life support [1]. To solve such problems it is necessary to obtain accurate information about the current activity of a person.

In many cases to determining the current human activity we can use static devices, wearable devices, or a combination of them. Activity recognition systems differ by the approach that has been taken. It could be classification, recognition of predefined types of activity, or clustering, automatic recognition of activity type templates.

This paper describes the developed and implemented program system designed for monitoring and recognition (classification) activity of the inhabitants of a smart home using wearable sensors, a smartphone and a fitness tracker. Classification problems were solved by various methods of machine learning.

The obtained information is used to create a human support system that includes a subsystem for monitoring the duration of actions of inhabitants to maintain a healthy rhythm of life as a personal request or the doctor’s recommendation.

In the presented work we describe the implementation performed with the Google Smart Home management programming environment [13]. We focus on the problems of choosing appropriate classification methods and creating a classifier of the activity of smart home inhabitants. As an example, a subsystem for monitoring the duration of activity was designed and implemented.

2. DATA DESCRIPTION

In previous studies [2], we used open access human activity data [14, 15] and the information obtained from wearable devices to select appropriate classification methods and the system configuration. The analysis of these datasets showed insufficient accuracy in recognizing the type of activity for practical usage. Therefore, for this study, an experimental dataset about the activity of an inhabitant of smart home was prepared. The data over a period of three weeks using wearable sensors were collected

Considering the information of large number of sensors, the readings of which are merged to a single class can lead to decreasing of classification accuracy [3]. Therefore, a fitness tracker and a smartphone, which are currently the most common sensors, were selected. With their readings we can determine the location of a person inside the home and his condition.

With using a smartphone, information about a human's indoors location is collected. This can be done basing on the readings of the Bluetooth or Bluetooth Low Energy receiving signal strength indicators

(RSSI) with a fitness tracker or smart watch and the indicators of signal strength of the smartphone connection with a Wi-Fi router [4]. The RSSI values are in the range from -100 to 0, the closer the value is to 0, the stronger the signal. In this work we assume that there is only one Wi-Fi router in the system, that is accessible from all the locations of the smart home environment.

The fitness tracker allows us to get more detailed information about the current type of an inhabitant's activity. In applications that use the information collected by the accelerometer, it is possible to use only the readings converted to the steps number, because the accelerometer readings are not transmitted from the fitness bracelet directly to the smartphone to save energy.

To get information about the heartbeat and the number of steps, the open source Gadgetbrige application for Android devices was used. This application is designed to replace the applications of fitness tracker manufacturers, because various device vendors use their own protocols for interacting with the wristband and smartphone. The functionality that allows getting RSSI information has been added to the application.

The resulting data set contains the following data types:

- heart rate;
- number of steps;
- Bluetooth RSSI;
- Wi-Fi RSSI;
- activity time;
- type of activity.

Information of 9 types of activity was collected: work, eating, cooking, walking, video games, inactivity, sports, shower, household.

The interaction with a user on sleep monitoring and control is implemented by applications of manufacturers of fitness trackers, so this type of activity was not considered for collecting information and solving the problem of monitoring the duration of activity.

Therefore, to configure the system, we got a dataset with 26709 records, each activity type contains no more than 4800 records.

3. DATA ANALYSIS AND EXPERIMENTS DESCRIPTION

For the recognition of activity type, we used machine learning algorithms that were commonly applied to solve problems related to human activity recognition. The experiments were made with using the cross-validation method, which divides the sample into 10 folds (groups of samples of equal size). The recognition accuracy (the ratio of correctly predicted values to the total size of the test subset) and standard deviation are shown in table 1.

Table 1: Accuracy comparison

Algorithm	Accuracy	Standard deviation
Neural network	0.739	0.01
K Nearest neighbours	0.815	0.006
Random forest	0.824	0.008
Naïve Bayes classifier	0.677	0.005
AdaBoost	0.456	0.003
Support Vector Machines	0.679	0.008

From the table we can see that the classifiers with a random forest containing 100 trees [5], and K nearest neighbours with K=10 have highest classification accuracy. The recognition quality of high movement activities using the random forest classifier is significantly lower than using the K nearest neighbours method, as shown in table 2. The accuracy of activity type recognition (precision) is calculated as the ratio of correctly defined objects of a class to the sum of correctly and falsely classified values.

Table 2: Precision comparison

Activity type	K nearest neighbours	Random forest
Work	0.922	0.947
Eating	0.515	0.488
Cooking	1.000	1.000
Walking	0.692	0.768
Video games	0.724	0.788
No activity	0.846	0.877
Sports	0.579	0.304
Shower	0.823	0.872
Household	1.000	1.000

To increase the recognition accuracy and take advantages of both types of classifiers, the hierarchical classification approach was applied, which allows us to consistently specify the belonging of an object to the classes the structure of which is a tree. All activities were divided into 2 basic types: dynamic and static.

In this work various combinations of classifiers using K nearest neighbours methods and random forest as basic recognition methods were reviewed, as the

training of classifiers on a subset of the original set of classes changes the quality of classification. The accuracy of recognition of activity classes from the data set obtained with hierarchical classifiers is shown in tables 3 and 4. The first classifier recognizes the basic type of activity, the second one — passive activities, and the third one — dynamic activities.

The approach that uses the K nearest neighbours algorithm to recognize dynamic activities and the random forest method at the remaining points solve the problem of low classification precision for high movement types of activity.

Table 3: The comparison of precision for hierarchical classifiers

Activity type	Random forest, K nearest neighbours, Random Forest	Random forest, Random Forest, Random Forest
Work	0.931	0.950
Eating	0.685	0.598
Cooking	1.000	1.000
Walking	0.715	0.715
Video games	0.753	0.786
No activity	0.866	0.879
Sports	0.474	0.474
Shower	0.804	0.804
Household	1.000	1.000

Table 4: The comparison of precision of hierarchical classifiers

Activity type	K nearest neighbours, Random Forest, Random Forest	Random forest, Random Forest, K nearest neighbours
Work	0.943	0.950
Eating	0.539	0.598
Cooking	1.000	0.996
Walking	0.694	0.658
Video games	0.770	0.786
No activity	0.874	0.879
Sports	0.480	0.711
Shower	0.847	0.773
Household	1.000	1.000

The selected hierarchical classification scheme is shown in Figure 1. The basic activity type is recognized by the base classifier using the random forest algorithm. Two subsequent classifiers refine obtained result. The first is recognizing static types of activities using the random forest method, and the second is recognizing dynamic activities using K nearest neighbours.

The implemented classification algorithm increases the precision of recognition "sport" activity type from 0.304 with the use of a random forest, up to 0.711.

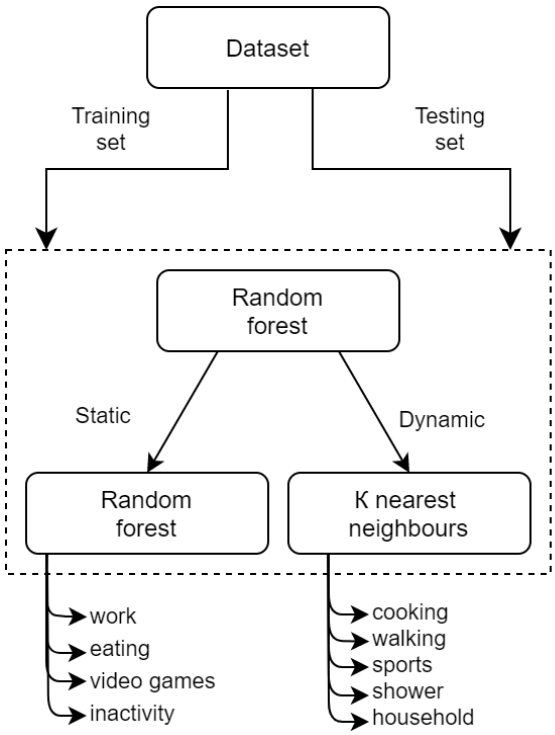

Figure 1. Hierarchical classification schema

The implemented system allows recognizing 9 types of activity with an accuracy of 0.838 using a hierarchical approach, and with data obtained from a heart rate sensor, step counter, Bluetooth and Wi-Fi RSSI.

The system can be compared with existing solutions by the set of sensors used, the classification algorithm used, the number of recognized classes, and the accuracy of classification:

- In [6], the authors used random forest algorithms and the support vector machines method to recognize 5 classes of activity (sitting, standing, doing household, working on an exercise bike with low activity, working on an exercise bike with high activity) based on the accelerometer and heartbeat data obtained from a smart watch. The classification accuracy is equal to 89.2% for the random forest algorithm and 85.6% for the support vector machines method.
- The article [7] describes a hierarchical modification of the support vector machines method for recognizing four types of activity with 99% accuracy. The method is based on data obtained from smartwatches: when a person is sitting or standing, walking or running.

- In [8], the author used 2 devices equipped with an accelerometer and a gyroscope. One of the sensors was attached to the wrist, and the second is located in the pants pocket. F-measure (the harmonic mean of precision and recall, where recall is defined as the ratio of correctly defined class objects number to the sum of correctly and falsely classified values) of the recognized types of activity was close to 1. A hierarchical classifier that divides the types of activity into the types that involve only the hands and the other types of activity was used. The algorithms of the naive Bayesian classifier and K nearest neighbours are used as the basic classification algorithms.

The implemented classifier provides the accuracy of recognizing the activity of a smart home inhabitant, which is comparable to the accuracy of recognizing human activities in the presented researches.

4. THE SYSTEM MONITORING THE ACTIVITY DURATION

The using existing hardware and software implementations of smart environment management simplifies the user interface development. This approach also allows us to store and exchange of information of several human support modules that use the same sets of information to solve several independent tasks [9].

Monitoring the duration of human activity in the Google Smart Home environment takes place using two functional features: the user changes the desired parameters of the duration of recognized actions, and receives a notification when the specified limits are exceeded.

The details of interaction of an inhabitant and the system are shown in Figure 2.

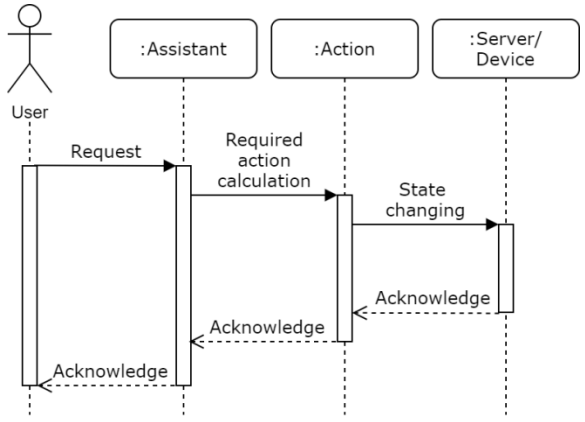

Figure 2. Interaction with Google Smart Home environment

The user sends a request to change the time of the activity duration using the voice or text interface of Google Assistant. The assistant calculates the required action for execution, where action is an implementation of a custom script for the smart environment management. The action handler sends the received parameters to the server via the REST API. The server returns a message confirming the update of the information.

Figure 3 shows a sequence diagram of the process of receiving a notification by an inhabitant about exceeding the established limits for the duration of activity. After receiving the heart rate and the count of steps from the fitness tracker, Gadget Bridge application adds the Wi-Fi and Bluetooth RSSI values and sends the information to the server where the described activity classifier is installed.

If the duration of the recognized activity type is outside of the established limits, smart home inhabitant receives a notification on the smartphone.

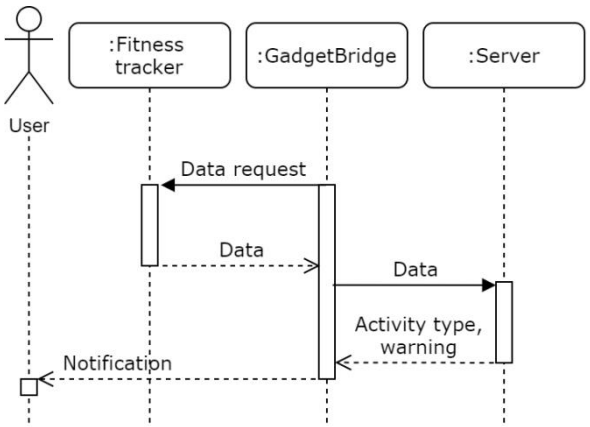

Figure 3. Notification receiving diagram

5. CONCLUSION

In this work, the problem of classification of the smart home residents activity was solved by hierarchical classification method including random forest and K nearest neighbours algorithms. The accuracy is 0.838, which is sufficient for a practical application of the classifier.

The use of the developed and implemented system for monitoring the duration of human activity in the smart home environment allows supporting the inhabitants and helps to maintain an optimal life rhythm by receiving notifications on a smartphone.

References

[1] T. Juhana, and V. Gusti Anggraini, "Design and implementation of Smart Home Surveillance system", 10th International Conference on Telecommunication Systems Services and Applications (TSSA), 2016, pp. 1–5.

[2] I. Y. Nebogatikov, and I.P. Soloviev *J. Phys.: Conf. Ser.,* 2021.

[3] A. Kirienko, and I. Soloviev, "Human Behaviour Analysis in Context of Smart Environment Automation", Computer tools in education, 2017, pp. 15–29.

[4] J. Correa, E. Katz, P. Collins, and M. Griss, "RoomLevel Wi-Fi Location Tracking", Carnegie Mellon University, 2018.

[5] T. Oshiro, P. Perez, and J. Baranauskas, "How Many Trees in a Random Forest?", Lecture Notes in Computer Science, 2012, pp. 154–68.

[6] S. Mehrang, J. Pietila, T. Tolonen, E. Helander, H. Jimison, M. Pavel, and I. Korhonen, "Human Activity Recognition Using A Single Optical Heart Rate Monitoring Wristband Equipped with Triaxial Accelerometer", EMBEC, 2017, pp. 587–590.

[7] T. Tang, L. Zheng, S. Weng, A. Peng, and H. Zheng, "Human Activity Recognition with Smart Watch based on H-SVM" International Conference on Frontier Computing, 2018, pp. 179–186.

[8] M. Shoaib, S. Bosch, O. Incel, H. Scholten, and P. Havinga, "Complex Human Activity Recognition Using Smartphone and Wrist-Worn Motion Sensors", Sensors, 2016.

[9] L. Min, G. Wenbin, C. Wei, H. Hed, W. Yannian, and Z. Yiying, "Smart Home: Architecture, Technologies and Systems", 8th International Congress of Information and Communication Technology (ICICT-2018), 2018.

[10] J. Bennett, O. Rokas, L. Chen, "Healthcare in the Smart Home: A Study of Past, Present and Future", *Sustainability*, 2017.

[11] M. Sripan, X. Lin, and M. Ketcham, "Research and Thinking of Smart Home Technology", Research and Thinking of Smart Home Technology, 2012.

[12] L. Rossi et al., "Interoperability issues among smart home technological frameworks," 2014 IEEE/ASME 10th International Conference on Mechatronic and Embedded Systems and Applications (MESA), 2014, pp. 1-7, doi: 10.1109/MESA.2014.6935626.

[13] H. Isyanto, A. Arifin, and M. Suryanegara, "Design and Implementation of IoT-Based Smart Home Voice Commands for disabled people using Google Assistant", International Conference on Smart Technology and Applications (ICoSTA), 2020, pp. 1-6.

[14] O. Bouarada, "heart rate and breathing data" [Electronic resource]. Access mode: https://www.kaggle.com/onnsbrd/heart-rate-and-breathing-data?select=final_ecg_data.csv (Access date: 16.06.2021).

[15] S. Jafarnejad, "An Open Dataset for Human Activity Analysis" [Electronic resource]. Access mode: https://www.kaggle.com/sasanj/human-activity-smart-devices (Access date: 16.06.2021)

GUI FOR IMAGE FUSION IN MEDICAL IMAGES OF BRAIN

Diana S. Tsvetkova

Faculty of German Engineering Education and Industrial Management, Technical University of Sofia, Bulgaria
1000 Sofia, "Kl. Ohridsky" str.8
E-mail: diana.tsvetkova@fdiba.tu-sofia.bg

Veska Georgieva

Faculty of Telecommunications, Technical University of Sofia, Bulgaria
1000 Sofia, "Kl. Ohridsky" str.8
T. (+359 2) 965-3293; E-mail: vesg@tu-sofia.bg

Abstract

In recent years of great technological development, medical diagnostic and treatment require great precision from various medical imaging methods such as Magnetic Resonance Imaging (MRI), Computed Tomography (CT), Single-photon emission computed tomography (SPECT) etc. These imaging methods often give unique information. Therefore, a post imaging method known as image fusion is often applied. This method synthesizes information from two or more images into one single image that carries all the relevant data. In this paper we propose a program and simple specialized Graphical User Interface (GUI), which is developed in MATLAB-environment. Different wavelet-based image fusion methods applied on MRI and SPECT medical images of brain can be analyzed on the base of different wavelet decompositions. The proposed GUI can be applied in Computer Aided Diagnostics for real images attempt to make medical diagnosis more precise. The presented GUI is suitable also to engineering education for studying of medical image fusion.

1. INTRODUCTION

Magnetic Resonance Imaging (MRI) is a medical imaging modality that can obtain images of the soft tissue and the non-bony parts such as blood vessels, ligament tears and many more. Talking about imaging of the brain, this medical imaging method shows the brain structure. The obtained images are usually good quality.

On the other hand, the Single-Photon Emission Computerized Tomography (SPECT) is a medical imaging modality that is used to present the blood circulation on different tissues and organs. When imaging the brain, the cerebral blood flow is measured and is used for diagnostic of brain diseases such as dementia. However, often these image sequences are difficult to interpret, because they could be blurred.

The growing appeal on using image fusion in the field of medicine can be observed from the large number of scientific papers published since 2000 on the topic [1, 2, 3, 4]. In publication [5] an image fusion GUI is developed, whereas the same techniques are used as the GUI in this article, but the input images are MRI and CT. Compared to the developed GUI in this paper, the GUI in [5] is used only for analysing the general combinations of wavelets and fusion rules that obtain the highest result. However, in our investigation, not only the fusion rules are taken into account when analysing the result, but also the different wavelet functions from different wavelet families and their decompositions levels, making this study more comprehensive.

The rest of the paper is structured as follows. In Section 2, the briefly theoretical part is given. In Section 3, the GUI for wavelet-based medical image fusion is presented. Section 4 describes tasks carried out from the main program. Some experimental results are presented in Section 5. Concluding remarks are given in Section 6.

2. THEORETICAL PART

The wavelet image fusion is done in three stages: first is the decomposition of the source images at different levels using tensors; than the combination of the obtained wavelet coefficients is performed. The approaches used when combining these coefficients are called Fusion rules; an inverse wavelet transform is applied to obtain the fused image. A graphic of wavelet-based image fusion is shown on Figure 1.

On Figure 1, it is denoted that the two input medical images from different medical modalities are image A and image B. The first step of the algorithm is to decompose each source image with the help of wavelet transform into wavelet coefficients. In this

case, the multidimensional wavelets can be presented as a tensor product of separable basis functions, defined in every dimension. Knowing this, the wavelet decomposition can be defined as a set of wavelet coefficients, where the scaling wavelet function $\varphi(x,y)$ can be presented in Eq.1 as the tensor product [6]:

$$LL = \varphi(x, y) = \varphi(x).\varphi(y) \quad (1)$$

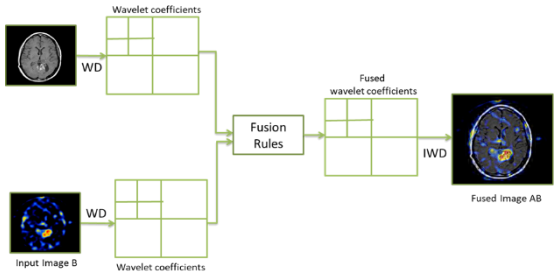

Figure 1. Wavelet Image Fusion scheme

Than in Eq.2 the wavelet functions $\Psi(x,y)$ are as follows

$$\begin{aligned} LH &= \Psi_{LH}(x,y) = \varphi(x).\Psi(y), \\ HL &= \Psi_{HL}(x,y) = \Psi(x).\varphi(y), \\ HH &= \Psi_{HH}(x,y) = \Psi(x).\Psi(y), \end{aligned} \quad (2)$$

where L represents the usage of a low pass filter and H – the usage of a high pass filter. The decomposition stage transforms the image into approximate and informative coefficients using Tensor Wavelet Decomposition (TWD) at some specific level. Therefore one 2-dimensional wavelet function LL is obtained, representing the low-frequency band. This image contains maximum energy and information. Obtained are also three more 2-D wavelet functions (LH, HL and HH), describing the high frequency bands. These images are called detailed or informative, thus they describe different types of image details. The LH (Low-High) subimage represents information about the horizontal edges, HL (High-Low) subimage contains details about the vertical edges and the HH subimage describes the diagonal details. For obtaining a next level of decomposition, the decomposition stage is carried out, but this time the approximation coefficients (LL) from the previous level are used.

After both images are decomposed and their wavelet coefficients are obtained, the second stage occurs. This is the stage where the obtained wavelet coefficients from images A and B are fused. This means that the approximation and detail coefficients from both images are combined together obeying *fusion rules* in order to form one fused image. The fusion rules used, are from the category of spatial fusion techniques. They present a way of fusing medical images without using significant part of the resources of the computer [7]. The simple Fusion techniques fuse separately the detail and approximation coefficients. Three main techniques are presented in the Image Fusion GUI: Average selection scheme, Minimum selection scheme and Maximum selection scheme and Adaptive scheme. The third step of developing fused image is to perform an inverse wavelet transform that makes it possible to visualize the fused image AB. This image contains the synthesized coefficients from both images.

3. GUI FOR IMAGE FUSION

For solving the task of image fusion, a specialized Graphical User Interface (GUI) is developed in MATLAB-environment. The interface will enable the user to perform wavelet image fusion on two medical images, while giving the user an opportunity to test different combinations of wavelet decomposition methods and fusion rules.

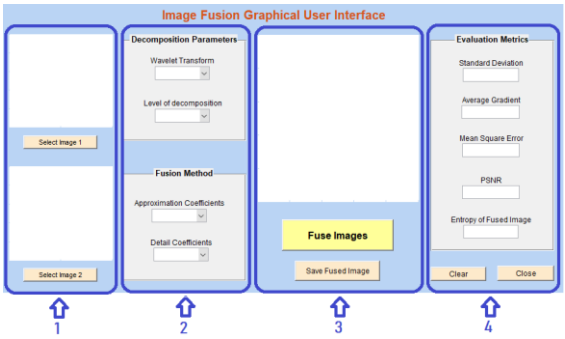

Figure 2. GUI for wavelet image fusion

The initial state of the GUI can be seen on Figure 2, where 4 panels can be defined. Panel one gives the user the opportunity to select the two input images. When button "Select Image 1" is clicked-on, the user can navigate among the folders in the workspace and choose image, after that the chosen image is displayed on the axes above the button. Pushing the button "Select Image 2" give the user the opportunity to select the second image in the same manner. This action is demonstrated in Figure 3.

If the two selected images do not have the same size, image fusion is unapplicable and the GUI shows an error window explaining the problem to the user. This is demonstrated on Figure 4.

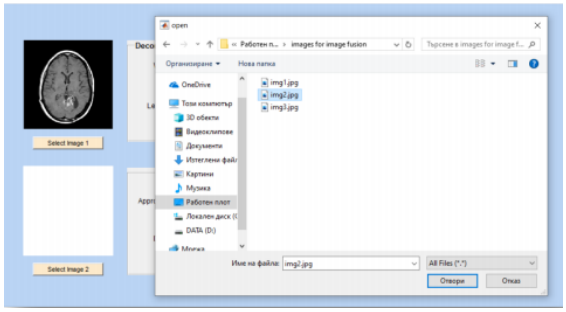

Figure 3. Image Selection

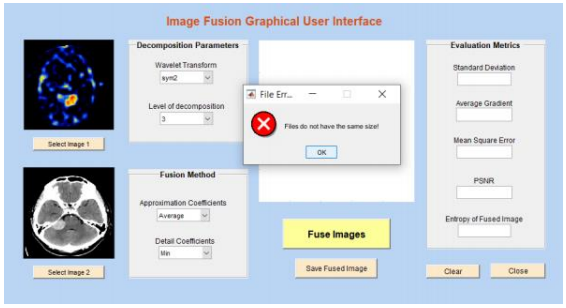

Figure 4. Error for uneven size of input images

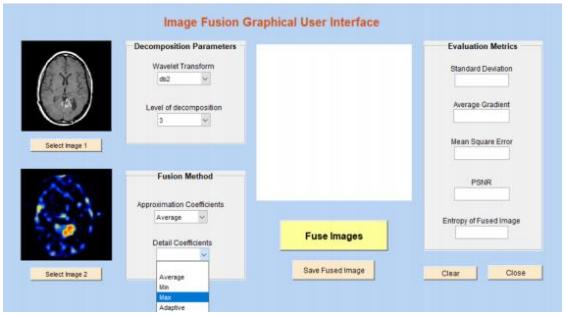

Figure 5. Parameter selection

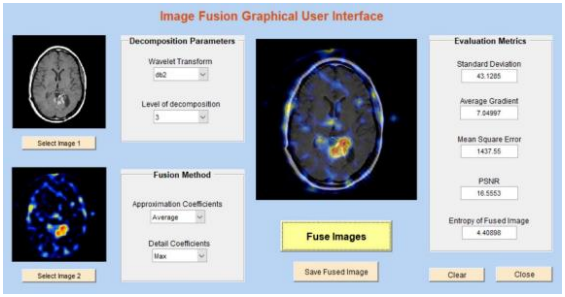

Figure 6. Fused image

Panel two enables the user to test out different combinations of image decomposition and image fusion rules. The upper part of this panel is responsible for the selection of the Decomposition Parameters. The user can select one of the predefined wavelet transforms (haar, db2, db20, sym2, sym3, coif1, dmey) using the drop-down menus [7]. For selected wavelet function we obtain very good results for image fusion. The available options for wavelet transforms are not random. Taken in account the study [8], the same wavelet transforms are presented, since they have achieved the best results.

The selection of a different level of decomposition from 1 to 5 is also possible with the help of a drop-down menu. We obtain bad quality of the fused images for decomposition levels higher than 5. The lower part of the second panel is for the selection of the image fusion rules. Thus, the main fusion method synthesizes separately the Low- and the High-Frequency subbands, there are two drop-down menus in this subpanel: one for fusing the approximation, and the other is for choosing the fusion rule that the functions of the detail coefficients should be selected. The selection of the fusion rule for the detail coefficients is demonstrated at Figure 5.

Panel 3 have two important buttons. The button *Fuse Images* applies all of the user preferences and fuses the input images. The user can also press the button *Save Fused Image* and can save the resulting image onto his workspace. The result of pressing the button *Fuse Images* can be seen on Figure 6. The resulting image is shown on the axes above the buttons.

Right after the fusion happens on panel 4 the accessed metrics are calculated and shown. This enables the user to make quick and precise judgment of the fusion – is it successful or not. The Evaluation metrics shown are: Standard Deviation, Average Gradient, Mean Square Error, PSNR and Entropy of the fused image. For the better results of the MRI/SPECT fusion, the Entropy should be minimal, but PSNR should be as higher as possible Panel 4 contains two additional buttons – *Clear* and *Close.* The *Clear* button deletes all the preselected preferences and returns the GUI to its initial state, where the user can perform the image fusion again. The *Close* button simply closes the GUI and exits from the application.

4. TASKS, CARRIED OUT BY THE MAIN PROGRAM

The main algorithm working behind is shown on Figure 7.

The GUI is developed with the help of the graphic redactor GUIDE. After the computation of the GUI, two files are present: one „fig" file containing a figure that presents information concerning the outlook of the user interface and a ".m" file containing the main program. Within this program there are functions that define the work of each programmable component from the figure.

Each graphical component from the GUI is being handled as an object. Each object refers to a handle

(pointer) and has a list of properties that can be altered through programming if needed. Objects properties can be changed only if the object is defined by its handle or other type of reference. When initializing the GUI, each graphical component is registered in the MATLAB-environment and it is provided with a callback function, that can change the state and properties of the object. The formed callback functions are present in the main program and can be altered.

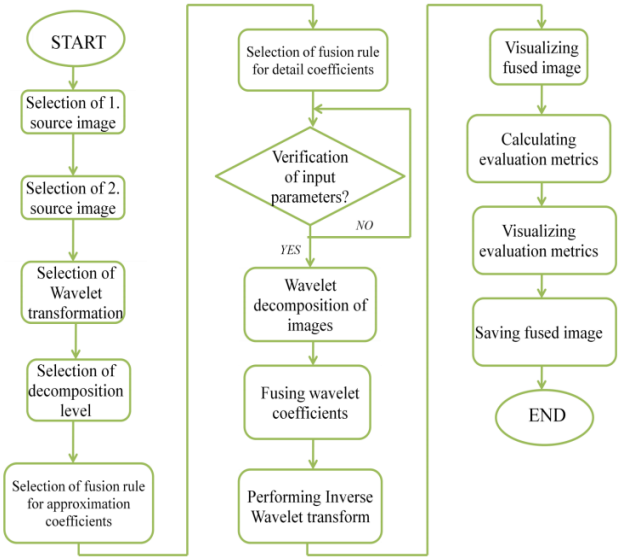

Figure 7. Block scheme of the program

Each callback function has the form: *Function Callback (hObject, eventdata, handles), where hObject* is a pointer that associates this specific function with its exact graphical component, providing the ability to change the properties of the graphical component from the main program. *Handles* is a pointer that can enable the saving and retrieval of information or other manipulations. The *eventdata* is a data structure that is reserved and will be used automatically from MATLAB in future versions.

In the development of this particular GUI the function *setappdata (obj,name,val)* stores the contents of „*val*". To identify the data for later retrieval, *obj* identifies the graphic object and name identifies the name, where the function *val=getappdata (obj, name)* retrieves data stored using the *setappdata* function. To retrieve the desired data – obj and name are used as identifications.

5. EXPERIMENTS AND RESULTS

Our investigations for application of the different methods of the medical image fusion and the multimodal imaging of the human brain have shown that the combination of an average fusion rule for the approximation coefficients and the detail coefficients gives better results.

Some experimental results can be seen on Table 1. It should be taken in account that Entropy of the fused image value should be minimal, since this indicates that the fused image is carrying greater information. and in the meantime, the Peak-Signal-to-Noise-Ratio (PSNR) value should be high, since larger values are associated with less noise in the fused image. It should be denoted that since we are working with medical images, the analysis of the evaluation metrics is not enough and a visual analysis of the fused image is also needed.

Table 1. Results for accessing fusion rules

Fusion Methods		Evaluation metrics		
Approxim.Coeff.	**Detail. Coeff.**	**MSE**	**PSNR**	**Entropy *imf***
Average	**Average**	**1.4016**	**16.6646**	**4.2764**
	Min	1.4178	16.6146	4.7628
	Max	1.4187	16.6118	4.7452
	Adaptive	1.5607	16.3121	4.9570
Min	**Average**	2.3382	15.8487	3.3094
	Min	2.3412	15.8170	3.4269
	Max	2.3424	15.8263	3.4535
	Adaptive	2.2734	15.2922	3.7806
Max	**Average**	2.4833	15.4966	5.7880
	Min	2.5020	15.4415	5.7858
	Max	2.5012	15.4339	5.7888
	Adaptive	2.6856	15.6521	5.6790

Figure 8 represents the image correspondent to this exact fusion method.

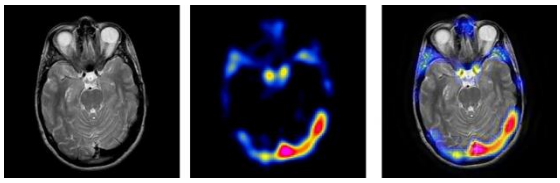

Figure 8. Successful image fusion of brain

Note that all the experiments are made with a *dmey* wavelet function at a *3rd* level of decomposition. More detailed information about the results in regard to the selection of a suitable wavelet function can be found in [7].

6. CONCLUSION

In this paper we present a program with GUI for image fusion in MRI and SPECT images of the brain. The developed program provides good opportunities on the task of image fusion, whereas the GUI enables the user to interactively select the input images

and all the needed setting for the execution of image fusion.

The program performs the task easily and calculates the evaluation metrics fast. This enables the user to analyse more data easily on the topic of medical image fusion. Note that images from SPECT could be blurred, therefore in a future work a pre-processing panel will be included in order to reduce the problems concerning the images from SPECT medical modality. The proposed GUI can help for making medical diagnosis more precise. The presented GUI is suitable also to engineering education for studying the process of medical image fusion.

7. ACKNOWLEDGMENTS

This work was supported by the National Science Fund at the Ministry of Education and Science, Republic of Bulgaria, within the project KP-06-H27/16 „Development of Efficient Methods and Algorithms for Tensor-based Processing and Analysis of Multidimensional Images with Application in Interdisciplinary Areas "

References

[1] A. P. James, B. V. Dasarathy, Medical Image Fusion: A survey of the state of the art, Information Fusion, 2014.

[2] M. Nandeesh, M. Meenakshi, "Image Fusion Algorithms for Medical Images-A Comparison", Bonfring International Journal of Advances in Image Processing, vol. 5, no. 3, pp.23-26, 2015

[3] H. Elhoseny, O.Faragallah,"Medical Image Fusion: A Literature Review Present Solutions and Future Directions", Menoufia Journal of Electronic Engineering Research, vol.26, no.2, pp. 321-350, 2017

[4] V. Georgieva, P. Petrov and D. Zlatareva, "Medical image processing based on multidimensional wavelet transforms - Advantages and trends", AIP Conference Proceedings 2333, 020001, https://doi.org/10.1063/5.0041869, 2021

[5] R. Bhandari, B. Shivakumar, "Wavelet based analysis of medical image fusion using MATLAB GUI," International Journal of Innvative Research in Science, Engineering and Technology, vol. 5, pp.512-517, 2016.

[6] T. Kugarajah and Q. Zhang, "Multidimensional wavelet frames," in *IEEE Transactions on Neural Networks*, vol. 6, no. 6, pp. 1552-1556, 1995.

[7] V. M. Georgieva, P. P. Petrov, D. S. Tsvetkova and L. B. Laskov, "MRI/SPECT Image Fusion of Brain Based on Multi-Scale Wavelet Decomposition, "*56th International Scientific Conference on Information, Communication and Energy Systems and Technologies (ICEST)*, pp. 85-88, 2021.

[8] B. Jiang, R.Zhang, X.Zhang, A Comparative Study of Wavelet-Based Image Fusion with a Novel Fusion Rule, *International Journal of Machine Learning and Computing,* Vol. 5, No. 6. 2015.

A HYBRID APPROACH FOR BRAIN TUMOR DETECTION IN MRI IMAGES

Veska Georgieva

Faculty of Telecommunications, Technical University of Sofia, Bulgaria
1000 Sofia, "Kl. Ohridsky" str.8
T. (+359 2) 965-3293; E-mail: vesg@tu-sofia.bg

Veronika Katsarova

Faculty of German Engineering Education and Industrial Management, Technical University of Sofia, Bulgaria
1000 Sofia, "Kl. Ohridsky" str.8
E-mail: veronika.katsarova@fdiba.tu-sofia.bg

Lyubomir Laskov

Faculty of Telecommunications, Technical University of Sofia, Bulgaria
1000 Sofia, "Kl. Ohridsky" str.8
T. (+359 2) 965-3998; E-mail: llaskov@tu-sofia.bg

Abstract

In this paper we present a hybrid approach based on texture analysis and active contour segmentation for the 3 grades of meningiomas. Since the shape of the tumors plays a major role in its classification, we propose to segment the area of the meningioma on the base of the active contour without edges. We use the second-order texture analysis through Gray-Level Co-occurrence Matrices to extract and analyse some texture features, such as contrast, correlation, homogeneity, energy and entropy. The experiments, performed in MATLAB environment with real MRI images of a human brain have shown good results for detection of meningioma in the diagnostic phase, which can help for successfully treatment of this disease.

1. INTRODUCTION

Meningiomas are the most common type of primary brain tumors, which present approximately of 30 % of all brain tumors. It arises from the meninges, the outer three layers of protective tissue located between the skull and the brain [1, 2]. Meningioma can be graded in 3 grads, based on the appearance of the tumor cells under a microscope. Grade I is the most common type of meningioma, it grows slowly and is considered benign. Grad II (atypical meningioma) grows more quickly. Grade III (anaplastic/malignant meningioma) grows and spreads quickly. It is the most aggressive form and is considered malignant [1]. Magnetic resonance imaging (MRI) is preferred technology to diagnose meningioma because it can create more detailed images than CT scans and often shows changes in the brain caused by the tumor, such as swelling or areas where the tumor has grown [3]. Meningiomas are characterized in the MR image by a relatively smooth, regularly appearing border. In many cases the segmentation of brain tumors is a complex task due to tumor shape, size and location that vary greatly across different patients [4, 5]. The presence of noise of different nature in many cases complicates accurate diagnosis [6].

Many methods and approaches have been proposed for detection and classification of different brain tumors in MR images, particularly, fuzzy clustering means (FCM), support vector machine (SVM), artificial neural network (ANN), Deep Learning model (DLM) and expectation-maximization (EM) algorithm technique [7,8,9]. Some of the popular techniques for extracting the important information from images are based on region growing based segmentation [10]. The features extraction approaches can obtain texture characteristics on the base on Local Standard Descriptor (LBP), Grey-Level Co-occurrence Matrices (GLCM) or their modifications [11].

We propose a hybrid approach based on active contour segmentation and texture features analysis to detect the 3 grades of meningioma in MRI images.

The rest of the paper is organized as follows. In section 2, we present the basic stages of the proposed approach. Some results, obtained by the simulation and discussion are introduced in section 3. Finally, conclusion is given in section 4.

2. MAIN STAGES OF PROPOSED APPROACH

The proposed hybrid approach consists of the following main stages:

- Pre-processing
- Meningioma segmentation via active contour and calculation of tumor area
- Texture analysis based on GLCM

2.1. Pre-processing

The complex effect of the influence of some different artefacts in MR images can be presented as kind of noise. MR images are mostly corrupted by Rician noise, which arises from complex Gaussian noise in the original frequency domain measurements [12]. We propose to reduce this noise based on the homomorphic wavelet filter due to the best SNR results for MRI images [6].

2.2. Meningioma segmentation

We propose to apply the active contour model of Chan and Vese for segmentation in individual MR images, as well as in the entire MRI sequence. This model guarantees greater smoothness of the contour and accuracy of segmentation compared to the other known ones. The algorithm for determining the initialization contour (mask) from which the segmentation begins will be the same. But in segmenting the entire sequence, this algorithm will be applied to the image in which the tumor is best seen. From this image we can get a more accurate initial contour for segmentation.

The model is a special case of the Mumford–Shah function. Mumford and Shah approximate the image f by a piecewise-smooth function u as the solution of the minimization problem. Compared to the piecewise constant Mumford - Shah model, the key differences with the Chan - Vese model are an additional term penalizing the enclosed area and a further simplification that u is allowed to have only two values, $c1$, $c2$ are the values of u respectively inside and outside of the boundary of a closed set C [13].

The main idea is to find among all u of this from the one that best approximates f [14]. Now is needed minimization over all set boundaries C. This is made by applying the level set technique introduced by Osher and Sethian, where is used a level set function φ for a circle of radius r. The Dirac function δ, which is the gradient of the Heaviside function, penalizes long boundaries between the regions [14].

The flowchart of the main algorithm for tumor segmentation in the MRI sequence is shown in Fig. 1.

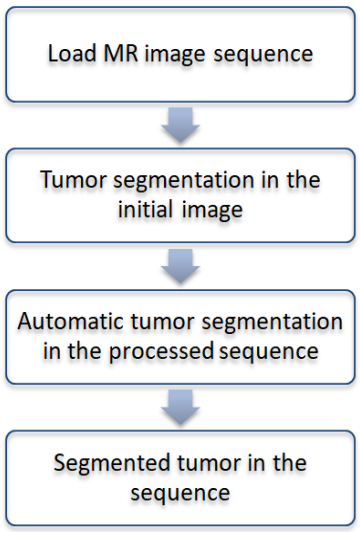

Figure 1. Flowchart of main algorithm for segmentation

For solving this task and to make the initial segmentation of the primary image we choose the following specific parameters for the segmentation [15]:

- *mask* – Initial contour at which the evolution of the segmentation begins;
- *n* – Maximum number of iterations to perform in evolution of the segmentation;
- *R* – Radius of the location in pixels;
- *Alpha* – 'Smooth Factor' — Degree of smoothness or regularity of the boundaries of the segmented regions;

The flowchart of algorithm for creating the initial contour (mask) is given in Fig. 2.

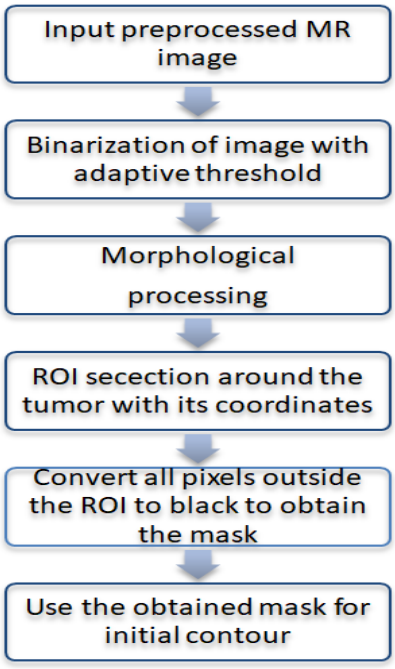

Figure 2. Flowchart of algorithm for creating the initial contour

For binarization the method of Otzu was proposed. After that we use morphological oppening to remove all small objects around the tumor and preserve its shape and size. We choose a disk structure element, therefore, the tumor usually is oval and in determining the correct width, the square ROI can keep the shape of the tumor. Next, the initial contour is obtained. Finally, the segmentation via active contour without edges in the MR image is made. Using this algorithm, we can successfully segment the tumor into single images.

Once the image in which the tumor is best seen has been selected, we propose to segment the sequence in two directions (forward and backward from the original image) to segment all the images in the sequence. That means we can build two loops: one incrementing and other decrementing to craw the array of images with tumor in the sequence. This approach is appropriate, because in the most cases the tumor is getting smaller in these two directions in the sequence. Each subsequent image uses as mask for its segmentation with active contours without edges the result of the segmentation of the previous image [16]. Each image is processed primarily as described above. The segmented meningioma is visualized with yellow contour on the preprocessed images. Finally, the area covered by the tumor can be calculated in pixels using the area of the resulting contour mask.

2.3. Texture analysis based on GLCM

The second-order statistical method that takes into account the spatial relationship of pixels in an image is the Gray-Level Co-Occurrence Matrix (GLCM), also known as the Gray-Level Spatial Dependence Matrix. The functions of the GLCM characterize the texture of the image by calculating how often pairs of pixels with a specific value and in a specific spatial relationship appear in an image. In this way a GLCM is formed and statistical measurements are taken from it [17]. The representation of the image texture is contained in the co-occurrence matrices calculated in four directions, namely, 0^0, 45^0, 90^0, and 135^0. We can extract information about the structure from the examined texture by using texture properties. Fourteen local properties have been suggested by Heralick et al. for this purpose [18].

In our study, we have used some textural characteristics as the most useful such as contrast, correlation, homogeneity, energy, and entropy. Analyzing these texture characteristics, we can conclude about their behavior in the three different grades of meningioma, which is very useful for their early detection.

3. RESULTS AND DISCUSSION

The experiments were performed in MATLAB 9.7 environment. Thirty real digital MRI – T1 images in axial plane of a human brain with the 3 different grades meningioma (10 from each grad) are used for the experiments. The images are from database of Radiopedia [19]. We have used also 3 MRI series of the brain with size 256x256 pixels from the database of Medical University of Sofia.

Some results from our experiment are given in the next figures below. They show the results from segmentation of meningioma in the 3 grades from single MR images.

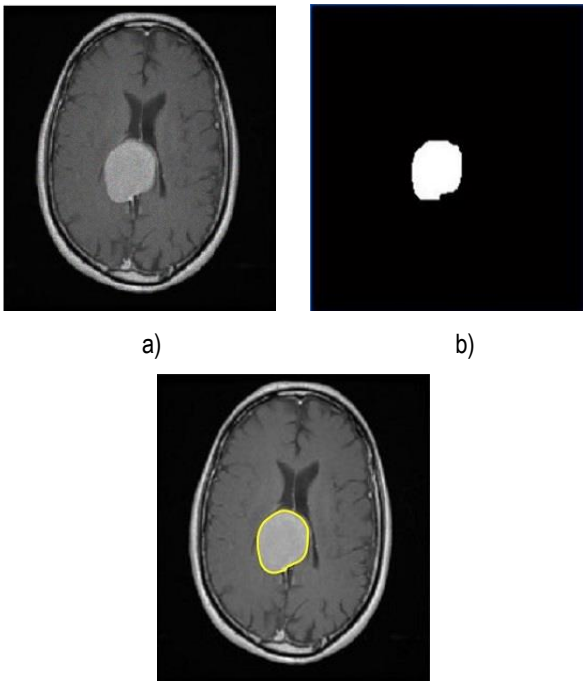

a) b)

c)

Figure 3. MRI image of meningioma grad I:
a) original; b) mask for initial contour
c) segmented image with tumor area 2337 pixels

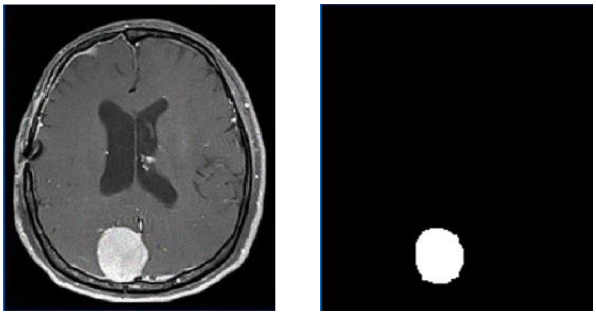

a) b)

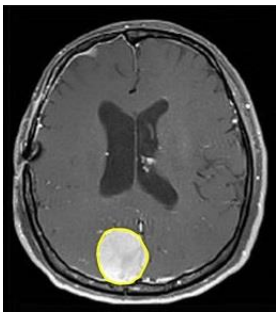

c)

Figure 4. MRI image of meningioma grad II: a) original; b) mask for initial contour c) segmented image with tumor area 2089 pixels

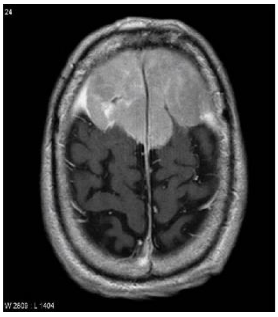

a)

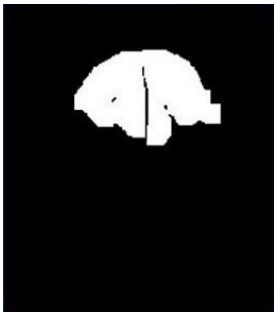

b)

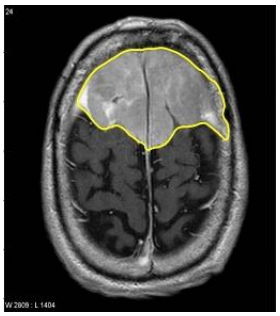

c)

Figure 5. MRI image of meningioma grad III:
a) original; b) mask for initial contour
c) segmented image with tumor area 7977 pixels

The segmented images are obtained by following specific parameters: *n*=50, *R*=10 pixels, smooth factor *alpha*=2.

Some average results of the texture characteristics obtained for the 3 grades of meningioma, are presented in the following tables.

Table 1. Contrast

Angle	Meningioma grad I	Meningioma grad II	Meningioma grad III
0°	0.08	0.1	0.13
45°	0.12	0.18	0.17
90°	0.06	0.12	0.1
135°	0.13	0.17	0.175

Table 2. Correlation

Angle	Meningioma grad I	Meningioma grad II	Meningioma grad III
0°	0.99	0.984	0.987
45°	0.985	0.971	0.984
90°	0.992	0.983	0.992
135°	0.985	0.972	0.984

Table 3. Homogeneity

Angle	Meningioma grad I	Meningioma grad II	Meningioma grad III
0°	0.968	0.96	0.958
45°	0.959	0.948	0.942
90°	0.971	0.96	0.96
135°	0.958	0.947	0.943

Table 4. Energy

Angle	Meningioma grad I	Meningioma grad II	Meningioma grad III
0°	0.28	0.27	0.23
45°	0.27	0.255	0.225
90°	0.28	0.27	0.235
135°	0.27	0.255	0.225

The obtained average results for the entropy are as follows: for grad I is 5.783, for grad II is 6.355 and for grad III is 8.583. This shows that when the difference between the maximum and minimum image intensity is very small, which characterizes cases with a low grades of meningioma, the image has low entropy and low contrast.

The corresponding graphical representation of these characteristics is given in Figure 6, Figure 7, Figure 8 and Figure 9.

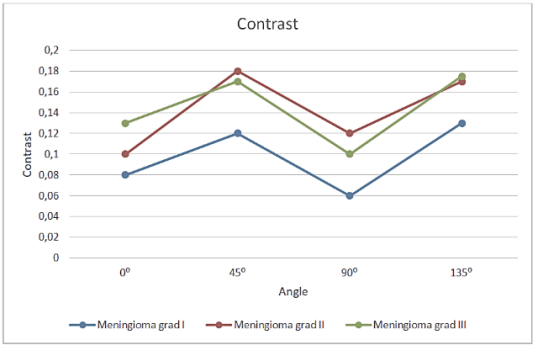

Figure 6. Contrast for the 3 grades of meningioma

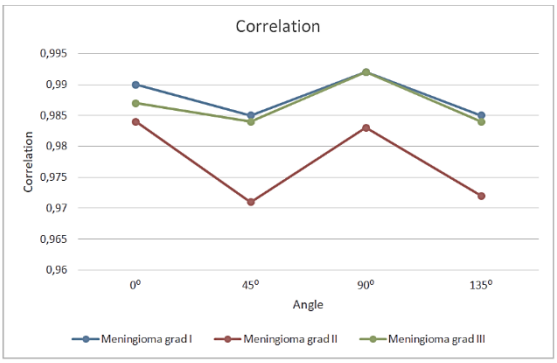

Figure 7. Correlation for the 3 grades of meningioma

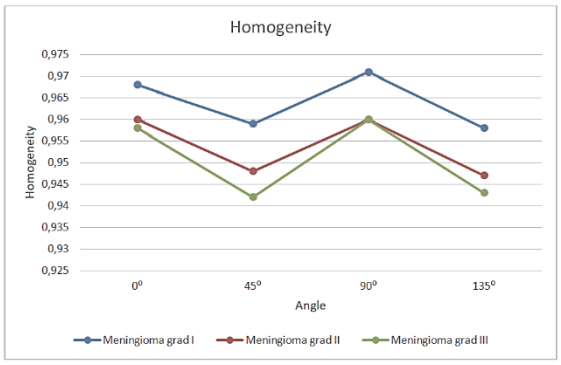

Figure 8. Homogeneity for the 3 grades of meningioma

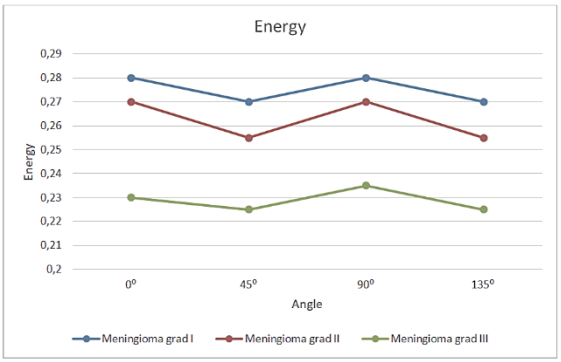

Figure 9. Energy for the 3 grades of meningioma

The obtained results of correlation show how the gray values of the pixel pairs change. If the values are higher than zero, it means that the pixel pairs have roughly similar gray values. All values here are very close to 1, from which it can be determined that there are no dramatic changes in the gray values, but there is a fairly smooth gradient of gray values. But we can find the peaks at the 0^0 and 90^0 angles. This shows that the different gray values gently overflow in these directions. The situation is similar with the homogeneity. If we now look at the images, it is clear that several textures can be distinguished on the images of the meningioma of grade III. Grade I meningioma are characterized by high homogeneity of cell structure. The energy values show that despite being close, the highest energy is in grade I and the lowest in grade III. This is due to the lower homogeneity in the cell structure of the tumor.

4. CONCLUSION

In this paper we present a hybrid approach based on active contour segmentation and texture features analysis to detect the 3 grades of meningioma in MRI images. Our hybrid approach shows the highest Dice coefficient (DSC) for segmenting the tumor (96.2%) in the single images. This is better compared to the active contours without edges (94.5%) and a growing region, or compared to the approach presented in [4], where the Dice coefficient is 90%. It offers the opportunity to detect the different grades of meningioma, not just the classification of grad I and anaplastic. In many clinical cases, the degree is determined only by the area of the tumor, but our study has shown that the application of textural characteristics is crucial in this classification.

Our future work will be related to conducting more experiments in terms of research for series of images, not only in axial plane, as well as combining the proposed approach with other methods such as DLM for automatic classification of the individual grades of meningioma.

5. ACKNOWLEDGMENTS

This work was supported by the National Science Fund at the Ministry of Education and Science, Republic of Bulgaria, within the project KP-06-India-04 "Contemporary Approaches for Processing and Analysis of Multidimensional Signals in Telecommunications".

References

[1] American Brain Tumor Association. https://www.abta.org/tumor_types/meningioma

[2] American Society of Clinical Oncology. https://www.cancer.net/cancer-types/meningioma

[3] https://www.hopkinsmedicine.org/health/

[4] M. Agn., O.Puonti, P.Rosenschöld, I. Law, K. Van Leemput, (2016) "Brain Tumor Segmentation Using a Generative Model with an RBM Prior on Tumor Shape". In: Crimi A., Menze B., Maier O., Reyes M., Handels H. (eds) Brainlesion: Glioma, Multiple Sclerosis, Stroke and Traumatic Brain Injuries. BrainLes 2015. Lecture Notes in Computer Science, vol 9556. Springer, Cham. https://doi.org/10.1007/978-3-319-30858-6_15

[5] T. Haeck, M. Frederik, P. Suetens. "Automated model-based segmentation of brain tumors in MR images." Proceedings BraTS Challenge, 2015, pp.25-28.

[6] A. Mihaylova, V.Georgieva, "Comparative analysis of Various Filters for Noise Reduction in MRI Abdominal Images", *International Journal "Information Technologies & Knowledge"* Volume 10, Number 1, Page 47-66, 2016.

[7] M. Alfonse and A.-B. M. Salem, "An automatic classification of brain tumors through MRI using support vector machine," Egyptian Computer Science Journal, vol. 40, pp. 11–21, 2016.

[8] S. Damodharan and D. Raghavan, "Combining tissue segmentation and neural network for brain tumor detection," International Arab Journal of Information Technology, vol. 12, no. 1, pp. 42–52, 2015.

[9] K.Laukamp, F.Thiele, G., Shakirin,. *et al.* "Fully automated detection and segmentation of meningiomas using deep learning on routine multiparametric MRI". *Eur Radiol* 29**,** pp.124–132, 2019.

[10] C.Sheela, G.Suganthi, "Morphological edge detection and brain tumor segmentation in Magnetic Resonance (MR) images based on region growing and performance evaluation of modified Fuzzy C-Means (FCM) algorithm"", Multimed Tools Appl. 79, pp. 17483–17496, 2020.

[11] J.Amin, M.Sharif, M. Raza, T.Saba, M.Anjum, "Brain tumor detection using statistical and machine learning method," Computer Methods and Programs in Biomedicine-Elsevier,pp. 69-79, 2019.

[12] L. He and I. R. Greenshields, "A Nonlocal Maximum Likelihood Estimation Method for Rician Noise Reduction in MR Images," in *IEEE Transactions on Medical Imaging*, vol. 28, no. 2, pp. 165-172, Feb. 2009.

[13] P.Getreuer, Chan and Vese Segmentation, In: Image Processing On Line, IPOL 2012-08-08, Yale University, pp. 214-224.2012.

[14] K. D. Toennies, Guide to Medical Image Analysis, Methods and Algorithms, Springer 2012.

[15] V.Georgieva, S.Ermakov, "GUI for CT Image Segmentation via Active Contours", *IEEE 4th International Black Sea Conference on Communications and Networking (BlackSeaCom)*, pp.1-5, 2016.

[16] A.Mihaylova, V.Georgieva, "Spleen segmentation in MRI sequence images using template matching and active contours", Procedia Computer Science, Elsevier, 131, pp. 15–22, 2018.

[17] B.Varghese, St.Cen, D.Hwang, V. Duddalar, "Texture Analysis of Imaging: What Radiologists need to know", American Journal of Roentgenology. pp. 520-528, 2019.

[18] R. M. Haralick, K. Shanmugam and I. Dinstein, "Textural Features for Image Classification," in *IEEE Transactions on Systems, Man, and Cybernetics*, vol. SMC-3, no. 6, pp. 610-621, 1973.

[19] Radiopedia (o.J.): "Meningioma", URL: https://radiopaedia.org/articles/meningioma

CYBERSECURITY OF INFORMATION IN SPACE TELEMEDICINE

Evgeni Andreev[1], Veselka Radeva[2], Mariya Nikolova[3],

N. Y. Vaptsarov NAVAL ACADEMY
73 V. Drumev St., Varna 9026, BULGARIA

E-mail: e.andreev@naval-acad.bg[1]; veselka.radeva@gmail.com[2]; mpn@abv.bg[3]

Abstract

The article presents the main guidelines and requirements for space telemedicine, which should ensure the health and safety of future space tourists and spacecraft pilots. The existing ways of transmitting medical information from the International Space Station are considered. It is proposed to create special telemedicine centers for future medical centers at space airports.

The article discusses the main medical conditions and their parameters that must be monitored during space flight. This information is consistent with the small time interval of space flights for space tourists. According to the existing technical standard for the protection of space data transmission systems, a prototype of a communication protocol for data transmission has been developed. Personal and medical data are obtained from a suit specially equipped with medical sensors and transmitted to the medical center at the space-port. The advantages of the prototype protocol, which are in the field of data protection and compression, are presented. It is proposed that in order to increase the security of the data, their transmission must take place via encrypted channel.

1. INTRODUCTION

On July 11, 2021, the first space tourists successfully took off with a spacecraft of the private space agency Virgin Galaxy. Other private space agencies will also operate space tourism flights [5]. The development of a new sector in the world economy has already begun. Spacecraft with space tourists will be launched from specially created space airports or transformed airports from military and civil aviation. An interesting trend is the extended age limit of future space tourists - from 16 to 70 years. This determines the great role of space medical centers – an important area of any space airport. The selection of future space tourists and monitoring of their health during the flight will be carried out. These medical centers will monitor and control the health of the crews of the spacecraft before, during and after the flights [9].

A team of teachers and students from Naval Academy is developing a project "Space Medical Center", presented at the ESA Aerospace student challenge competition in 2019 [2]. We propose to establish telemedicine laboratories in the future space medical centers. It is extremely important to ensure secure, stable protection of personal and medical data of the crew and space tourists.

2. SPACE AIRPORTS AND MEDICAL CENTERS FOR SPACE TOURISTS

Sir Richard Branson and Virgin Galactic set the stage for space tourism. Interest in space travel is growing as many people make deposits to book their "flights"; revenues from commercial space flights are increasing and capital investment from private sources is expanding [5].

Space tourism is an area that is soon expected to be a multimillion dollar industry. Space tourism will continue to expand, and will become increasingly affordable. The implementation of this huge expansion will depend to a large extent on the security of all systems, including those in the medical sector. A process is underway to turn military and civilian airports, rocket launchers into space airports. We propose that the main areas in a space airport are: terminal, horizontal runway and vertical runway, control tower and flight control area, medical area, production area, fuel storage and fire safety area [2] Crews and tourists will be trained in special gyms under the supervision of space medicine specialists. During the flight, the health of each tourist will be monitored by sensors in the suit of each of them. If medical intervention is required, instructions will be given through direct contact with specialists from the Telemedicine Center at the Space Medical Center. After returning to Earth, the crew and tourists will undergo mandatory examinations and receive instructions for possible post-flight health problems [7]. Conceptual design of a medical center for space tourists is shown in Figure 1.

It is of utmost importance the preliminary selection of people who will have the unique opportunity to fly in space as tourists. This selection will be accomplished due to a special, unified pre-selection system

for candidates located in a medical online site of the Space Center. This way, everyone who is willing will be able to submit the necessary data and receive an answer in the shortest possible time whether it meets the basic requirements for space travelers. Pre-selection is of paramount importance, as it saves a lot of time and energy, both from the choice of medical professionals and from the space tourist.

Figure 1. Conceptual design of a Space Medical Center

It is of utmost importance the preliminary selection of people who will have the unique opportunity to fly in space as tourists. This selection will be accomplished due to a special, unified pre-selection system for candidates located in a medical online site of the Space Center. This way, everyone who is willing will be able to submit the necessary data and receive an answer in the shortest possible time whether it meets the basic requirements for space travelers. Pre-selection is of paramount importance, as it saves a lot of time and energy, both from the choice of medical professionals and from the space tourist.

The poll will be available on a specially developed web site. After completing it, in the database of Space Medical Center for future space tourists, the following information will be included: personal data, weight, height, Body Mass Index, cardio and brain diseases, cerebrovascular, respiratory accidents, problems of the digestive system, genetic anomalies, oncology illness, chronic diseases of muscles, joints and / or bones, traveling often by airplane etc.

Occasionally available medical specialists are not enough to build a multidisciplinary patient review. It is important because you may find movement in one of the indicators during the diagnostic process. For this reason, the medical center must provide the unique opportunity to build online connections with the best medical professionals from all over the world, conduct research and review of candidates Telemedicine is an important part of the overall scientific work of the center and its employees.

3. BASIC GUIDELINES AND REQUIREMENTS FOR SPACE MEDICINE

A very accurate idea of human factors and their relationships in space medicine is given by the diagram shown in Figure 2. It is based on the SHELL model [7].

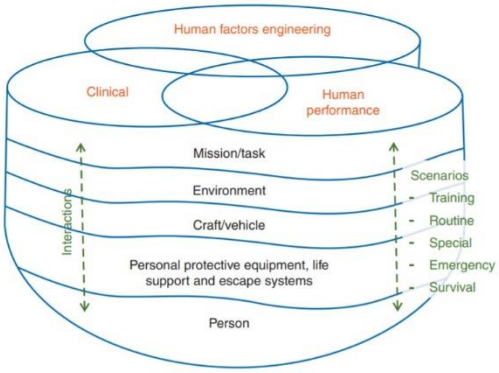

Figure 2. Model of factors and relationships in space medicine [7]

The SHELL abbreviation stands for: Software (e.g. standard operating procedures), Hardware (e.g. equipment, systems, vehicles), Environment, Liveware (individual) and Liveware (other people). The SHELL model demonstrates the importance of interfaces and interactions between different components of a spacecraft system.

Space flight refers to those trips that take place at more than 100 km above sea level. This internationally recognized altitude limit is known as the Karman line. There are three categories of human spaceflight: 1) suborbital, 2) low Earth orbit (LEO; eg, the International Space Station), and 3) exploration-class missions (eg, missions to the moon and Mars). Space tourists will participate in suborbital space flights. They are short and usually last no more than a few hours, of which only a few minutes are spent in a state of weightlessness. The flights involve exposing the human body to increased acceleration in the vertical (Gz) and horizontal (front to back; Gx) planes, which may affect the cardiorespiratory system. The degree of acceleration tested usually refers to the acceleration due to gravity near the Earth's surface. The cockpit pressures are likely to be equivalent to commercial aircraft cabins (6-8,000 feet above sea level). The low Earth orbit suggests spacecraft in orbit around the Earth at an altitude of 200-400 km.

4. MEDICAL CONTROL DURING FLIGHT

Human spaceflight takes place in a rigorous, remote, and physiologically challenging environment with medical provision severely limited by considerations of power, weight and volume and crew skills. In addition, it is an environment in which it is possible for a person with an important role in the mission to endanger the health and safety of the entire crew due to a medical problem. The most successful method of mitigating the significant physiological risks posed by spaceflight lies in adequate screening prevention. Therefore, medical standards in space flight play an important role. Their purpose is to know all existing medical conditions that could endanger the safety of the crew and the objectives of the mission. [4]

The standards are stricter for astronauts than for professional astropilots. However, all are monitored for health problems that can cause disability (eg, coronary artery disease, kidney stones, epilepsy). It should be borne in mind that poor health can be further exacerbated by interactions with the space environment or life support systems (eg, bullous lung disease or asthma). Special medical standards will be observed in the situation of a tourist space flight to a "space tourist". The Aerospace Medical Association (AsMA) publishes medical guidelines [7] for space travelers who are older and show more health problems. Preliminary studies of potential future space tourists have been conducted to understand possible tolerance to health requirements. Potential space tourists with well-controlled medical conditions will be allowed to fly. Medical standards will continue to change through future surveys of space tourists in combination with data on medical incidents from flights with an increase in the number of space tourists.

5. PROTOTYPE OF A COMMUNICATION PROTOCOL FOR THE TRANSMISSION OF MEDICAL SPACE DATA

Medical information data is transmitted after encapsulation by the prototype protocol via TCP (Transmission Control Protocol).

5.1. Concept for protection of space communication

Hacking satellite communication is not an easy task. We can talk about the possibility of potential attacks that may or may not happen at the moment. The attacks that are generally used are the so-called Spoofing or Jamming attacks. Their purpose is to deceive the systems or make them stop working altogether. Electronic warfare is a method used to stop the uplink signal to satellites sent from Earth, as well as to limit the signal received from the satellite. In this way, a false spoofing uplink signal can be sent to try to trick the satellite into executing commands by the attacking hacker. In this way, the data sent by the satellite, such as GPS coordinates with a GPS Spoofing attack, can be manipulated. This will affect GPS users. Some good practices show that we should never trust a single source, if GPS does not send accurate information we should look for alternative ways of positioning. According to the Consultative Committee for Space Data Systems, the most common space cyber attacks are: altering the transmitted data, restricting the ability to transmit data, manipulating the sender and recipient, sending incorrect data and unauthorized access to spacecraft. To prevent this type of attack, it is good practice to use an encrypted access channel from point A to point B, most often through a tunnel - VPN. The authorization should be two-factor, and the data should be encrypted and not sent in clear text. To this end, a communication protocol must be established that meets all the requirements for the protection of communication between earth stations and satellites [1, 8].

5.2. Preliminary protocol for secure communication

We propose that the secure communication protocol consists of the following fields, shown at the figure 3:

- Message type – shows the priority and seriousness of the message. For example – urgently, with normal priority, daily and informative.
- Message sender – contains information about the author of the message.
- Message Receiver – possible variants of the recorded information are: a specific doctor, a group of doctors or to all doctors.
- Message – includes a short text and / or image of the patient's symptoms
- Checksum for the integrity and authorization - ensuring that only the actual recipient will receive and be able to read the message.

The information is first converted to a binary number system and then sent. The structure of the fields that make up the protocol are presented as follows:

- The first 3 bits of the protocol allow for 8 different types of message, and in the first version only the first 2 bits are used, which allow for 4 records.
- The next 5 bits indicate who is the sender, 2 of the 5 options are provided, as the first revision of the protocol, which for the subject activity of the protocol should be sufficient.
- The next 5 bits are divided into 2 parts for the attending physician (s). The first two bits indicate whether the message should be sent to one or more doctors. As if the value is 01 - specific doctor, if it is 10 to several doctors, 11 to all and 00 initial value without recipient. After choosing the type, individual individuals or groups of doctors are specified in 3 bits.
- The message size can include up to 5000 bits. For greater protection of the information in it, it is not transmitted in its pure form, but is converted to base64 format [6]

Message Type	Message Sender	Message Receiver	Message	Checksum
3 bits	5 bits	5 bits	5000 bits	

Figure 3. Conceptual version of the structure of protocol for secure communication

5.3. Advantages of the protocol

The reduced type of data transmitted in two main data types are one of the main advantages of the protocol prototype.

The data types are limited to the bit representation of the main components of the protocol. The text information is converted to base64.

The data is transmitted through a VPN tunnel for additional protection.

6. CONCLUSION

Space telemedicine is a key component of the medical care of future space tourists. Space telemedicine provides preventive, diagnostic and therapeutic assistance during the flight and allows seamless continuity of care before and after space tourist flights. Cybersecurity and a secure data transmission protocol are required for the seamless transmission of medical information from the spacecraft to Earth.

References

[1] B. Unal, Cybersecurity of NATO's Space-based Strategic Assets, The Royal Institute of International Affairs, 2019.

[2] ESA Aerospace student challenge competition in 2019, http://www.studentaerospacechallenge.eu/index.php/en

[3] G. Falco, "Cyber Security Project. Job One for Space Force: Space Asset Cybersecurity, Cyber Security Project", Belfer Center for Science and International Affairs| Harvard Kennedy School, 2018, http://osa-public.s3.amazonaws.com/papers/csp_falco_space_asset-final.pdf

[4] HL7 Fast Healthcare Interoperability Resources, Release 4, http://www.hl7.org/implement/standards/product_brief.cfm?product_id=491

[5] J. Bachman, Virgin Galactic pull off key test for Space Tourism, Bloomberg, July, 2021

[6] Lossless Data Compression, Recommended Standard CCSDS 121.0-B-3, https://public.ccsds.org/Pubs/121x0b3.pdf, 2020

[7] P. Hodkinson, R. Anderton, B. Rosselt, K. Fongq An overview of space medicine British Journal of Anaesthesia, 119,2017

[8] R. Slywczak, Low-Earth-Orbit Satellite Internet Protocol. Communications Concept and Design, Glenn Research Center, Cleveland, Ohio, 2004, https://ntrs.nasa.gov/api/citations/20040045319/downloads/20040045319.pdf

[9] S. Tkachova, Emerging Space Markets, Springer-Verlag Berlin Heidelberg, 2018

OBJECTS TRACKING FROM VIDEO IN URBAN ENVIRONMENT BY LOW RANK RECOVERY

Ivo R. Draganov, Rumen P. Mironov

Radiocommunications and Videotechnologies Dept.
Faculty of Telecommunications, Technical University of Sofia
8 Kliment Ohridski Blvd., 1756 Sofia, Bulgaria

e-mail: {idraganov, rmironov}@tu-sofia.bg

Abstract

In this paper a novel scheme is presented for objects tracking in urban environment from a video, represented as three-way tensor. The low rank recovery (LRR) method is applied in 4 of its variations – the Robust Orthogonal Subspace Learning (ROSL), the Fast Linearized Alternating Direction Method with Adaptive Penalty (FastLADMAP), the Inexact Augmented Lagrange Multiplier (IALM), and the Linearized ADM with Adaptive Penalty (LADMAP). Two fusion functions are proposed for combining binary segmented frames from the top two performing decompositions – LRR FastLADMAP and ROSL, to get higher detection rate for foreground objects. The proposed approach is considered applicable in fields like video surveillance, production automation, public entertainment, etc.

1. INTRODUCTION

Moving objects detection on a frame-by-frame basis in video plays important role in numerous applications, such as video surveillance, vehicle traffic control, industrial production, logistics and many others. Detecting the boundaries of foreground objects over a complex background as accurately as possible over time is the first step towards further efficient analysis of the scene. Many methods rely on representing the input video as three-way tensor, which is being further decomposed under various schemes to sparse and low-rank components, which further analysis lead, in some of the applications, to detection of the moving objects – a hard task, when the background is complex.

In [1] Shijila B. et al. use low rank approximation as a mean for denoising and in parallel to it, moving objects detection in videos. They apply the l_1-Total Variation (TV) regularization approach and try to consolidate it with the nuclear norm, and the l_2-norm in a single framework. F1-measure of the detection process has been reported to vary between 0.98 and 0.99 over videos with Gaussian noise. The same authors had proposed another technique, using TVRPCA with a convex optimization, where the convergence of the resulting algorithm is being tried [2]. Reduced computational complexity is reported, compared to TVRPCA, DECOLOR and other algorithms, while the F1-measure changes between 0.52 and 0.90 among 6 test videos, comprising of various elements, including camera jitter, shadows, dynamic background, etc.

Yang et al. [3], following the basic idea of approximation based on rank functions and sparse conditions, try to find different mean than the nuclear norm. The authors propose nonconvex function, using Generalized Singular Value Thresholding (GSVT) and Alternating Direction Method of Multipliers (ADMM). The proposed approach appears effective in noise suppression, leading to Peak Signal to Noise Ratio (PSNR) of filtered frames between 35.2 and 39.4 dB. The F-measure of the object detection process changes between 0.3969 and 0.9153 for a set of 7 test videos, which proves its general applicability.

Matrix recovery with a low rank and using weights through a spectral graph is the approach, developed by Chen et al. [4], to detect salient objects. Both the low-rank and sparse matrices are employed in the process. The average F-measure deviates between 0.5678 and 0.8437 from testing with 4 datasets.

Sobral, in his thesis [5], looks towards both the matrix and tensor decomposition to low-rank and sparse components for object detection in video and other applications. Double-constrained version of the RPCA algorithm is developed for enhanced foreground detection. Spatial saliency maps ease the process in the case of dynamic scenes. Additionally, two decomposition algorithms, based on tensor representation and incrementally organized help to separate better the foreground from the background in multidimensional data. The F-measure reaches 85.96% for a RGB test sequence and 95.17% for a multispectral one for one of the implementations, following this approach.

Wang and Huang [6] use the $l_{2,1}$-norm minimization, while performing the low-rank approximation. The approach is applied over a set of multi-scale features, incorporating color, shape, texture, and other descriptors. All three parameters – Precision, Recall and F-measure reach values close to 0.9 during experimentation with MSRA10K dataset. More recently, Yang et al. [7] propose matrix recovery, based on spatiotemporal representation, in which approach the scalability is one of the imposed properties. The movement of objects in the video is detected by the optical flow algorithm and further the background is eliminated by low-rank regularization with consequent affine transform for suppressing its slight variation (motion) over time. PSNR in background recovery reaches 40 dB and SSIM – 0.9939 in some instances. The average F-measure in detecting foreground objects is 0.87, higher than numerous other decomposition methods. Low-rank tensor representation of videos is employed in their decomposition along with fused-sparse representation of salient type [8]. Three-way tensors assure preservation of the spatial and time relations among objects on a continuous basis over time. Three-dimensional local adaptive regression kernel (3D-LARK) redounds for finding the movement saliency on both the space and time independent coordinates in relation to the foreground. Salient objects are also being detected with a weighted matrix recovery process, where the table arrangement of data has a low rank [9]. Color, mutual location, and contour connectivity are some of the properties embedded in that representation to find the regions, classified as part of the background. Positive results are reported after comparing the algorithm efficiency with other 24 implementations in the practice. Structured sparse outliers [10] are another view over the moving objects in video, which is employed in the low-rank and sparse decompositions. Shkeri and Zhang propose with addition to that view the prior map, which assists in the reduction of the negative effect of significant illumination changes in the scene. F-measure of the background subtraction from testing with popular datasets reaches 0.8033 in some instances.

In this study the main aim is to evaluate the Low Rank Recovery (LRR) method in 4 of its base implementations - the Robust Orthogonal Subspace Learning (ROSL), the Fast Linearized Alternating Direction Method with Adaptive Penalty (FastLADMAP), the Inexact Augmented Lagrange Multiplier (IALM), and the Linearized ADM with Adaptive Penalty (LADMAP) over a popular video test set. Based on the obtained results two new fusion schemes are proposed and tested, which yield higher Detection Rate in one instance and higher Precision in the other. In Section 2 of the paper, the description of the algorithms is given, followed by experimental results in Section 3 and discussion in Section 4. Section 5 contains the conclusion.

2. ALGORITHMS DESCRIPTION

2.1. LRR IALM

In the base of the LRR IALM algorithm lays the matrix completion task. It has been proven that for a matrix A of rank r (typically a low one), having some missing elements, the following optimization procedure may lead to its restoration [11]:

$$\min_A \|A\|_*, given\ A_{ij} = D_{ij}, \forall (i,j) \epsilon \Omega, \quad (1)$$

where Ω is the entity of samples' indices, D – an input matrix of real noisy elements, mxn in number. The exact Augmented Lagrange Multiplier (ALM) method could be applied in this case, following [11]:

$$\min_A \|A\|_*, \quad given\ A + E = D, \quad \pi_\Omega(E) = 0, \quad (2)$$

where π_Ω is a transformation that puts all elements, falling outside Ω to be 0; E – matrix of the additive errors. The partial augmented Lagrangian function with the multiplier Y in it, then, could be found from [11]:

$$L(A,E,Y,\mu) = \|A\|_* + \langle Y, D - A - E \rangle + \frac{\mu}{2}\|D - A - E\|_F^2, \quad (3)$$

where $\mu > 0$ is a scalar, and F denotes the Frobenius norm. Depending on the constraints imposed over the values of $\pi_\Omega(E)$, the IALM algorithm takes its form.

2.2. LRR LADMAP

The linearized ADM could be expressed as [12]:

$$\boldsymbol{x}_{k+1} = arg\min_{\boldsymbol{x}} f(\boldsymbol{x}) + \frac{\beta}{2}\|\boldsymbol{\mathcal{A}}(\boldsymbol{x}) + \boldsymbol{\mathcal{B}}(\boldsymbol{y}_k) - \boldsymbol{c} + \lambda_k/\beta\|^2, \quad (4)$$

where $\boldsymbol{x}$ (typically, the noisy input), $\boldsymbol{y}$ and $\boldsymbol{c}$ are matrices (could be also vectors, which is not of interest to this study, since processing is done over video frames), f – a convex function, λ – Lagrange multiplier, β – penalty parameter, k – the number of the current iteration, and $\boldsymbol{\mathcal{A}}$ and $\boldsymbol{\mathcal{B}}$ – linear transformations. Equation (4) could be approximated as [12]:

$$\boldsymbol{x}_{k+1} = \underset{\boldsymbol{x}}{\operatorname{argmin}} f(\boldsymbol{x}) + \frac{\beta\eta_A}{2}\left\|\boldsymbol{x} - \boldsymbol{x}_k + \boldsymbol{\mathcal{A}}^*\left(\lambda_k + \beta(\boldsymbol{\mathcal{A}}(\boldsymbol{x}_k) + \boldsymbol{\mathcal{B}}(\boldsymbol{y}_k) - \boldsymbol{c})\right)/(\beta\eta_A)\right\|^2, \quad (5)$$

where $\boldsymbol{\mathcal{A}}^*$ is the adjoint of $\boldsymbol{\mathcal{A}}$, η_A – scaling parameter with positive value. The adaptive penalty could be found by updating process, according to [12]:

$$\beta_{k+1} = \min(\beta_{max}, \rho\beta_k) \quad (6)$$

with ρ – a scalar, greater or equal to 1, found separately.

2.3. LRR FastLADMAP

The LRR solution to the problem, posed in Section 2.2, could be found approximately following the criterion [12]:

$$\min_{\boldsymbol{Z},\boldsymbol{E}} \beta\left(\|\boldsymbol{Z}\|_* + \mu\|\boldsymbol{E}\|_{2,1}\right) + \frac{1}{2}\|\boldsymbol{X} - \boldsymbol{X}\boldsymbol{R} - \boldsymbol{E}\|^2, \quad (7)$$

where β is relaxation parameter with a non-negative value, $\boldsymbol{Z}$ – coefficient matrix, $\boldsymbol{R}$ – an additional matrix. Gradual decrease of β could be achieved by [12]:

$$\beta_{k+1} = \max(\beta_{min}, \theta\beta_k), \quad (8)$$

where θ is a constant.

2.4. LRR ROSL

Following the general case of RPCA recovering of a low-rank matrix A, given input matrix X with noise [13]:

$$\min_{A,E}\|A\|_* + \lambda\|E\|_1, given\ A + E = X, \quad (9)$$

where $\|.\|_*$ is the nuclear norm and $\|.\|_1$ – the l_1-norm. It has been proven that [13]:

$$\|A\|_* = \min_{D,\alpha}\frac{1}{2}\left(\|D\|_F^2 + \|\alpha\|_F^2\right), given\ A = D\alpha, \quad (10)$$

$$\|A\|_* = \|\alpha\|_{row-1}, given\ A = D\alpha, D^TD = I_k, \quad (11)$$

where D is a spanning matrix of the ordinary orthonormal space the data is being present, α – vector of coefficients, revealing the influence degree of the components of D, and I – the identity matrix. From (10) and (11) it has been shown that the low-rank recovery by the ROSL algorithm could be accomplished by solving [13]:

$$\min_{E,D,\alpha}\|\alpha\|_{row-1} + \lambda\|E\|_1, given\ D\alpha + E = X, D^TD = I_k, \forall i. \quad (12)$$

2.5. Fusion OR and AND

In order to get higher Detection Rate over the pixels of moving objects the logical operation OR is performed between the binary frames, obtained from the LRR decomposition algorithms. The result is another binary frame. For the purposes of getting higher Precision, the logical operation AND is performed in analogous way. It is expected to have, in this second case, finer detection of the boundaries of moving objects, which are more contrast to the background with less False Positives.

3. EXPERIMENTAL RESULTS

The hardware platform, used for testing, consists of 64-bit Intel Core i5 processor with 4 cores, working on a base frequency of 3.1 GHz, along with 12 GB of RAM and 2 TB 7200 rpm HDD. It is controlled by Ubuntu 14.04 LTS operating system, and all tests are implemented in the Matlab R2016a simulation environment. All decompositions are based on implementations from the LRS Library v. 1.0.10 [14]. The video dataset contains 6 24-bit color videos, captured in urban environment (in- and outdoor with at least 1 person or a vehicle moving over complex background), some of which with changing illumination conditions (Table 1). They are derived from the LASIESTA database [15], in which every video has its groundtruth correspondent (binary) video.

Table 1. Video dataset for testing

Video	Width, px	Height, px	FPS	Frames
I_IL_01	352	288	10	300
O_CL_01	352	288	10	250
I_OC_02	352	288	10	300
I_SI_01	352	288	10	220
O_RA_02	352	288	10	370
O_SU_02	352	288	10	400

The following parameters are measured on a pixel basis along all frames from a video:

$$DR = TP/(TP+FN), \quad (13)$$

$$Precision = TP/(TP+FP), \quad (14)$$

$$F = 2DR.Precision/(DR+Precision), \quad (15)$$

where TP is the True Positive value, expressing the count of pixels correctly discovered as part of a moving object, FN – False Negatives – the count of pixels, belonging to moving objects, but marked as part of the background, and FP – False Positives – all pixels, labeled as part of moving objects, but being

part of the background. Processing time (*PT*) of just applying the decomposition and Full time (*FT*), including input-output operations, are also measured. They are shown in Fig. 1 and the average *DT*, *Precision* and *F* measure – in Fig. 2.

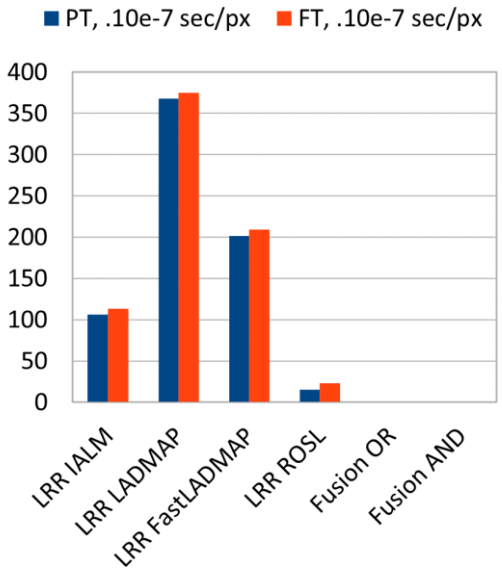

Fig. 1. Processing and Full times of the decomposition schemes

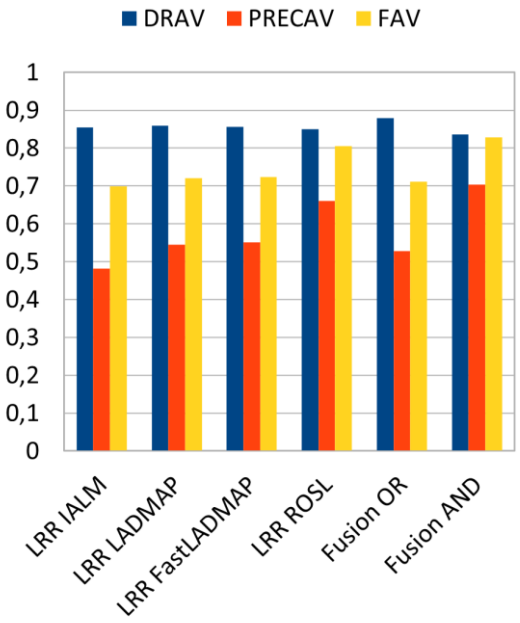

Fig. 2. Detection Rate, Precision and F measure of tested algorithms

The deviations of the same, accuracy defining parameters, are visible in Fig. 3.

Sample processed frames from the two most accurate decompositions and the newly proposed two fusion algorithms are included in Fig. 4.

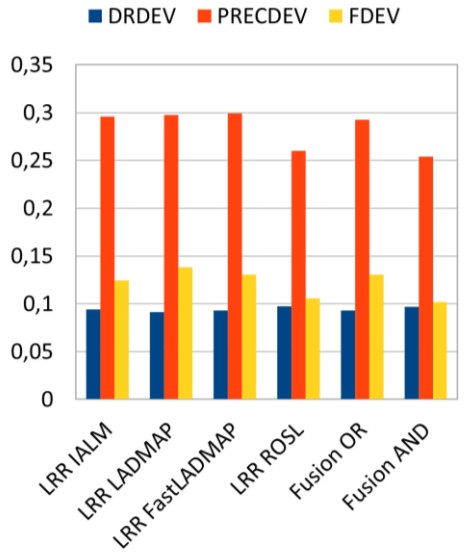

Fig. 3. Deviations of the Detection Rate, Precision and F measure

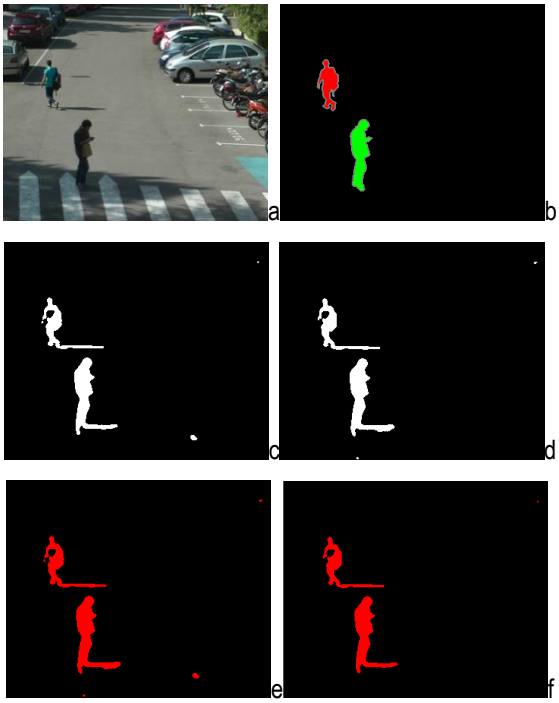

Fig. 4. Frame 257 from the O_SU_02 video: a – original, b – groundtruth, c – FastLADMAP, d – ROSL, e – Fusion OR, f – Fusion AND

4. DISCUSSION

The fastest algorithm is LRR ROSL with *PT* = $15.46.10^{-7}$ sec/px, almost 24 times faster than the slowest LRR LADMAP (Fig. 1). Fusion OR and Fusion AND take $0.58.10^{-7}$ and $0.42.10^{-7}$ sec/px, respectively. These times, although much smaller than the *PT* of all decompositions, are not negligible and should be taken into consideration.

Based on the achieved *F* measures, the most accurate single decomposition implementation is the LRR

ROSL (0.8050), followed by the LRR FastLADMAP with 0.7244 (Fig. 2). There is no significant difference in deviation of accuracy parameters among all tested implementations (Fig. 3).

Fusion OR over the ROSL and FastLADMAP leads to higher *DR* = 0.8791 than any of the four basic decompositions (Fig. 2). Fusion AND on the other hand yield higher *Precision* = 0,7040 – 1.07 times higher than the ROSL, turning out to be the most precise single algorithm (Fig. 2).

At visual inspection of the processed videos, it could be observed that the LRR basic decomposition algorithms produce in some of the cases spots within the binary frames, which are not part of a moving object, but are appearing artefact from the video compression or present noise. In some cases, such spots are result of slight movement of an object, which casts shadow over the visible portion in the frame. The higher the *DR* is, the more of these spots may appear. Examples for such False Positives are seen in Fig. 4 c and d in the lower and top-right area of the frame. Applying the Fusion OR do not remove them (Fig. 4 e), but the Fusion AND does – Fig. 4 f. In general, there is a reduction in the *DR* for the Fusion AND algorithm but getting higher *Precision* for the detection process. Another inconsistency is the appearance of holes in moving objects – at uneven illumination, for example due to reflected light (Fig. 4 a, c-f).

5. CONCLUSION

In this paper, 4 single LRR decomposition algorithms are tested over videos with varying conditions for detection of moving objects – the IALM, LADMAP, FastLADMAP, and the ROSL. Resulting frames from two of the most accurate – the FastLADMAP and ROSL are being passed to a fusion process – once with the logical OR operator and once – with the AND. Higher detection rate is the result in the first case with lower precision and the opposite in the second case. Both fusion schemes are considered applicable in numerous systems, employing video analysis, e.g., video surveillance, vehicle traffic control, automated production, etc.

ACKNOWLEDGEMENT

This work was supported by the National Science Fund at the Ministry of Education and Science, Republic of Bulgaria, within the project KP-06-H27/16 „Development of efficient methods and algorithms for tensor-based processing and analysis of multidimensional images with application in interdisciplinary areas “.

References

[1] Shijila, B., Tom, A. J., & George, S. N. (2019). Simultaneous denoising and moving object detection using low rank approximation. Future Generation Computer Systems, 90, 198-210.

[2] Shijila, B., Tom, A. J., & George, S. N. (2018). Moving object detection by low rank approximation and l1-TV regularization on RPCA framework. Journal of Visual Communication and Image Representation, 56, 188-200.

[3] Yang, Z., Fan, L., Yang, Y., Yang, Z., & Gui, G. (2019). Generalized singular value thresholding operator based nonconvex low-rank and sparse decomposition for moving object detection. Journal of the Franklin Institute, 356(16), 10138-10154.

[4] Chen, J., Chen, J., Ling, H., Cao, H., Sun, W., Fan, Y., & Wu, W. (2018). Salient object detection via spectral graph weighted low rank matrix recovery. Journal of Visual Communication and Image Representation, 50, 270-279.

[5] Sobral, A. C. (2017). Robust low-rank and sparse decomposition for moving object detection: from matrices to tensors (Doctoral dissertation, Université de La Rochelle).

[6] Wang, S., & Huang, A. (2017). Salient object detection with low-rank approximation and ℓ2, 1-norm minimization. Image and Vision Computing, 57, 67-77.

[7] Yang, J., Shi, W., Yue, H., Li, K., Ma, J., & Hou, C. (2020). Spatiotemporally scalable matrix recovery for background modeling and moving object detection. Signal Processing, 168, 107362.

[8] Hu, W., Yang, Y., Zhang, W., & Xie, Y. (2016). Moving object detection using tensor-based low-rank and saliently fused-sparse decomposition. IEEE Transactions on Image Processing, 26(2), 724-737.

[9] Tang, C., Wang, P., Zhang, C., & Li, W. (2016). Salient object detection via weighted low rank matrix recovery. IEEE Signal Processing Letters, 24(4), 490-494.

[10] Shakeri, M., & Zhang, H. (2017). Moving object detection in time-lapse or motion trigger image sequences using low-rank and invariant sparse decomposition. In Proceedings of the IEEE International Conference on Computer Vision (pp. 5123-5131).

[11] Lin, Z., Chen, M., & Ma, Y. (2010). The augmented Lagrange multiplier method for exact recovery of corrupted low-rank matrices. arXiv preprint, arXiv:1009.5055.

[12] Lin, Z., Liu, R., & Su, Z. (2011). Linearized alternating direction method with adaptive penalty for low-rank representation. arXiv preprint, arXiv:1109.0367.

[13] Shu, X., Porikli, F., & Ahuja, N. (2014). Robust orthonormal subspace learning: Efficient recovery of corrupted low-rank matrices. In Proceedings of the IEEE conference on computer vision and pattern recognition (pp. 3874-3881).

[14] Sobral, A., Bouwmans, T., & Zahzah, E. H. (2016). Lrslibrary: Low-rank and sparse tools for background modeling and subtraction in videos. In: Bouwmans, T., Aybat, N., Zahzah, E.-H. (eds.) Robust Low-Rank and Sparse Matrix Decomposition: Applications in Image and Video Processing, CRC Press.

[15] Cuevas, C., Yáñez, E. M., & García, N. (2016). Labeled dataset for integral evaluation of moving object detection algorithms: LASIESTA. Computer Vision and Image Understanding, 152, 103-117.

AUTHOR INDEX

AMPILOVA, N. 33
ANDREEV, E. 54
DORONIN, G. 33
DRAGANOV, I. 58
FRANGOS, P. 1
GEORGIEVA, V. 43,48
KATSAROVA, V. 48
KOTOPOULIS, A. 1
LASKOV, L. 48
MIRONOV, R. 58
NEBOGATIKOV, I. 38
NIKOLOVA, M. 54
PANAGIEV, O. 20,27
POURAIMIS, G. 1
RADEVA, V. 54
SIMEONOV, I. 10
SIRKOVA, I. 6
SOLOVIEV, I. 38
TRIFONOV, T. 15
TSVETKOVA, D. 43